UNIVERSITY OF CALIFORNIA,
IRVINE

MOLECULAR IMAGING FOR BREAST CANCER USING MAGNETIC RESONANCE-GUIDED POSITRON EMISSION MAMMOGRAPHY AND EXCITATION-RESOLVED NEAR-INFRARED FLUORESCENCE IMAGING

DISSERTATION

submitted in partial satisfaction of the requirements
for the degree of

DOCTOR OF PHILOSOPHY

in Biomedical Engineering

by

Jaedu Cho

Dissertation Committee:
Professor Gultekin Gulsen, Chair
Professor Lydia Su
Professor Jered Haun

2017

DEDICATION

To

my wife, Gaeun, and my daughters, Alice and Anne,

who provide endless support and inspiration

A feeling bears on itself the scars of its birth; it recollects as a subjective
emotion its struggle for existence;
it retains the impress of what might have been, but is not.

Alfred North Whitehead
Process and Reality

and hope

If the fool would persist in his folly he would become wise.

William Blake
"Proverbs of Hell"

TABLE OF CONTENTS

LIST OF FIGURES

LIST OF TABLES

ACKNOWLEDGMENTS

I would like to express the deepest appreciation to my committee chair Professor Gultekin Gulsen, who has the attitude and the substance of a genius: he continually and convincingly conveyed a spirit of adventure in regards to research, scholarship, and excitement in regarding teaching. Without his guidance and persistent help, this dissertation would not have been possible.

I would like to thank my committee members, Professor Lydia Su and Professor Jered Haun for serving as a committee member and have generously given their time and expertise to better my work. I thank them for their contribution and their friendly support. I would like to thank the founder of our research center, Professor Orhan Nalcioglu. Thank you for giving us insightful perspective in biomedical imaging techniques, and for providing resources and training to support our research. I am especially indebted to Professor Chang-Seok Kim, who have been supported of my academic goals.

I am very thankful for the five years of being a member of John Tu & Thomas Yuen Center for Functional Onco-Imaging. I would like to thank all my lab members: Dr. Seunghoon Ha, Dr. Farouk Nouizi, Dr. Hakan Erkol, Dr. Tiffany Kwong, Dr. Alex Luk, Dr. Jessica Kwong, Jie Zheng, and Yang Zhang. These five years were truly a precious experience for me. I realize how lucky I am to find a good lab like this, how much I need to rely on other people, and how much help and support I have received from these amazing people.

Nobody has been more important to me in the pursuit of this project than the members of my family. I would like to thank my parents, whose love and guidance are with me in whatever I pursue. Most importantly, I wish to thank my loving and supportive wife, Gauen, and my wonderful daughters Alice and Anne, who provided constant inspiration.

ABSTRACT OF THE DISSERTATION

Molecular Imaging for Breast Cancer Using Magnetic Resonance-guided Positron Emission Mammography and Excitation-resolved Near-infrared Fluorescence Imaging

By

Jaedu Cho

Doctor of Philosophy in Biomedical Engineering

University of California, Irvine, 2017

Professor Gultekin Gulsen, Chair

The aim of this work is to develop novel breast-specific molecular imaging techniques for management of breast cancer. In this dissertation, we describe two novel molecular imaging approaches for breast cancer management.

In Part I, we introduce our multimodal molecular imaging approach for breast cancer therapy monitoring using magnetic resonance imaging and positron emission mammography (MR/PEM). We have focused on the therapy monitoring technique for aggressive cancer molecular subtypes, which is challenging due to time constraint. Breast cancer therapy planning relies on a fast and accurate monitoring of functional and anatomical change. We demonstrate a proof-of-concept of sequential dual-modal magnetic resonance and positron emission mammography (MR/PEM) for the cancer therapy monitoring. We have developed dedicated breast coils with breast compression mechanism equipped with MR-compatible PEM detector heads. We have designed a fiducial marker that allows straightforward image registration of data obtained from MRI and PEM. We propose an optimal multimodal imaging procedure for MR/PEM.

In Part II, we have focused on the development of a novel intraoperative near-infrared fluorescence imaging system (NIRF) for image-guided breast cancer surgery. Conventional spectrally-resolved NIRF systems are unable to resolve various NIR fluorescence dyes for the following reasons. First, the fluorescence spectra of viable NIR fluorescence dyes are heavily overlapping. Second, conventional emission-resolved NIRF suffers from a trade-off between the fluence rate and the spectral resolution. Third, the multiple scattering in tissue degrades not only the spatial information but also the spectral contents by the red-shift. We develop a wavelength-swept laser-based NIRF system that can resolve the excitation shift of various NIR fluorescence dyes without substantial loss of the fluence rate. A linear ratiometric model is employed to measure the relative shift of the excitation spectrum of a fluorescence dye.

Chapter 1: Introduction

1.1. Breast cancer imaging

Breast cancer has been one of the most frequently diagnosed cancers and the leading cause of deaths in women worldwide. (1) The American Cancer Society estimates about 321,120 new cases of breast cancer will be diagnosed and about 40,610 women will die from breast cancer in 2017 in the United States alone. (2) Fortunately, the mortality of breast cancer is gradually declining due to new development in advanced techniques in early diagnosis and therapy. (3-5) However, many technical challenges remain to be resolved. Breast cancer is a family of diseases including different presentation, biology, and response to therapy. (6) Conventional anatomy-based imaging techniques for breast cancer, such as mammography and ultrasound, cannot deliver an ideal diagnostic yield due to numerous individual effects including ages, breast density, and hormonal status. (7, 8) Also, optimal breast cancer treatment with personalized medicines often requires knowledge about the molecular behavior of various subtypes of tumors. (9, 10) Furthermore, incomplete resection of the tumor during surgical treatment causes a high rate of unwanted recurrent of the lesion. (11) Therefore, knowledge of tumor identification, growth, progression, and other important biomolecular pathways can be critical value in the management of breast cancer patients. Recently, molecular imaging has emerged to provide knowledge of tumor biology and applied to daily practice. (12) Molecular imaging is defined as the visualization, characterization, and measurement of biological process at the molecular and cellular levels in humans and other living systems including two- or three-dimensional imaging as well as quantification over time. (13) Molecular imaging can be used for various stages of cancer management such as screening, staging, therapy response monitoring, and image-guided surgery.

(14) Molecular imaging instrumentation comprised tools that enable visualization and quantification in space and over time of signals from molecular imaging agents. Molecular imaging instrumentation includes magnetic resonance imaging, positron emission tomography (PET), single photon emission computed tomography (SPECT), optical imaging, and others. Table. 1.1 shows the summary of various molecular imaging instrumentation.

Table 1.1 Summary of various molecular imaging instrumentation.

TECHNIQUES	ENERGY SOURCE	SPATIAL RESOLUTION	DEPTH	TEMPORAL RESOLUTION	SENSITIVITY (MOLE/L)
MRI	Radio wave	25-100 μm	No limit	min - hour	10^{-3} - 10^{-5}
PET(15)	High energy γ-rays	6-8 mm	No limit	sec-min	10^{-11} – 10^{-12}
SPECT(16)	Low energy γ-rays	10 mm	No limit	min	10^{-10} – 10^{-11}
Fluorescence	Visible/near-infrared	2-3 mm	<1 cm	sec	~10^{-9} – 10^{-12}

1.2. Magnetic resonance imaging for breast cancer

Magnetic resonance imaging (MRI) is a three-dimensional imaging technique that uses a strong magnetic field and radiofrequency (RF) pulses to image relevant anatomical structures and functional information. MRI produces excellent soft tissue contrast and functional information with a relatively high spatial resolution such that it is used for screening, therapy monitoring, preoperative staging, and guided biopsy for breast cancer. (17) Breast MRI is the most reliable imaging technique in preoperative staging of local extent of breast cancer (18), and the sensitivity is the best of all imaging techniques. (19) Breast MRI requires the administration of a gadolinium-based contrast agent during the study; early study shows that breast MRI does not have a diagnostic value without the contrast agent. (20) The contrast agent, for example, gadolinium-diethylenetriaminepentacetatic acid, GdDTPA, wash-in through the leakiness of microcapillaries

of a tumor and then wash-out via reverse diffusion from the extracellular compartment into the blood stream. (21) Multiple data sets are acquired before and after the administration of the contrast agent to track the dynamic curve of the contrast agent over time. Breast MRI begins with pre-contrast T2- or T1-weighted images. T2-weighted images of breast MRI show lesion with high contents of water otherwise there is no evidence of added value of T2-weighted imaging in breast MRI. (22, 23) The most widely used RF pulse sequence in breast MRI is the T1-weighted dynamic contrast-enhanced acquisition. Breast MRI is used for cancer detection in the dense breast, which is hardly seen in the conventional mammogram. However, the uptake of the gadolinium-based contrast agent is dependent on the phase of the menstrual cycle such that careful imaging planning is required for reliable diagnosis.

1.3. Nuclear imaging for breast cancer

PET is a three-dimensional nuclear medicine imaging techniques that are used to map out the underlying biochemistry. The PET system detects pairs of high energy γ-rays (511 keV), which are emitted in directions 180° apart, generated by a positron-emitting radionuclide such as ^{15}O, ^{13}N, ^{11}C, and ^{18}F. The high energy γ-ray emitting nuclides often conjugate with biologically active molecules for PET metabolic imaging. The most widely used PET metabolic imaging tracer is ^{18}F-fluodeoxyglucose (FDG), which is an analog of glucose. The uptake of the radioactive tracer indicates the cellular metabolic activity, and imaging of FDG allows to explore the possibility of invasive cancer. FDG uptake imaging, called FDG-PET, is the most common type of PET scan in breast cancer imaging. FDG-PET is widely used for oncological diagnosis, staging, and treatment monitoring for various types of cancer including breast cancer. However, FDG-PET scanner is optimized for the whole-body scanning such that the conventional PET scanner does not provide ideal diagnostic and monitoring yields for breast cancer imaging. Recently, positron emission

mammography (PEM) has rapidly drawn attention in molecular breast cancer diagnosis due to its high spatial resolution (< 2 mm), excellent imaging sensitivity and specificity. PEM is a dedicated breast imaging technique that utilizes two opposing γ-ray detector heads and breast compression paddles. PEM allows improved spatial resolution and photon detection sensitivity about whole-body PET scanner.

1.4. Fluorescence imaging for breast cancer

1.4.1. Optical molecular imaging for image-guidance breast cancer surgery

More than a half-million of cancer patients undergo surgical treatment in the United States alone. (24) Surgical removal of the lesion is the most effective cancer treatment and cure almost a half of all cancer patients. (25) Every year one-fifth to one- quarter of breast cancer patients suffer from high local recurrence rate due to incomplete removal of the targets, (26, 27) and the mortality of post-surgery relapse is high. (28) The key to successful surgical treatment is to remove primary tumors and metastatic pathways completely. Proper imaging tools with the ability to landmark tumors, nerves, and blood vessels are required for the successful surgical treatment.

Intraoperative imaging is emerging technique that delineates the surgery margins and helps surgeons to avoid unnecessary damage to vital anatomical structures. There are several conventional intraoperative imaging techniques, such as magnetic resonance imaging, computed tomography, positron emission tomography, and ultrasound. However, most of these conventional radiological modalities are costly and bulky except for the ultrasound, make it impractical for use around the surgical table such that it does not allow easy access to surgeons. Ultrasound provides high spatial resolution and tomographic images. However, the high spatial resolution comes at the cost of small field-of-view, and it requires physical contact of the ultrasound probe posing potential infection-related problems.

Intraoperative fluorescence imaging has revolutionized the field of surgery-guidance imaging by clearly delineating target lesion or structures that need to be identified using exogenous fluorescence agents. (29, 30) Intraoperative fluorescence imaging leverages higher spatial resolution and sensitivity than human vision and ergonomically placed around the surgical table facilitating the surgical workflow. (31) Intraoperative fluorescence imaging is characterized by illuminating targeted contrast agent with a shorter wavelength and taking images or videos of the emission intensity of fluorophores with a longer wavelength. The high-contrast originates from the difference of wavelengths between excitation and emission since the signal from the target is only visible with a properly designed fluorescence imaging system. Particularly, near-infrared intraoperative fluorescence imaging has greater benefits to UV-VIS spectral range. First, NIR light penetrates deeper than UV-VIS. Second, NIR reduces background tissue fluorescence. Last, the vision of surgeon will not be interfered by the intensive excitation lights; NIR is invisible to human eyes.

1.4.2. Fluorescence agents for intraoperative NIRF

There are several promising NIR fluorophores under development towards clinical approval. (29, 32-34) We summarized viable NIR fluorescence agents in Table 1. ICG is the only fluorophore approved for clinical usage in NIR spectrum. ICG is a lipophilic cyanine dye whose excitation spectrum depends on the nature of the solvent and the concentration, and the excitation peak of ICG shifts from 780 nm to 807 nm as soon as free ICG binds to lipoproteins such as albumin in plasma leading to chemical stabilization of ICG. (35, 36) Once ICG in the blood or lymphatic stream, ICG is strongly confined in the vessels, which is why ICG is mainly used for angiography, lymphangiography, perfusion, cardiac output, and hepatic function studies. The

lipophilicity of ICG results in the fast clearance rate. (37) Even though ICG is a non-specific NIR agent, it is used for tumor (34) and atherosclerotic plaque targeting studies. (38) For tumor imaging, ICG is a small molecule (775 Da) that tend to accumulate in tumor through the coarse structure of the neovasculature, which is called the enhanced permeability and retention (EPR) effect. For atherosclerosis imaging, macrophages in the plaque engulf ICG such that the plaque tends to have more fluorescence contrast than the background. IRDye800CW is designed to reduce the renal clearance rate such that the agent remains longer than ICG. Due to its hydrophilicity, IRDye800CW is chemically stable in serum. IRDye800CW is also charged negatively such that it bound to tissue non-specifically. However, IRDye800CW can conjugate with targeting ligands. (39, 40) Zwitterionic dyes are newly synthesized to target specific tissue. (41) It has charge neutral molecular structure resulting in the charge-shielding effect such that it prohibits the non-specific molecular binding, and the quantum yield outperforms other conventional NIR fluorophores. Most of the clinically viable NIR fluorescence dyes shares the practical limitation. The Stoke's shift of the fluorescence dyes are subtle, 15 nm, the maximum excitation, and full spectrum acquisition are challenging in epi-illumination geometry, such as open surgery and endoscopic imaging due to the excitation leakage. The leakage causes the false positive signal that severely degrades the sensitivity of the fluorescence imaging system. The key design issues are choosing the right excitation source and detection optics for better SNR.

Table 1.2 Summary of NIR fluorophores for intraoperative imaging.

DYES	EXCITATION PEAK	EMISSION PEAK	QUANTUM YIELD	PROPERTIES	APPLICATION
INDOCYANINE GREEN	807 nm	822 nm (serum)	9%	Lipophilic Non-specific	Angiography, lymphangiography, bile duct, GI track, tumor imaging
IRDYE800CW	774 nm	789 nm	12%	Hydrophilic Non-specific Ligand conjugatable	Tumour imaging and ICG
ZWITTERIONIC DYES	772 nm	788 nm	15%	Hydrophilic	Tumour imaging with targeting tissue

1.4.3. Intraoperative NIRF imaging systems

Various intraoperative NIRF systems have been developed, as summarized in Table 2. Most of the systems are designed to image NIR fluorophores such that excitation source and emission filters are designed from 750 nm to 806 nm excitation and 780 nm to 900 nm emission detection. Those intraoperative NIRF systems have been heavily used in the visualization of cardiovascular (42-44), biliary tract (45-47), tumor (48-50), diabetic ulcer (51, 52), gastrointestinal tract, and lymph nodes (53-55). NIRF imaging has been performed in either open surgery or minimally invasive surgery. The key design issue for high-performance NIRF system is to choose excitation light sources and detection optics. The best strategy for fluorescence imaging is to excite the fluorescence agent at the excitation peak and collect all the spectrum of the emission light. The challenge for this ideal strategy is the excitation leakage at modern optics. Modern thin film technologies perform the optical density (OD) of seven out of band rejection. However, the transition from the passband (OD 0) and the out-of-band (OD 7) is not steep enough to match up with the Stoke's shift of currently available fluorescence dyes, 15 nm, such that the maximum peaks of excitation and emissions are designed to have minimum 30-nm separations. Also, it is intended for normal incident rays such that backscattered oblique incident light leak through the filters and added as noise non-fluorescence signal.

Table 1.3 Review of articles for intraoperative NIR fluorescence imaging system

Instrument	Excitation	Emission	Applications	Manufacturer/Multispectral
Laser type				
ArteMIS (30, 56)	793 nm	NS	Open surgery	Quest Medical Imaging/comment
da Vinci® Si HD	803 nm	830 nm	Robotic	Intuitive Surgical/ single channel
platform w/			Endoscopy	NIR fluorescence
FireFly (30, 57, 58)				
FDPM imager (59)	785 nm	825-835 nm	Lymphangiography(60)	Univ. of Texas Health Science Center
Fluobeam 800 (59, 61, 62)	780 nm	800 nm	Open surgery	Fluoptics/single channel NIR fluorescence
IC-View(33, 59)	780 nm	835 nm	Perfusion (63)	Pulsion Medical System SE/NS
Iridium (62)	785 nm,	825-850 nm	Open surgery	Vision Sense/ single channel NIR
	805 nm		Endoscopy(64)	fluorescence
SPY Elite (30, 62, 65, 66)	806 nm	825-850 nm	Open surgery	Novadaq Technologies Inc./ single
PINPOINT (30, 67)			Laparoscopy	channel NIR fluorescence
LUNA			Diabetic foot ulcers	
SurgOptix T3(30, 68)	750 nm	NS	Open surgery	SurgOptix, Inc./
LED type				
FLARE™ (30, 69)	656-678 nm	689-725 nm	Open surgery	Beth Israel Deaconess Medical
mini-FLARE (70)	745-779 nm	800-848 nm		Center/Multispectral 2-ch simultaneous
Lab-FLARE® Model	665 ± 3 nm	685-735 nm	Open surgery	Curadel ResVet
R1 (62)	760 ± 3 nm	>781 nm		Imaging/Multispectral 2-ch simultaneous
Goggle System (29, 71)	770 nm	830 nm	Wearable imaging	Washington University at St. Louis/prototype

PDE (Handheld) (30, 72) PDE-2 / PDE-neo™ (62, 73)	760 nm	> 820 nm	Open surgery Laparoscopy	Hamamatsu Photonics K.K./Single channel
HyperEye (74)	760-780 nm	800-850 nm	Open surgery	Mizuho Medical Co.
Quest Spectrum (62)	NS, Laser available	700-830 nm 830-1000 nm	Open surgery Laparoscopy	Quest Medical Imaging/ Multispectral 2-ch (700/800 nm) simultaneous
Solaris™ Open-Air	667 nm, 743 nm, 757 nm	692-742 nm 770-809 nm >784 nm	Open surgery	PerkinElmer/Multispectral 4-ch sequential (VIS 1-ch, NIR 3-ch)
SurgVision Explorer Air (62, 75)	760 nm	NS	Open surgery	SurgVision BV
Xenon arc lamp type				
Leica M720 OH5 platform w/ Leica FL800(29, 59)	700-800 nm	820-860 nm	Intraoperative angiography	Leica Microsystems Inc.
PENTERO 900 platform w/ INFRARED™ 800™ and FLOW® 800 (29, 30, 33, 59)	700-780 nm	820-900 nm	Intraoperative angiography	Karl Zeiss Inc.

1.4.4. Spectroscopic NIRF instrumentation

Various sNIRF systems are developed to separate multiple fluorescence agents to solve complex biomedical problems. (76-80) Conventional wavelength selection methods rely on the binary splitting of fluorescence emission techniques such as sequential single-channel or simultaneous multi-channel spectral imaging. (62) However, conventional emission splitting methods are not suitable for multiple agent NIRF imaging applications. Since the fluence rate of emission is a critical factor for intraoperative imaging, most of conventional sNIRF systems are equipped with wideband emission filters. Therefore, the use of fluorescence agents is limited to a few widely separate fluorescence agents including visible or far-red fluorescence agents, such as fluorescein, methylene blue, and porphyrins.

The full potential of intraoperative spectroscopic NIRF imaging could be achieved by utilizing the newly viable NIR fluorophores summarized in Table 1. The successful spectral decomposition starts from the high-spectral resolution data acquisition without severe compromise of the emission fluence rate. The conventional spectral resolving method of splitting emission signal at detection side has been unable to resolve the viable NIR fluorophores. We introduce a new concept in resolving currently viable NIR fluorescence agents using excitation spectroscopy.

1.4.5. Excitation spectroscopy

Measurement of fluorescence excitation spectrum is challenging in intraoperative imaging setup. Excitation light source homogenously illuminates a surface of tissue containing target fluorescence agents, and quantitative measurement of the excitation energy absorption by the fluorescence agents is difficult. The fluorescence in low concentration can be approximated by Equation. (1.1),

$$F(\lambda) \approx I\eta \frac{\Omega}{4\pi} 2.303\varepsilon(\lambda)lc. \qquad (1.1)$$

where, F is the steady-state fluorescence intensity, I is the normalized excitation intensity on the target, Ω is the solid angle, ε is the molar extinction coefficient as a function of the excitation wavelength λ, η is the quantum efficiency, l is the path length of excitation light through the fluorescence sample. Since the quantum yield of the fluorescence is independent of the excitation wavelength, the fluorescence intensity is proportional to the quantum yield, the concentration of fluorophore, and absorbed energy during the excitation. Accordingly, the measurement of the fluorescence intensity difference while examining the laser wavelength can provide spectral information of the wavelength-dependent excitation of the fluorophores. In a mixture of two different fluorescence agents, identification of two distinct fluorescence agents is possible by solving linear algebra when at least two different wavelengths are used. In the case of using double agents such as ICG and IRDye800CW or Zwitterionic dyes, the same absorption wavelength (hence force isosbestic point) occurs between their maximum excitation peaks (775 nm – 805 nm). It is a narrow spectral band, and a proper spectrally-resolved source is essential for the excitation spectroscopy.

There are three major types of the spectrally-resolved source that are used for intraoperative fluorescence imaging, namely laser, light emitting diodes, and filtered broadband source. Laser excitation systems tend to have a small separation between the excitation and emission wavelengths (< 30 nm) that takes advantage of exciting the fluorophores at almost maximum excitation. Indeed, laser systems allow the most sensitive fluorescence imaging due to the high fluence rate that is most significant for NIR fluorescence agents at low concentration in tissue. The laser has an advantage in light coupling due to its narrow solid angle that is effective to minimally invasive surgery with endoscopy. However, extra caution is required to protect healthcare

providers from the high-intensity laser beams. Light emitting diodes (LEDs) are a reasonable compromise for cost-effectivity and performance. Combined array of LEDs emits high enough excitation lights. However, the excitation-emission separation is greater than 50 nm due to its relatively broad spectrum and it requires additional excitation spectral filtering to reduce the leakage signal. Xenon arc lamp is a broadband light source that is frequently used for the excitation. It requires post-filtering of the light due to its broadband nature such that thermal relief on the illumination and filter system is required.

1.4.6. Wavelength-swept laser

Wavelength-swept laser is widely used for cutting-edge technological applications. (81) The use of the wavelength-swept laser in sNIRF imaging can provide a variety of biomedical applications in a laboratory as well as a clinical research setup. In this work, we propose a novel method that can obtain excitation-resolved images in NIRF by employing a near-infrared wavelength-swept laser as opposed to the previously techniques employed on the detection side of the instrumentation. To the best of our knowledge, we demonstrate for the first time the excitation-resolved NIRF imaging with a wavelength-swept laser and a CCD camera. Several research groups have reported on several types of near-infrared wavelength-swept lasers for biomedical imaging. (82-84) Meanwhile, we recently developed a wavelength-swept laser centered at 800 nm to image microstructural and functional information of blood in-vitro (85) and high-resolution depth-resolved retina layers (86) for swept-source optical coherence tomography. The wavelength-swept laser that we have developed can tune the wavelength from 780 nm to 820 nm, which covers the maximum excitation wavelength of ICG. Since a piezoelectric transducer based wavelength

selector poses thermal instability, we have employed a holographic transmission grating and a Galvo-scanner as a wavelength selector to avoid the heat instability.

1.5. Dissertation organization

This dissertation consists of two parts. The first part, Part I**,** is about our new concept of therapy monitoring for breast cancer technique using a multimodal MR/PEM system. *Chapter 3* introduces MR/PEM and demonstrate the proof-of-concept including the development of MR-compatible PEM detector heads, dual-modality imaging interface, breast compression paddles, and single-channel breast coil for dedicated MR/PEM breast imaging. *Chapter 4* describes the development of dual-channel breast coil for improved signal-to-noise ratio and scanning speed in our novel MR/PEM therapy monitoring application. Our prototype single-channel coil in *Chapter 3* is significantly enhanced by adding a saddle coil. The SNR of MR image is 20 % better than a commercial clinical 4-channel breast coil, and its MR scanning speed is comparable to the commercial one.

The second part of this dissertation, Part II**,** focuses on the development of excitation-resolved intraoperative fluorescence imaging system using a near-infrared swept laser for surgery-guidance imaging. *Chapter 5* gives the details of our novel excitation-resolved intraoperative fluorescence imaging system using a near-infrared wavelength-swept laser. We describe a straightforward spectral decomposition with a spectrum centroid method. *Chapter 6* provide introduces our novel method for quantitative excitation spectrum measurement using a linear ratiometric model.

In *Chapter 7*, Conclusion and future directions that could extend and improve the work in this dissertation are described.

1.6. Innovation and contributions

Several innovative contributions have been achieved in this dissertation:

1. We demonstrate the proof-of-concept of breast cancer therapy monitoring using dual-modal MR/PEM system. We also expect to achieve high-sensitivity and high-specificity breast cancer detection and diagnosis with further development.
2. Our dual-channel dedicated breast coil achieves comparable image SNR and imaging speed to a commercial clinical breast coil. Plus, our dual-channel coil enables multimodal imaging with customized imaging interface with breast compression paddles and PEM detector head mounting systems.
3. Our excitation-resolved intraoperative fluorescence imaging technique enables multiple near-infrared fluorescence agent imaging that conventional emission-resolved fluorescence imaging techniques cannot achieve. The development of new intraoperative fluorescence imaging system helps to solve complex biomedical problems.
4. Our excitation-resolved intraoperative fluorescence imaging technique expands the information content of conventional fluorescence imaging by providing additional spectral information. Phantom experiments are performed with plasma protein (bovine serum albumin) bound ICG and ICG dissolved in Dimethyl sulfoxide (DMSO). The results show that the HER-NIRF technique can visualize the distribution of DMSO in wide-field imaging setting. We believe that such a system will help the development of the penetration-enhanced drug-delivery techniques as well as new molecular imaging agents.

Chapter 2: Theoretical basis of positron emission mammography and fluorescence spectroscopy

2.1. Theoretical basis of positron emission mammography

2.1.1. Positron emission and decay

The unstable radio nucleus, the *parent*, spontaneously emits particles, photons or both releases energy, and became more stable product nucleus, the *daughter* in the process of nuclear transition from an unstable nucleus to a more stable one. It is called radioactive decay. The radioactive decay results in the conversion of mass into energy. Mass m and energy E are related to each other by Einstein's equation $E = mc^2$, in which c is the speed of light. The energy comes from the conversion of nucleus mass or electron mass. According to the equation, the mass of an electron is equivalent to 511 keV of energy. The radioactive decay is associated with the nucleus such that a radioactive nucleus does not affect the chemical behavior of its molecules. Independence of radioactive nucleus and chemical properties of molecules is of keen interest in molecular tracer studies with radioactive labeling. There are several modes of radioactive decay, such as b- emission, b-, g emission, isomeric transition, internal conversion, electron capture, and positron emission.

During radioactive decay by positron emission, a proton (p+) in the radioactive nucleus is transformed to a neutron (n) and a positron (e+). The positron and a neutrino are ejected from the nucleus. The positron emission process is described by

$$p^+ \rightarrow n + e^+ + \nu + E \qquad (2.1)$$

Since a positron is the antimatter of an electron, it annihilates with an electron and radiates the mass-equivalent energy of 511 keV. This process involves two particles with the same mass, and

a pair of photons are emitted with nearly 180 degrees apart each other to conserve the momentum for a stationary positron-electron. Since both positron and electron have motion, the emitted angle might be slightly off 180 degrees by a tenth of a degree.

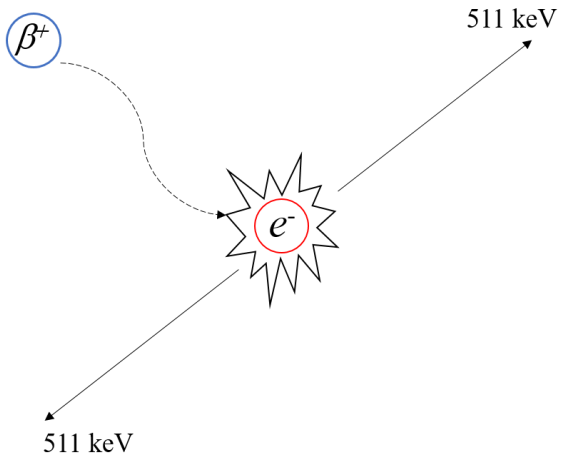

Figure 2.1 Schematic of an annihilation reaction between a positron and an electron. A pair of 511 keV photons is emitted with 180 degrees apart from each other.

The average decay rate of a sample containing the number of N radioactive atoms of a radionuclide is given by

$$\Delta N/\Delta t = -\kappa N \qquad (2.2)$$

where ΔN is the net change in the number of radioactive atoms of a radionuclide, Δt is the time change, κ is the decay constant for the radionuclide in units of sec^{-1}. The average decay rate $(\Delta N/\Delta t)$ has the Systeme International (SI) unit of activity of the *becquerel* (Bq). If a sample has an activity of 1 Bq, it is decaying at an average decay rate of 1 sec^{-1}. Commonly used multiples of the becquerel are the kilo becquerel (1 kBq = 10^3 Bq), the mega becquerels (1 MBq = 10^6 Bq), and the Giga becquerel (1 GBq = 10^9 Bq). The traditional unit for activity is *curie* (Ci), which is defined by 37 GBq.

The number N of radioactive atoms decays exponentially. An exact mathematical expression of N at time t can be derived from Equation 2.2 using methods of calculus. Thus,

$$N(t) = N(0)\exp(-\kappa t) \qquad (2.3)$$

The half-life of a radionuclide is the time needed for it to be 50 % of the first activity. The half-life $(t_{1/2})$ is given by

$$t_{1/2} = \ln 2 / \kappa \qquad (2.4)$$

The half-life of ^{18}F is 109.7 minutes.

2.1.2. Interaction of gamma-rays with matter

The interaction between high-energy photons and matter can be modeled as simple particle collisions. A high-energy photon can knock out electrons from the electron orbital. There are twelve theoretically possible interactions between photons and matter. (87) The main interactions in nuclear imaging are the photoelectric effect, Compton scattering, pair production, and Rayleigh scattering.

The photoelectric effect is an atomic absorption process that an atom absorbs the energy of incident photons and ejects photoelectrons. The maximum kinetic energy $(E_{k,\max})$ of a photoelectron is given by

$$E_{k,\max} = h(f - f_0) \qquad (2.5)$$

where *h* is the Plank constant, *f* is the frequency of the incident photon, f_0 is the threshold frequency required to elicit the photoelectric effect on a matter. The photoelectric effect creates a vacancy in an electron orbital shell and leads to the emission of characteristic x-rays or Auger electrons. The probability of the photoelectric effect can be characterized by the cross section σ, which is given

by

$$\sigma \propto Z^n / (hf)^3 \qquad (2.6)$$

where Z is the atomic number, n is a number that depends on matter and varies between 4 and 5. In low-Z atoms, the binding energy of an electron in tissue is relatively small (~ keV) such that the photoelectric effect in tissue is a small factor at the photon energy of 511 keV.

The Compton scattering is an inelastic collision between an incident photon and an outer-shell electron orbital of an atom. If the energy of incident photons exceeds the binding energy of the outer-shell electrons, the interaction seems like a collision between the photons and free electrons. Unlike the photoelectric effect, the photon does not disappear in Compton scattering. The Compton scattered photon deflects through a scattering angle. A portion of energy transfer occurs in the process. The energy of the scattered photon (E_s) can be described by

$$E_s = E_0 - E_{re} \qquad (2.7)$$

where E_0 is the energy of the incident photon and E_{re} is the energy of the recoiled electron. The Compton scattering does not depend on the property of the matter. It is a photon-electron interaction. Typically, the energy change of the Compton scattered photon is not substantial at low energy (< 100 keV) and the Compton scattered photons are detected in either the forward or backward direction with a minimum angle of 90 degrees. At higher energies over 0.5 MeV, the scattering angle decreases as the energy of the incident photon increases.

The pair production is the creation of an elementary particle and its antiparticles such as creating a positron and an electron. For pair production to occur, the energy of the incident photons must be above a threshold to create a positron-electron pair. The positron and electron have arrest mass equivalent to 511 keV; the threshold incident photon energy must be above 1.022 MeV. The Rayleigh scattering is a type of elastic scattering interaction that occurs between a photon and an

atom. There is no energy change between the incident photon and the atom, and the photon is simply deflected from its original path. It is only important at low energy, and of little practical use in nuclear imaging.

2.1.3. Spatial resolution

The annihilation process emits two photons at a time in 180-degree opposing directions within a few millimeter of the origin as described in Figure 2.2. Most positrons or electrons travel in a matter in random directions and go through multiple deflections. The actual positron range is always smaller than the real positron path. The distance of interest in the effective positron range that is the average distance from the radionuclide to the end of the positron range and measured perpendicular to the actual line-of-response. The estimated value of the effective positron range of ^{18}F in water is around 1-2 mm. (88, 89) This positron range effect degrades the spatial resolution causes image blurring in nuclear medicine imaging as shown in Figure 2.2 and Figure 2.3(a).

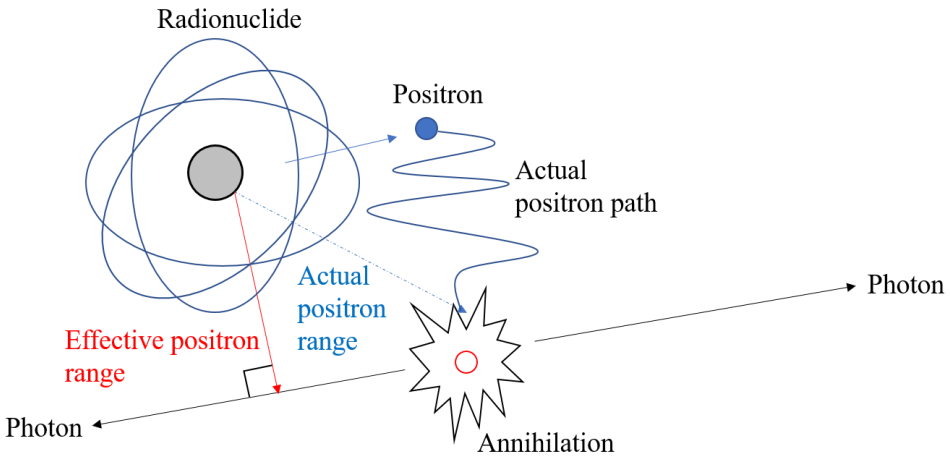

Figure 2.2 Schematic of the positron random walk emitted from a radionuclide. The random walk causes image blurring in nuclear medicine imaging. The perpendicular distance from the line-of-response and the radionuclide are referred to as the effective positron range.

Two opposing photons from the annihilation process does not always have an exact 180-degree angle as shown in Figure 2.3(b). The deviation from colinearity of the emitted photons occurs from the thermal motion of the particles and the conservation of the Fermi momentum. (90) The distribution of the angular deviation in water or biological tissue is around 0.5 degree. The non-colinearity effect is responsible for the spatial resolution degradation in a large diameter detector ring in a whole-body PET scanner. The full-width-half-maximum (FWHM) of the spatial resolution of a whole-body PET, with a detector diameter of *D*, can be described as:

$$FWHM \approx \Delta\theta \times D/4 = 0.0022 \times D \qquad (2.8)$$

where Δθ is the deviation angle of 0.5 degrees and D is measured in meters. Typically, this means the spatial resolution of 2.2 mm per unit meter of the detector distance.

The random coincident events from scattering contribute to the spatial resolution degradation. The high energy photons at 511 keV have a mean free path of about 10 cm in water. In the case of 20 cm diameter head or chest, 75% of annihilation photons undergo the Compton scattering and photoelectric absorption. The photoelectric absorption reduces overall detection sensitivity, while the Compton scattering causes inaccurate counting of line-of-response as shown in Figure 2.3(c).

The parallax error or depth of interaction error also contribute to the degradation of spatial resolution. The depth of interaction error occurs if the exact place of the annihilation is unknown in the crystal. The line-of-response does not necessarily match with the actual line-of-response. This spatial resolution degrading effect has more impact on the dedicated detectors such as PEM than a whole-body PET scanner because the good spatial resolution is crucial for these applications.

The high spatial resolution is crucial for molecular imaging to estimate the apparent molecular activity in small targets or region-of-interests. The intensity of each pixel in molecular

imaging should be proportional to the amount of molecular activity within the equal volume of tissue. One can define the partial volume effect as the loss of ability to correctly recover the actual amount of activity due to the limited resolution of the imaging system. If the target or region-of-interest to be acquired is less than twice the FWHM resolution of the imaging system, the imaging system underestimates the outcome activity in the target or region-of-interest. (91) The loss of apparent activity occurs when the background activity is zero. (92) The loss of activity involves an increase in activity in surrounding pixels, which reduces the tumor-to-background ratio. The ratio of apparent activity to true activity is called the recovery coefficient. The recovery coefficient can be applied to correct for the underestimated activities by the partial volume effect by using a priori anatomical information from high spatial resolution imaging systems.(93-96)

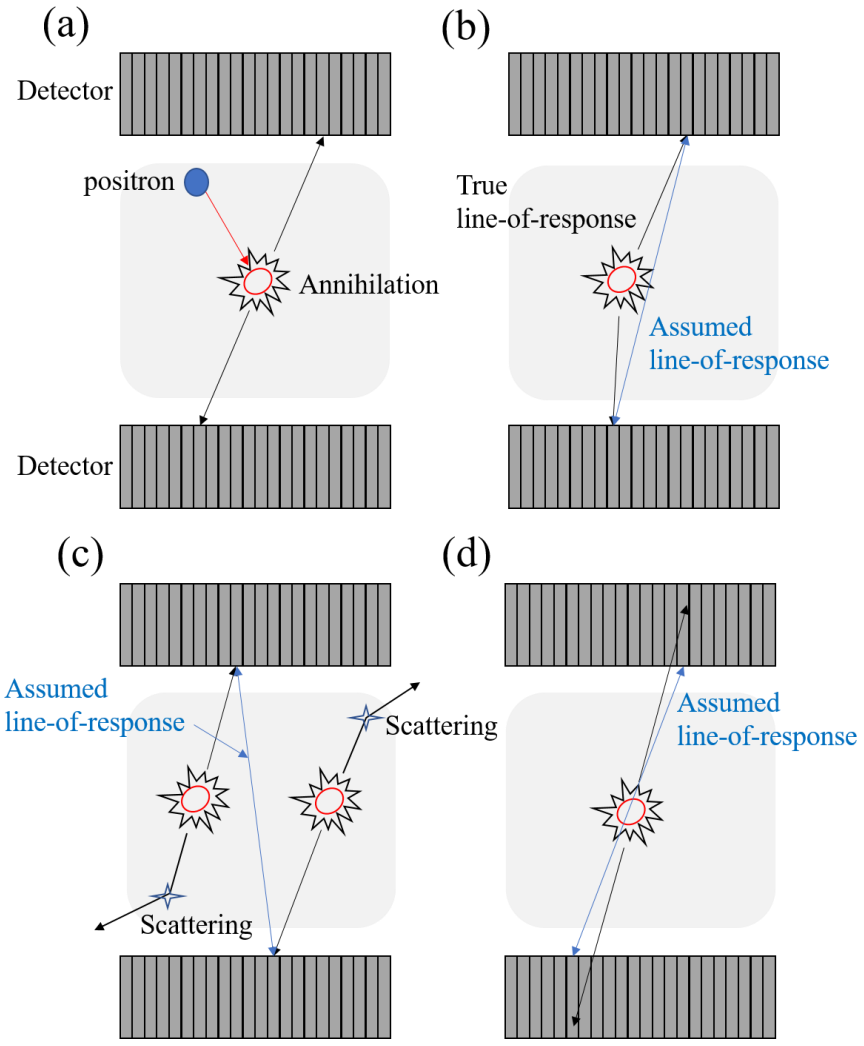

Figure 2.3 Schematic drawings of fundamental limitations in the spatial resolution in annihilation coincidence detection. (a) The annihilation point does not match with the actual radionuclide emitting positrons due to the positron range effect. (b) Acolinearity effect: the measured line-of-response is not the same with the real line-of-response due to the motion of particles. (c) Two different annihilations can cause random detection of the line-of-response. (d) The depth of interaction: it occurs when the crystal depth at which the photon interaction takes place is unknown.

2.1.4. Backprojection

Backprojection is widely used image reconstruction algorithm in X-ray computed tomography and nuclear medicine imaging. Backprojection employs on the direct inversion of the Radon transform such that it is fast, linear, predictable, and the properties are very well known. In general practice, a set of multiple projection images is acquired at different angles. The image is reconstructed on a 2D matrix of pixels in the Cartesian coordinate system. The annihilation event counts are assigned uniformly throughout all pixels that fall within the path of projection. When the backprojections for multiple angle profiles are added to a dataset, one can obtain an approximated image of annihilation activity in the scanned area. The backprojection of N profiles can be described by:

$$I'(x,y) = \frac{1}{N}\sum_{j=1}^{N} p(x\cos\phi_j + y\sin\phi_j, \phi_j) \qquad (2.9)$$

where, $I'(x,y)$ is an assumed image to the actual annihilation event distribution of $I(x,y)$, ϕ_i denotes the i^{th} projection angle. In PEM imaging, most of the breast is compressed, and the effective thickness is less than a few centimeter, while the mean free path of the annihilation photon is over 10 cm. In other words, most of the photons are detected with minimal attenuation by tissue. Multiple angle sampling of 2D projection data comprises a data set for 3D tomographic reconstruction. However, most PEM systems utilize a limited number of views such that the spatial resolution of the off-plane is not high (~ 8 mm) enough to be used for the clinical purpose. The anisotropic nature of PEM images can be improved by using other high-spatial resolution imaging modalities such as X-ray computed tomography or magnetic resonance imaging.

2.2. Theoretical basis of fluorescence spectroscopy

Fluorescence spectroscopy is a powerful tool for solving a broad range of problems in the biomedical, chemical, biological sciences. The fluorescence spectrum measurement provides valuable information on molecular processes such as the interaction of solvent molecules with fluorescent molecules, the distance between biomolecules, conformational molecular changes, and molecule-molecule binding interactions. The use of fluorescence is increasingly expanded by advances in molecular imaging techniques. Following is the fundamentals of fluorescence process that is required to understand Chapter 5 and Chapter 6.

2.2.1. Excitation and emission process of fluorescence

In most cases, fluorescence is the reemission of photons having lower energy (longer wavelength) than absorbed photons. Fluorescence molecules have two characteristic spectra: the excitation spectrum and the emission spectrum. The Jablonski diagram usually describes the processes between the excitation and emission of light as shown in Figure 2.4. Following light absorption, several fluorescence processes occur. A fluorescence molecule is excited to higher vibrational levels at S_1 or S_2. The excited electrons quickly relax to the lowest vibrational level of the excited state at S_1, which is called the internal conversion and occurs within 10^{-12} sec or less. Collisions cause this process with solvent molecules and with phonon modes in the fluorescent molecule. Vibrational relaxation is faster and photon emission. The fluorescence lifetime is typically 10^{-8} sec such that the internal conversion is complete before emission. Since the vibrational energy bands of the excited and ground states are similar, the emission and excitation spectrum of a fluorescence molecule is typically a mirror image of each other. Also, the spectrum of the emission is independent of excitation wavelength.

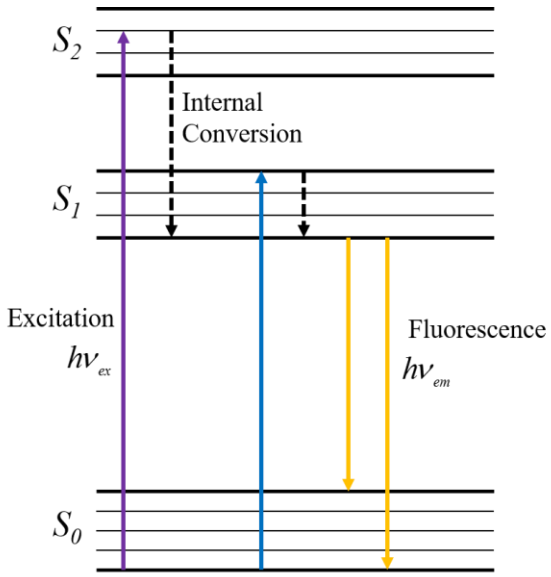

Figure 2.4 A Jablonski diagram.

Energy losses between excitation and emission are called Stokes shift, and they are observed for fluorescent molecules in solution. Also, fluorescent molecules display further Stokes shifts due to solvent effects, excited-state reactions, complex formation, and energy transfer.

The quantum efficiency η describes the ratio of the total energy emitted by a molecule per quantum of energy absorbed:

$$\eta = \frac{h\nu_{em}}{h\nu_{ex}} = \frac{k_r}{k_r + k_{nr}} \qquad (2.10)$$

where h is the Plank constant, ν_{em} and ν_{ex} are the frequency of the emission and excitation light, respectively. k_r and k_{nr} are the radiative decay rate and non-radiative decay rate, respectively. The higher the value of η, the greater the measured fluorescence of a fluorescent molecule. For example, a non-fluorescent molecule has zero quantum efficiency.

The average time of the molecule stays in the excited state before returning to the ground state defines the lifetime of the excited state. General fluorescence lifetimes are around 10 nsec.

The fluorescence lifetime τ can be described as:

$$\tau = \frac{1}{k_r + k_{nr}} \qquad (2.11)$$

The equation relating the fluorescence intensity *F* and the lifetime τ is:

$$F(t) = F_0 \exp\left(-\frac{t}{\tau}\right) \qquad (2.12)$$

Where F_0 is the initial intensity of fluorescence.t is the time after removal of the excitation source.

2.2.2. Photon interactions with biological tissue

Light propagation through tissue is characterized by the absorption and scattering of light by tissue. The optical properties of tissue alter the final measurement of fluorescence spectra. To correctly recover molecular information, we need to understand how light interacts with the biological tissue. During the propagation through the tissue, light can be either absorbed or scattered by particles in the tissue. (97) The absorption coefficient μ_a represents the probability of a traveling photon in tissue to be absorbed. The inverse of μ_a refers to the mean free path of a photon in a purely absorbing media.

The Beer-Lambert law describes the light absorption by media:

$$A = -\log_{10}\left(\frac{P}{P_0}\right) = -\log_{10} T = \varepsilon c b \qquad (2.13)$$

where *A* is the absorbance, P_0 is the incident radiant power, *T* is the transmittance, *P* is the outcoming radiant power, ε is the extinction coefficient, *c* is the concentration, and *b* is the light path length. When two or more types of solution are mixed, the total absorbance of the solution is the sum of its components:

$$A = \sum_{i=1}^{N} A_i = b \sum_{i=1}^{N} \varepsilon_i c_i \qquad (2.14)$$

where A_i, ε_i, and c_i is the absorbance, extinction coefficient, and concentration contribution from the ith solution. For example, when two types of the solution with unknown concentration are mixed, the wavelength dependent absorbance at two different wavelengths λ_a and λ_b can be described as:

$$\begin{cases} A(\lambda_a) = \varepsilon_1(\lambda_a) c_1 b + \varepsilon_2(\lambda_a) c_2 b \\ A(\lambda_b) = \varepsilon_1(\lambda_b) c_1 b + \varepsilon_2(\lambda_b) c_2 b \end{cases} \qquad (2.15)$$

Thus, the concentration of two molecules in the mixed solution can be recovered by solving the simple linear equation.

The absorption coefficient μ_a can be rewritten as:

$$T = \exp(-\mu_a b) \qquad (2.16)$$

alternatively, the absorption coefficient is proportional to the concentration and the extinction coefficient:

$$\mu = \varepsilon c \ln 10 = 2.303 \varepsilon c \qquad (2.17)$$

To estimate the absorbance of a particular solution, then one can use Equation (2.15) to identify N number of molecules with N number of wavelengths to solve the linear equation.

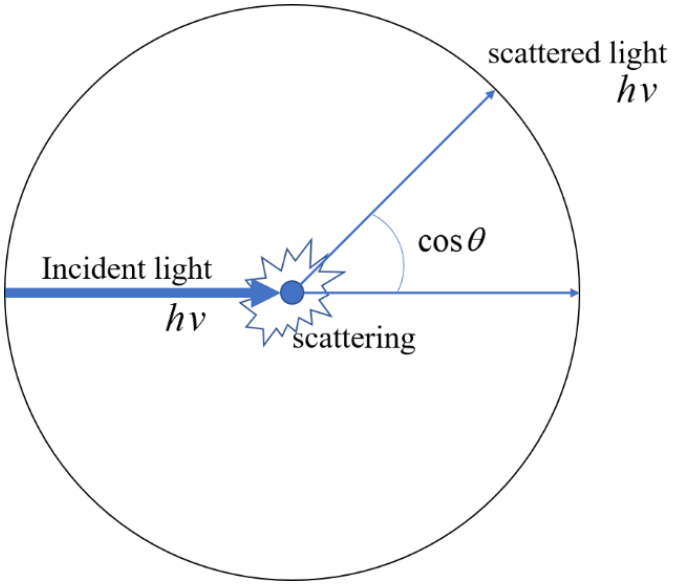

Figure 2.5 Schematic drawing of an elastic scattering event that deflects the original path of the incident light

While absorbing particles in tissue absorb light, scattering particles dispersed photons into a different direction from the original light path. Scattering is usually introduced by scatterers that have different refractive indices from the background tissue. The particle deflects a photon incident of a scatterer and the direction of photon propagation. Scattered photons retain its initial energy, keeping the same wavelength before and after the scattering event, which is called elastic scattering. Typical scatteres in tissue include cells, nuclei, mitochondria, collagen fibers, and membranes. In fluorescence imaging, elastic scattering dominates over inelastic scattering in most tissues, and therefore we focus on elastic scattering.

Photons traveling through in tissue are diffused and lose their original direction in a very short distance depending on the density of scatterers. Thus, the Beer-Lambert law cannot accurately describe the optical properties of tissue unless the actual path lengths of photons are precisely determined. If absorption is negligible, the scattering coefficient μ_s describes the

probability of a photon being scattered. As a highly scattering medium, tissue scatters incident photon in the forward direction. The parameter related to the forward scattering is known as the anisotropic factor *g*, which is the expectation value of the cosine of the scattering angle θ when a photon goes through the scattering events as shown in Figure 2.5. The definition of the anisotropic factor g is described by:

$$g = \langle \cos\theta \rangle \qquad (2.18)$$

The anisotropy factor is a measure of forward scattering retained after a single scattering event. If *g* is 1, the scattering is absolute forward scattering, while g equals to -1 means complete backward scattering. The isotropic scattering makes the anisotropic factor *g* zero.

The reduced scattering coefficient can be used to describe the diffusion of photons in turbid media with a step size of $1/\mu_s'$ where each step involves isotropic scattering events. The reduced scattering occurs if there are many scattering events before an absorption event. This situation of scattering-dominated light transportation is called the diffusion regime. The reduced scattering coefficient is employed to deal with visible and NIR light propagation in tissue, and it is described by:

$$\mu_s' = \mu_s(1-g) \qquad (2.19)$$

Biological tissue has the anisotropic factors between 0.8 and 1. The inverse of the reduced scattering coefficient, called the transport mean free path, describes the distance a photon will travel before becoming isotropic, and the incident photon completely loses its original direction.

2.2.3. Fluorescence intensity and concentration

The number of excited fluorescent molecules is proportional to the absorption is light intensity during the passage of the excitation light through the fluorescent sample with a path length of sample *b*. By applying the Beer-Lambert law, we obtain:

$$F = \eta I_0 \left[1 - \exp\left(-2.303 \varepsilon c b\right)\right] \qquad (2.20)$$

where I_0 is the incident light intensity.

If the fluorescent solution has a low concentration of a fluorescent molecule, Equation (2.20) becomes (2.21) by expanding the exponential term in the McLaurin series:

$$F = \eta I_0 \left(2.303 \varepsilon c b\right) \qquad (2.21)$$

Thus, a plot of fluorescence versus concentration can be linear at low concentrations. The linearity of fluorescence as a function of concentration holds over a wide range with linearity extending over four to six decades. (98)

Chapter 3: Development of magnetic resonance/positron emission mammography system

3.1. Introduction

Breast cancer is one of the commonly diagnosed cancer among American women and has the second highest death rates besides lung cancer. (1) However, because cancer affects everyone differently, and different treatment strategies are needed for different people. (10, 99, 100) There are four major molecular subtypes of breast cancer, namely luminal A, luminal B, triple negative/basal-like, and HER2 type. Triple negative/basal-like tumors represent 20 percent of all breast cancers. It tends to occur more often in younger women, which has a practical difficulty in early diagnosis, and is associated with faster tumor growth rate, and a poorer prognosis. (101-103)

For the aggressive subtypes of breast cancer, a physician must plan several treatment options for a short period before the quickly growing tumor advances further. Therefore, successful breast cancer therapy for young women relies on fast and accurate monitoring of individual responses to the treatments. Dynamic contrast enhanced-magnetic resonance imaging (DCE-MRI) is the leading and most commonly used functional imaging technology to image breast cancer and monitor treatment response. (104-106) Breast DCE-MRI (henceforth breast MRI) requires the use of dedicated breast coils to monitor the temporal variation characteristics of an MRI contrast agent through the neovasculature of the breast by rapid acquisition of multiple MRI images. However, standalone breast MRI has the traditionally high false-positive rate. (107) Furthermore, the immediate response to cancer therapy cannot be measured by the change of permeability surface area. Consequently, molecular response monitoring is crucial for planning the cancer therapies to the patients who suffer from aggressive subtypes of breast cancers.

Recently, combining positron emission tomography (PET) with MRI has been emerged to solve this problem by providing immediate physiological responses to cancer therapies. (108-111) PET provides functional information that can be used to differentiate recurrent cancer from scar tissue and has proven its ability to depict the extent of disease for surgical planning. (112, 113) However, the relatively low spatial resolution (~ 5 mm) due to the large diameter of the PET detector ring results in an inaccurate estimation of the functional information. (114)

Positron emission mammography (PEM) is an emerging nuclear medicine imaging technique that is characterized by two opposing annihilation photon detectors and breast compression paddles. (115-118) Like X-ray mammography, the gently compressed breast reduces the effective thickness of the breast tissue and takes one or multiple 2D images. Unlike the mammography projection images, the images from PEM is anisotropic tomosynthesis emission images that result in the high-resolution in-plane images. The short distance between the two opposing detectors allows high-resolution nuclear medicine imaging up to < 2 mm at the in-plane. This high-spatial resolution can lead to the correct tumor-to-background ratio of ^{18}F-FDG that was traditionally hard to achieve with the whole-body PET scanner. (119) Indeed, for every 2 mm improvement in the spatial resolution, the total number of counts can be reduced by a factor of three to four for equal subjective image quality. (120) The ability to provide high spatial resolution in functional imaging overcomes the partial volume effects. The increased tumor-to-background ratio in the functional imaging results in a more accurate diagnosis, reduces dosage, and allows monitoring of the physiological response of a tumor to the therapy. However, the excellent spatial resolution of PEM comes at the cost of the limited field-of-view (FOV). Consequently, more images must be taken which increasing the scanning time.

Combining PEM and MRI in a single system can yield highly sensitive and specific breast

cancer therapy monitoring as well as breast cancer examinations while at the same time compensating for the shortcomings that exist when using only standalone PEM and MRI. Breast MRI provides the full-scale anatomical information of the tumor with supplementary functional information, while PEM provides the functional information with the high spatial resolution in the cancer therapy monitoring.

The combination of PEM and MRI system is challenging due to the physical constraints. Clinical MRI systems have an inner bore diameter of 60 cm, and the breast coil only allows an area of 10 cm by 15 cm area for the PEM imaging systems. The integration of both PEM and MRI modalities for breast imaging requires the significant reduction in the size of the PEM imaging system and necessitates a new design and development of the MRI breast coil housing. In addition, a well-designed multimodal fiducial marker that facilitates the imaging data registration is crucial.

In this chapter, to the best of our knowledge, we develop the first integrated MR/PEM system and demonstrate its capabilities to for dual cancer therapy monitoring with a proof-of-concept study. This revolutionary one-of-a-kind MR/PEM system can provide valuable insight on how and whether a tumor is responding to treatment much faster than traditional MRI without significantly compromising specificity and sensitivity.

3.2. Methods

3.2.1. Pixelated silicon photomultiplier-based MR-compatible PEM system

Two opposing MR-compatible PEM detector heads are used to capture the radioactivity images as shown in Figure 2.1(a). The PEM detector head is based on a 20 x 20 pixelated Cerium-doped lutetium (LYSO) scintillator crystal. The total area of the crystal face and each pixel size are 42 x 42 mm^2 and 2 x 2 mm^2, respectively. Processing of the LYSO crystal (cutting, polishing, and assembling) was done by Agile Technologies Inc. Thin reflection coatings (Enhanced Specular Reflector, 3M) between pixels are glued on the septa to prevent the photon leakage to adjacent compartments. This gluing process on the septa requires an extra space of 0.1 mm between pixels resulting in the pitch of array 2.1 x 2.1 mm^2. The LYSO crystal has the density of 7.1 g/cm^3 and the emission peak wavelength of 420 nm. The decay time of LYSO is 41 ns, and the light yield is 32 photons/keV. The photoelectric yield for Gamma-ray is 75%, and the energy resolution is 7.1 %. The attenuation length of LYSO is 12 mm at 511 keV which allows a compact design with the crystal depth of 13 mm including a 1 mm marginal thickness.

Position-sensitive SiPMs with an active area of 3 x 3 mm^2 comprises a 6 x 6 sparse array, and the SiPM array is coupled with the LYSO crystal to read out the scintillated photons. The photon detection efficiency of SiPM is 35 %, and the gain is 1.25 x 10^6. Any signals from the two opposing PEM detector heads within the coincidence window (< 16 ns) are digitized as one decay event, and the energy and position data are listed sequentially in the computer memory. The event signals are digitized with data acquisition system, and a custom software package is developed to collect and visualize the event data. The XY position and non-uniformity calibration of crystal maps with a ^{22}Na flood-field source are performed. The measured energy resolution at 511 keV is about 15 %.

A simple back-projection technique is employed to reconstruct a finite number of projections of radioactive sources. The reconstructed 3D images are equidistantly divided into 15 perpendicular planes between the two opposing LYSO crystal detector surfaces as shown in Figures 3.1(b) and (c).

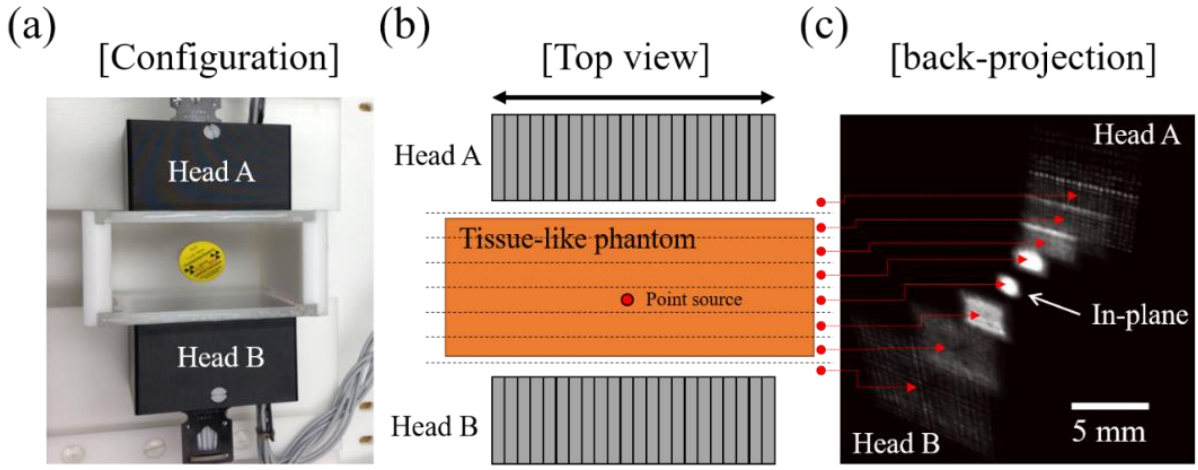

Figure 3.1 (a) Configuration of the two opposing MR-compatible PEM detector heads for imaging a coin-shaped ^{22}Na source. (b) Schematic top view of the PEM detector heads with a tissue-like phantom bearing a point source. (c) A 3D tomosynthetic image with 15 equidistant image slices is reconstructed from a simple back-projection method.

3.2.2. Dedicated breast coil with compression paddles

Previously, we have developed a dedicated breast coil for MR/scintimammography application. (121) The previous design is modified to insert our MR-compatible PEM detector heads and breast compression paddle assemblies. As seen in Figure 3.2(a), the solenoid quadrature breast coil consists of two parallel loops with a diameter of 150 mm. The copper trace pattern (width 5 mm, thickness 34 μm) pattern is fabricated on FR4 boards. The coil is tuned to the Larmor frequency of proton in the 3T magnetic field (127.7 MHz), and the impedance is matched to 50 Ohm with phantom loading using a network analyzer. Since the RF breast coil operates in a receive-only mode, the passive and active detuning circuits are controlled by PIN (positive-intrinsic-negative) diodes integrated into PCB to decouple the RF breast coils from the high-power RF transmission. (122) The MR signal is fed through a capacitive matching circuit and a balun circuit. A low-noise amplifier with 25 dB gain, 0.4 dB noise figure, and < 5 Ohm input impedance is also mounted in the coil interface box. To avoid physical contact with the breast and impedance with the breast compression mechanism, all the passive electronic components are covered by an acetal resin housing. [Figure 3.2(b)]

A major update to our dedicated breast coil is to utilize MR-compatible breast compression paddles for MR/PEM. [Figure 3.2(c)] In clinical practice, breast compression spreads overlaying tissues out such that it reduces the required dose while increasing image quality. (123) Our MR-compatible compression paddle screen (150 mm × 100 mm, thickness 3.2 mm) is made of Polycarbonate plastic plates that transparent to the 511 keV gamma-ray and visible light. These transparent paddle screens are supported by acetal resin frames that also allows mounting of our MR-compatible PEM detector heads. The compression paddles are installed in the space between the upper and bottom plates of our dedicated breast coil and no sharp edges are in contact with

breast tissue. [Figure 3.2(c)] The direction of the breast compression is designed to form the Cranial-Caudal (CC) view, as this view is commonly used in X-ray mammogram and emission mammograms such as Scintimammography and PEM. As seen in Figure 3.2(d), the custom-made housing of the imaging system is designed to support the chest allowing the breast to hang naturally. The upper plate with the two breast insertion holes is backed up by four distributed 1.5-inch diameter acetal resin pillars. The top loop of the breast coil is embedded into the acetal resin upper plate of the patient interface to minimize dead space between the chest wall and the FOV of PEM. The symmetric features allow installation of the PEM detector heads on both sides of the breast.

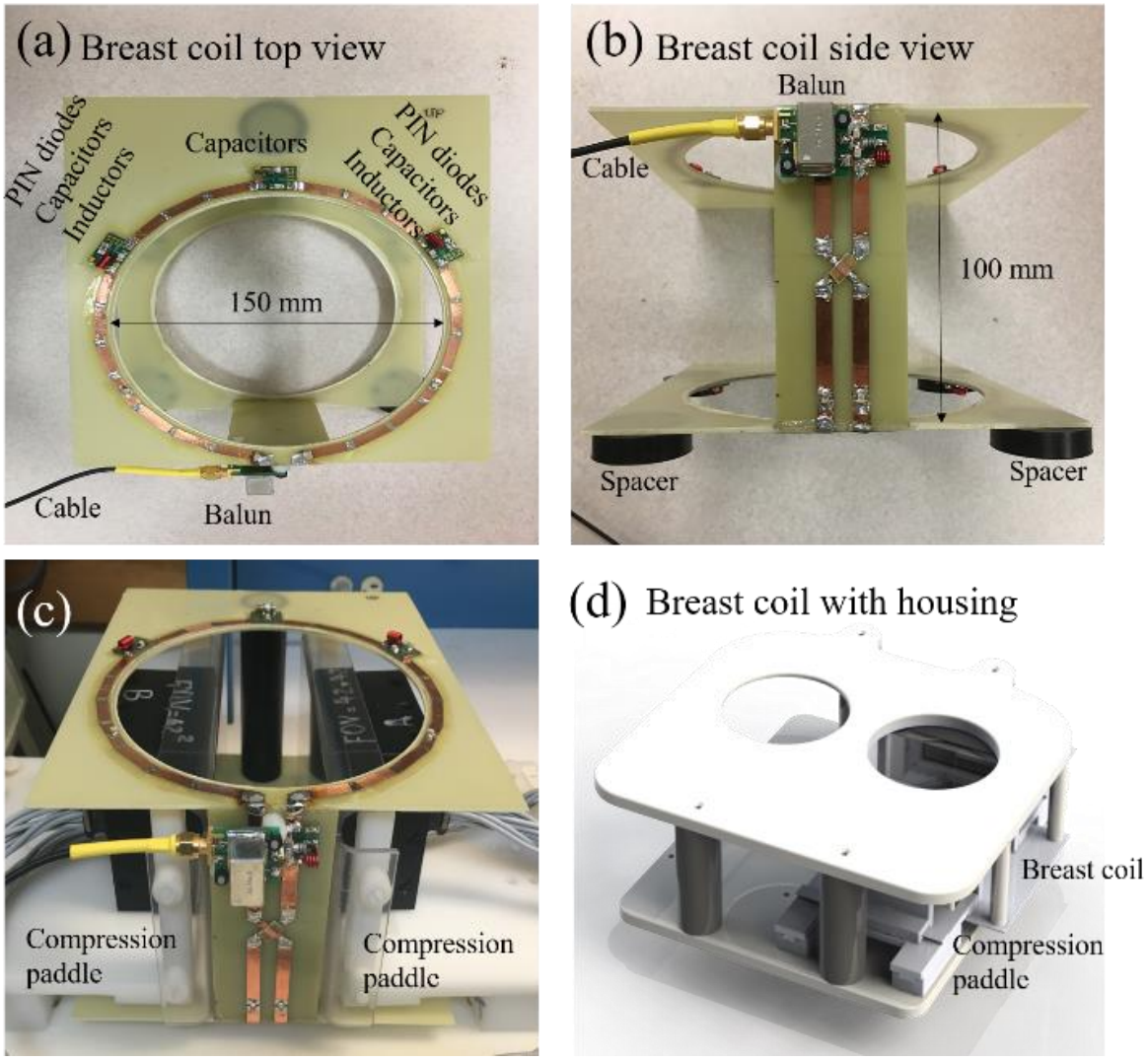

Figure 3.2 Pictures of our modified breast coil and mechanical housing. (a) A top view of our breast coil shows electronic components soldered on a coil frame and 150-mm diameter opening for breast insertion. (b) A side view shows a capacitively coupled output and a balun circuit. No electric component is mounted inner surfaces of the breast coil frame. (c) The compression paddles are designed to tightly fit in the inner space of the breast coil frame. The PEM detector heads are sitting behind the compression paddle screens. (d) A bird-eye view of our breast coil housing and compression paddles.

3.2.3. Fiducial marker for MR/PEM image registration

In multimodal imaging, a fiducial marker plays a major role in image data registration. (124-126) The MR/PEM system requires precise positioning of the PEM detector heads which is needed to measure the cancer therapy response. We design a fiducial marker that is visible in MR images to provide relative tumor locations. The fiducial marker is made of three layers of Polycarbonate plates. Two 3.2-mm thick plates sandwich a 6.4-mm thick plate with a 3×5 dot-patterned cavity with epoxy adhesives and plastic screws as shown in Figure 3.3(a). The 3×5 dot-patterned cavity is filled with a mixture of 10 mM $CuSO_4$, 70 mM NaCl, and distilled water. Two fiducial markers are placed behind the compression paddles as seen in Figure 3.3(b) and mechanically aligned with our PEM detector heads. This alignment provides the relative position information of the PEM detector heads and allows straightforward image data registration.

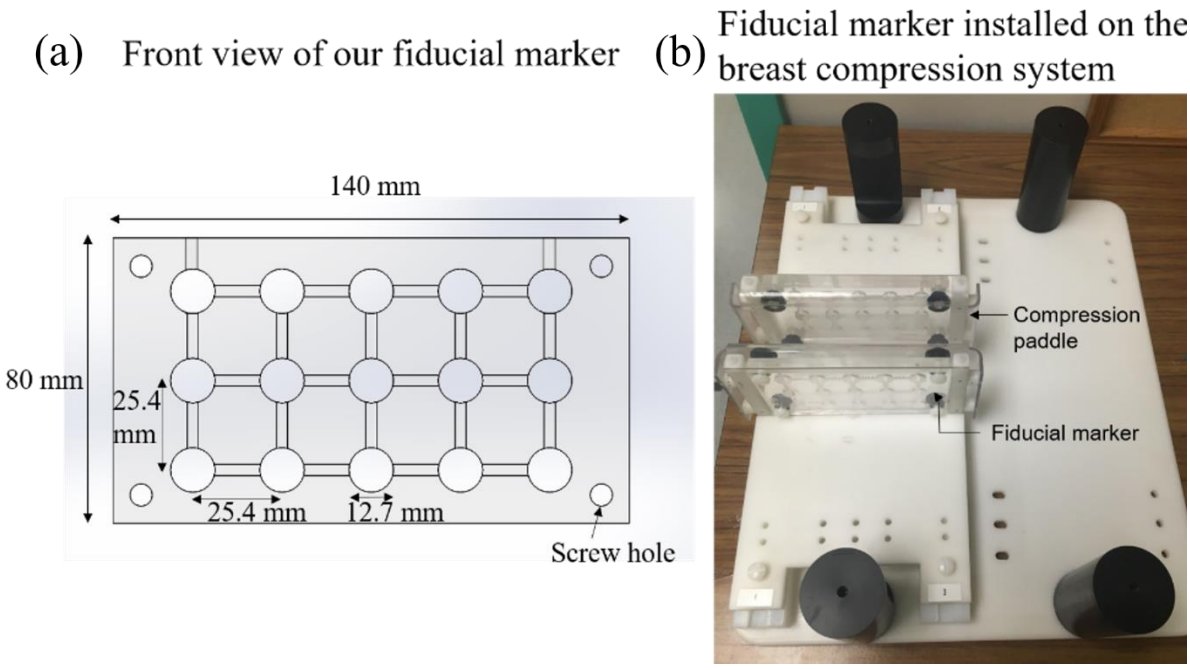

Figure 3.3 (a) A front view of the multimodal fiducial marker with 3×5 dot-pattern grid. (b) The two multimodal fiducial markers are installed behind the compression paddle screen.

3.2.4. Patient positioning and hardware configuration

Patient positioning is key to successfully perform breast MRI (17) and as well as PEM. (127) The patient lies face down in a prone position atop the MR/PEM system with their forehead resting on the head support and arms comfortably stretched above their head. The breast is carefully positioned and gently compressed in the MR/PEM system. Cables stemming from PEM detector heads and MR breast coils are run below an opening on the bottom part of the leg support. The data acquisition system of PEM sits on the patient table with a CAT 5 ethernet cable to connect to the control computer in the MRI console room. The patient positioning and hardware configuration is illustrated in Figure 3.4.

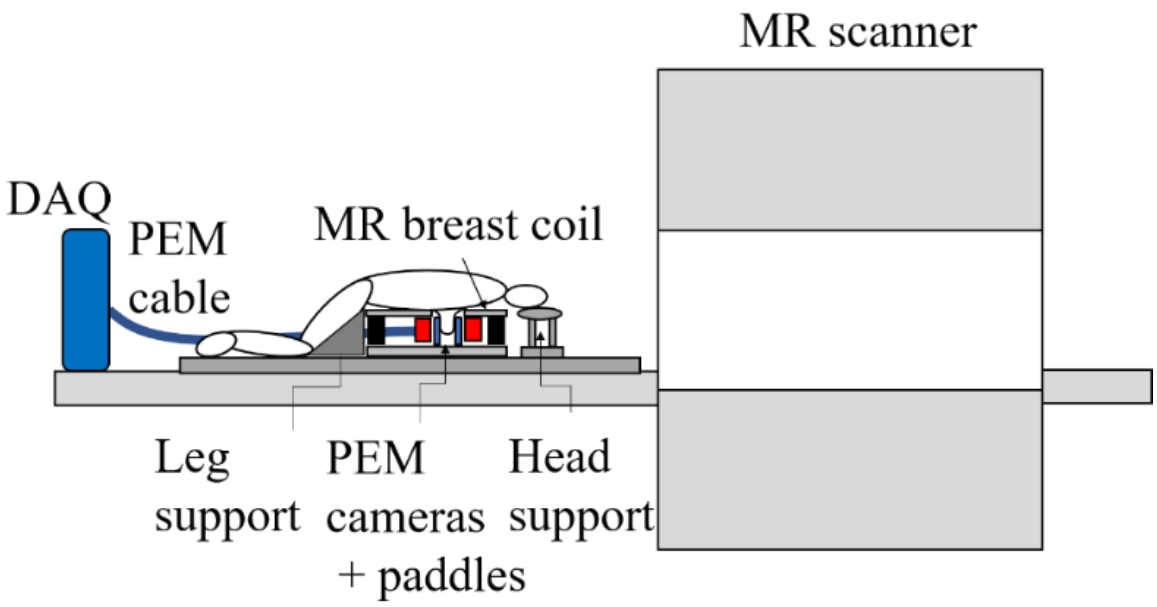

Figure 3.4 Patient positioning and hardware configuration of our sequential MR/PEM dual-modality imaging system.

3.2.5. The procedure of therapy monitoring using MR/PEM

For optimal MR/PEM breast cancer therapy monitoring, a dual-modal imaging procedure is proposed. First, the patient receives an intravenous (IV) ^{18}F-FDG injection. Since the uptake time of ^{18}F-FDG is around 30 to 60 min, MR imaging competes during this uptake time. For the breast MRI, the patient is scanned breast MRI during the ^{18}F-FDG uptake time. For breast MRI, the patient is positioned on the patient table, with the breast immobilized by the compression paddles. An MRI fiducial marker is placed behind the compression paddles. Then the patient is brought inside the MR magnet and scanned with a fiducial MR scan that can localize the fiducial marker and the breast. After that, one pre-contrast MR image and two post-contrast MR images are acquired. The patient is then brought out from the magnet, and the lesion can be targeted by comparing the fiducial scan and dynamic scan images. The technician locates the PEM detector heads at the hot spot. The block diagram of our MR/PEM imaging procedure is illustrated in Figure 3.5.

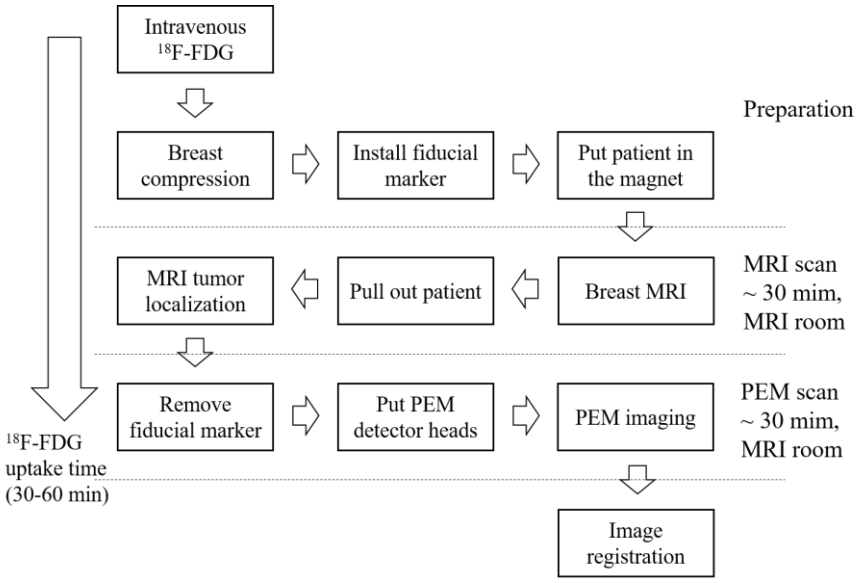

Figure 3.5 Our MR/PEM dual-modality imaging procedure for breast cancer therapy monitoring.

3.2.6. Compressible gelatin phantom

A cylindrical compressible breast phantom (diameter 90 mm, height 100 mm) is fabricated using porcine gelatin powder (175-bloom, Sigma-Aldrich Corp., St. Louis, MO, USA). The porcine skin powder (30 grams) is added to ~40 °C of distilled water (300 mL) and cooled down for 10 hours at 4 °C in a cylindrical phantom mold. A vertical hollow slot is made to insert a ^{22}Na point-like source as shown in Figure 3.6(a). The experiments are performed using a Philips 3T Achieva MRI scanner. The reported T1 relaxation time for fat and glandular tissue are 366.78 ms and 1444.83, respectively and the reported T2 relaxation time for fat and glandular tissue are 52.96 and 54.36, respectively. (128) The reported T1 and T2 time for porcine gelatin phantom are 853 ms and 55 ms, respectively.(129). The gamma-ray attenuation is (-0.4 dB/mm), which is close to the reported gamma-ray attenuation of the breast. (130)

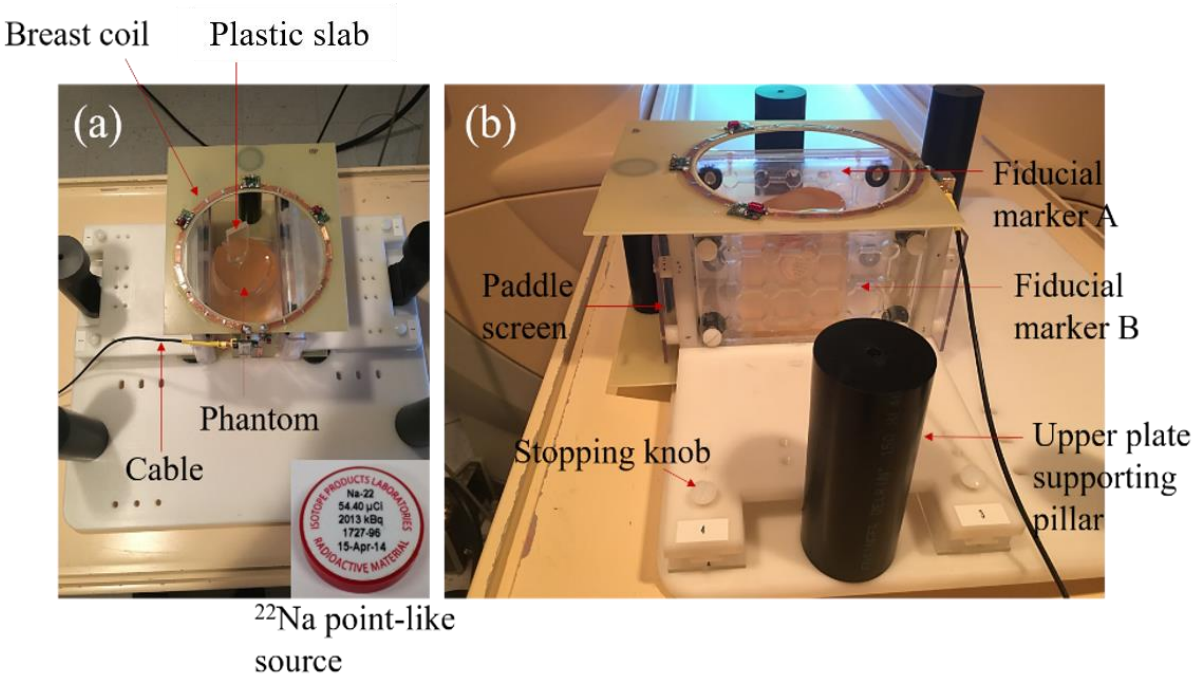

Figure 3.6 Pictures of the MR/PEM phantom setup with a compressible gelatin phantom bearing a ^{22}Na-source. The upper plate of the MR/PEM system is removed to visualize the MR coil and compression plates. (a) Gelatin phantom sitting inside our breast coil and immobilized by compression paddles. A plastic slab is used to make room for a coin-shaped ^{22}Na-source that is shown in the inset picture on the bottom right side. (b) The ^{22}Na-source is inserted to the compressible gelatin phantom, and two fiducial markers are installed behind the paddle screens. Stopping knobs are employed to control the compression distance between the two paddles.

3.3. Results

3.3.1 Point spread function of PEM images

The point-spread-function (PSF) of our PEM system is measured to assess the spatial resolution of our PEM system in the 3T magnetic field strength. Two experiments are performed with a single source and two sources. The point-like ^{22}Na source is centered between the two opposing PEM detector heads in free space as shown in Figure 3.1(a). The in-plane image slice is chosen to evaluate the PSF of our PEM system. Note that other image slices are not intended to view clinically. As shown in Figure 3.7(a), the point-spread-function (PSF) of reconstructed images at the opposing detector distance of 50 mm is about 1.5 mm with a point-like ^{22}Na source, which shows 2.5 times better spatial resolution compared to the whole-body PET scanner. The actual radioactivity of the ^{22}Na source and the integration time of PEM are 1 MBq and 5 min, respectively.

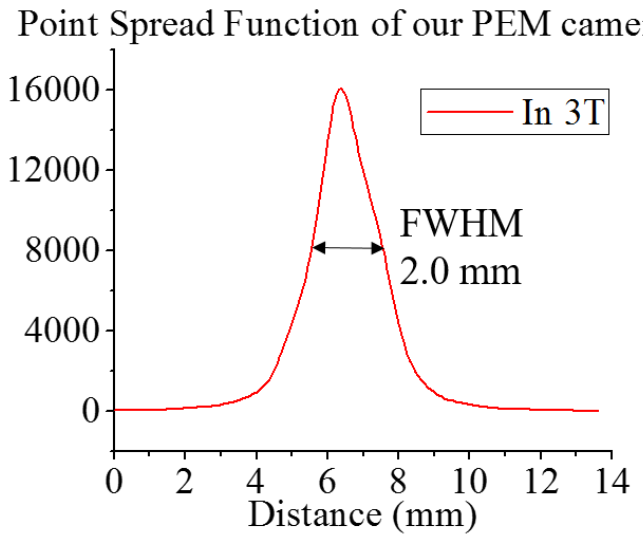

Figure 3.7 Point spread function of our PEM system at in-plane measurement in the 3T magnetic field.

3.3.2. MRI compressible phantom study

MR images are collected using a cylindrical compressible phantom with our previously developed multimodal breast coil. The breast coil and phantom are positioned at the isocenter of a 3T Philips Achieva Scanner. MR images are acquired in axial and coronal planes [Figure 3.8]. All MR images are acquired with a standard gradient-echo sequence (TE 1.3 ms, TR 11.0 ms, flip angle 90°, slice thickness 2 mm, matrix size 512 × 512, FOV 200 mm). For the axial MR images, two 2D slices are acquired. An axial MR image from the fiducial marker is shown in Figure 3.8(a) showing the distinctive 3×5 dot-patterned grid. For coronal MR images, two sets of 64 images are acquired. The first round of images is taken from the cylindrical phantom positioned at the center of our breast coil, while the other set of images come from the phantom positioned 30 mm off the center of the coil to the left side. An image slice from the first set is shown in Figure 3.8(b). Two opposing dot patterns appear on the MR images which determine a relative location of the compressed cylindrical phantom. A space inside the phantom indicates a coin-shaped point-like ^{22}Na source. The ^{22}Na source is located around the middle of the dot patterns of the fiducial markers. An image slice from the second set is shown in Figure 3.8(c). Likewise, the MR image shows the fiducial markers and the phantom bearing the ^{22}Na source, but the position of the phantom is shifted 30 mm to the left on the MR image. The relative position of the ^{22}Na source is between the first and the second dots from the left.

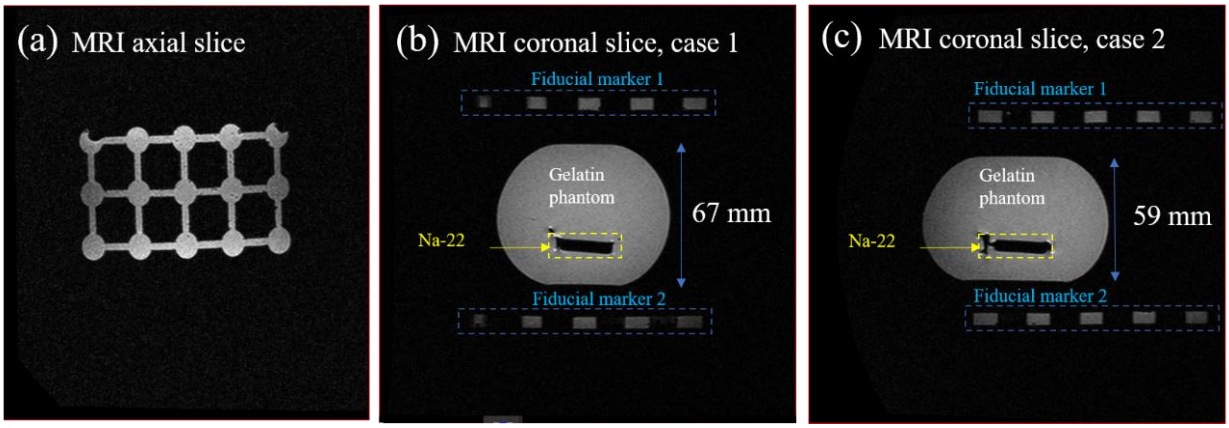

Figure 3.8 T2-weighted gradient echo images of the fiducial markers and compressible cylindrical phantoms in different image planes. (a) Axial 2D MR image from one of the two fiducial markers displaying a distinctive dot pattern in MR images. (b) Coronal 2D MR image from two fiducial markers and the compressed cylindrical phantom centered in the breast coil. (c) Coronal 2D MR image from two fiducial markers and the compressed cylindrical phantom 30 mm off the center of our breast coil.

3.3.3. Dual-modal MR/PEM imaging

Initial evaluation of our MR/PEM imaging performance is performed using a cylindrical phantom bearing a point-like ^{22}Na source with 1 MBq radioactivity. As aforementioned, MR images are acquired and analyzed before the technician positions the PEM detector heads in the expected hot spot. The position of the ^{22}Na point-like source can be seen in the first MR image set as shown in Figure 3.8. Then, two opposing PEM detector heads are placed at the center of the fiducial markers such that the centers of FOV of our PEM detector heads are aligned with the center of the fiducial markers. For this dual-modality system, the MR and PEM imaging are used sequentially in a single examination and therefore do not affect the performance of the individual imaging system. A spatial imaging data registration is performed as shown in Figure 3.9(a)-(c). ImageJ is used for rendering 3D images and overlaying dual-modality images. (131) A 3D volume

image comprised of 64 coronal slices is shown in Figure 3.9(a). The fiducial markers and the slightly compressed phantom shapes are visible in the MR images. A 3D PEM image from the point-like ^{22}Na source is shown in Figure 3.7(b). Since the fiducial markers indirectly display the location of the PEM detectors, simple image translations and rotations are applied for registering PEM image to MRI.

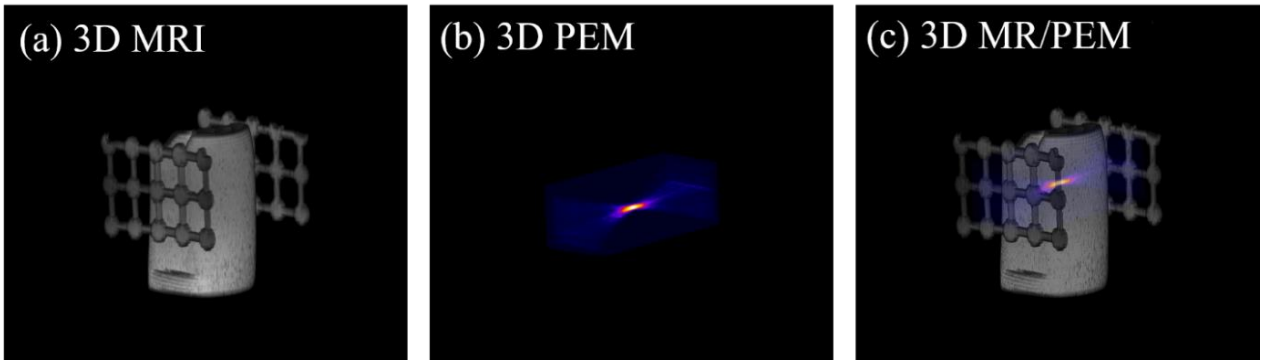

Figure 3.9 (a) 3D MRI image from 64 image slices of the fiducial markers and the compressible phantom. (b) 3D PEM image from 15 image slices of the compressible phantom bearing the point-like ^{22}Na source. (c) 3D MR/PEM overlay image from the fiducial markers and the compressible phantom.

3.3.4. Volunteer study using the MR/PEM system.

We have performed MR/PEM using both Gd-DTPA and ^{18}F-FDG on a volunteer. First, the breast is immobilized between the compression paddles and the complete set of T1-, T2- and DCE-MRI data is collected after the injection of Gd-DTPA. Once the MR images are collected, ^{18}F-FDG is injected, and the volunteer takes a rest for 30 minutes. Following that the PEM detectors are positioned, and the data is acquired. As the volunteer in this study has no lesion visible in the MRI, the PEM detectors are placed in an arbitrary position. For breast cancer patients, PEM detectors will be positioned based on the location of the lesion obtained from the MR images. Three sets of

PEM data are collected each lasted 10 minutes. For this case, the compression paddles are positioned 52 mm apart, and the detectors are 2.5 cm behind the compression paddles. In Figures 3.10 3.11, the results are presented as 15 slices equidistantly positioned.

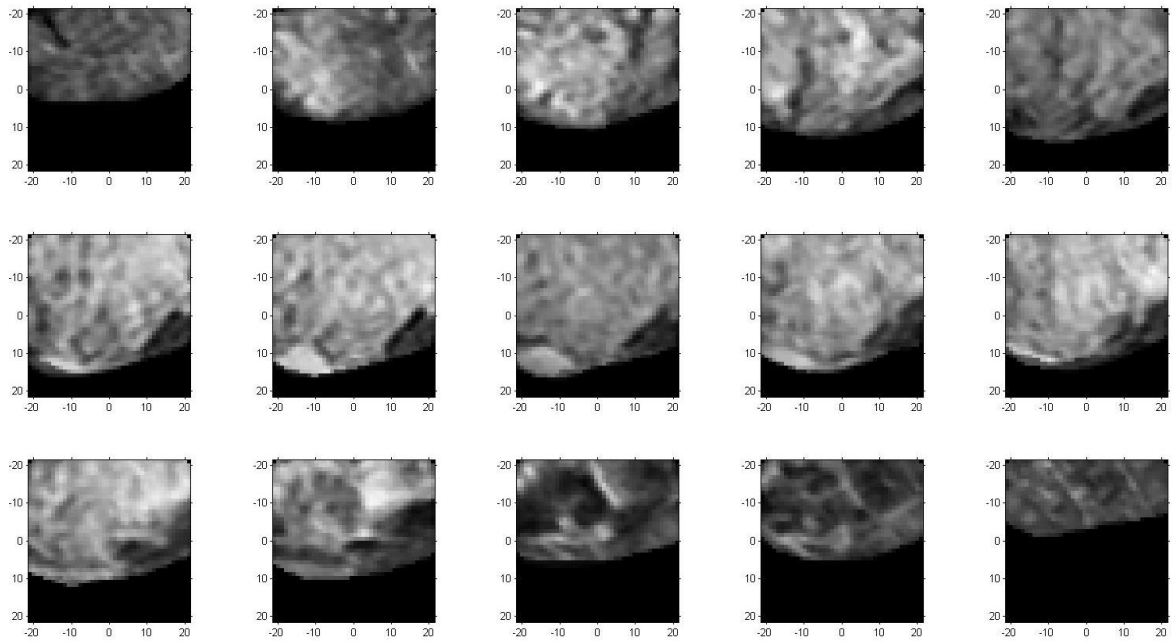

Figure 3.10 T1-weighted MR images within the volume of interest. Note that the MR images are down-sampled to the PEM resolution for image registration purpose.

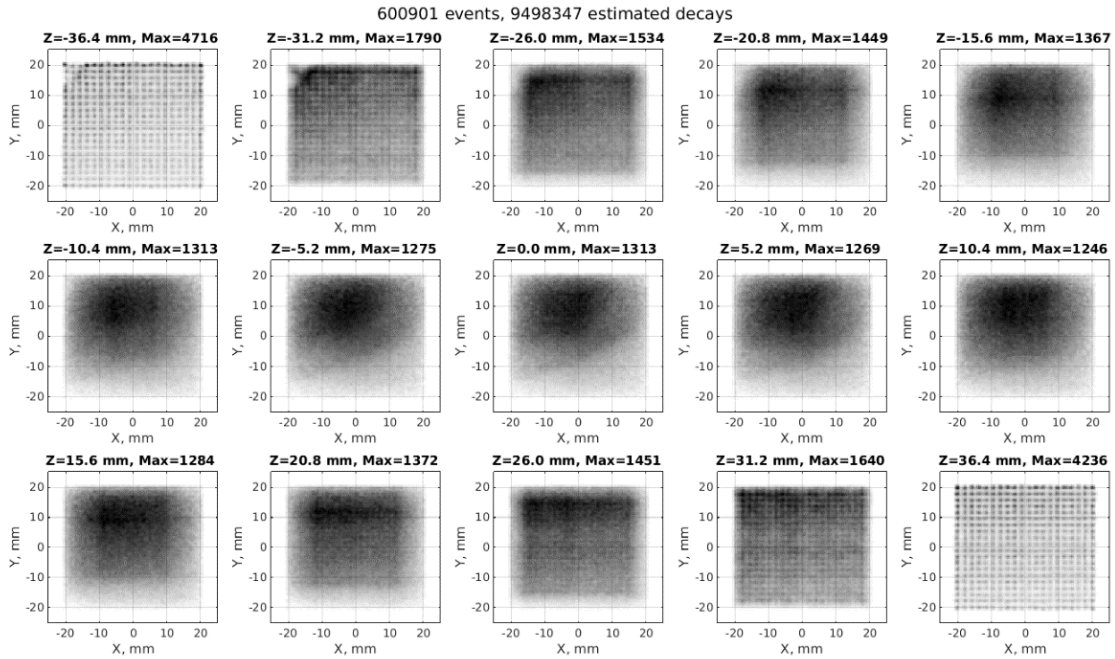

Figure 3.11 Backprojection imaging of PEM.

3.3.5. Comparison of MR images acquired using Philips Breast coil and our breast coil.

The MR/PEM interface is tested with several volunteers. With each volunteer, we improve and optimize the multi-modality imaging procedure. In our final trial, we successfully inject the volunteer with both Gd-DTPA and ^{18}F-FDG for MR/PEM imaging and acquire a complete data set. The images below demonstrate that the performance of our single channel breast coil is similar to the performance of the commercial Phillips MRI breast coil. This step is necessary to continue with the PEM imaging since the MR information is used as a priori information for the PEM reconstruction. The figures below compare the T1- and T2- weighted images for the same volunteer for both MR coils. Only selected slices are given here due to space limitation. Please note that since the volunteer are repositioned for the imaging session with the commercial and our single channel breast coils, images from the same breast are not identical one to one.

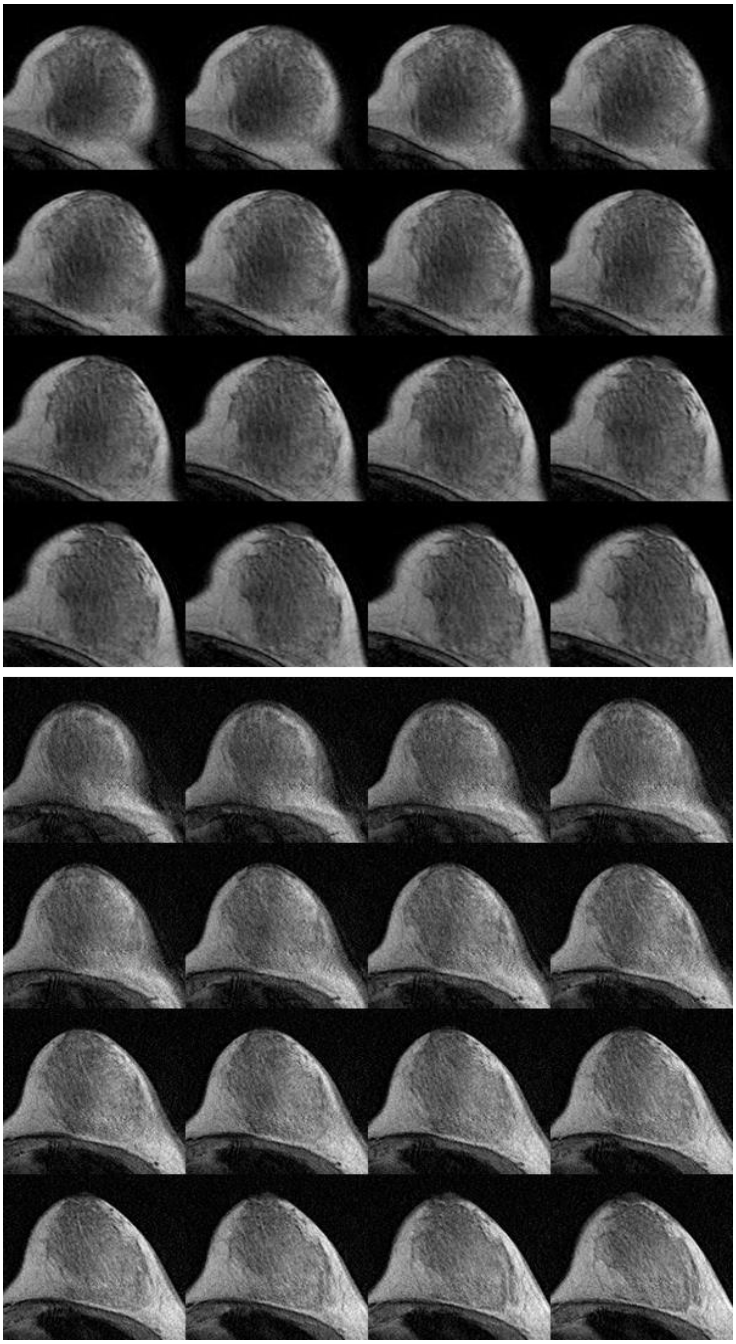

Figure 3.12 Comparison of T1-weighted MR images acquired using Philips Breast coil (top) and our single channel breast coil (bottom).

3.4. Discussion

In this chapter, we demonstrate the performance of our sequential MR/PEM system for the therapy response monitoring of breast cancer without a major modification on both sides of MRI and PEM in this proof-of-concept study. Our novel dual modality system design allows a straight forward imaging data registration using the first acquired MRI data before installing our MR-compatible PEM detector heads in the known hot spot. In addition, our novel MR/PEM system can facilitate better characterization of lesions and may have the potential to improve specificity without compromising in sensitivity in early detection of breast cancer. For the early cancer diagnosis, a larger FOV of the PEM system is required, and our PEM system will be upgraded to cover whole breasts in the future.

Our PEM system has shown 2.5-fold improved spatial resolution (2 mm) compared to a conventional whole-body PET scanner (5 mm). The limiting factor of the spatial resolution is the actual pixel size of the crystal face (2×2 mm^2). An advanced iterative image reconstruction method can be employed to improve the image quality. (132, 133) However, this approach comes at the cost of greater computation power for an iterative statistical image reconstruction method. Another possible way to increase the spatial resolution is to obtain a time-of-flight information. (134-136) However, it poses another challenge such as the susceptibility to dark counts in multi-pixel detectors. (137, 138)

Our first MR/PEM dual-modality imaging for the breast cancer therapy monitoring has several benefits over a conventional PET/MRI and standalone PET or MRI. First, our MR/PEM approach can substantially reduce the required dosage of radioactive tracers. (139) Also, the increased spatial resolution in PEM scanning from 5 mm to 2 mm can help minimizing the partial volume effect lowering the required dose while breast MRI provides supplementary information

of excellent soft tissue contrast (breast tissue) and molecular behavior that PEM cannot perform.

Secondly, our MR/PEM system employs a one-of-a-kind breast compression paddle and fiducial marker design that improves image quality in PEM but also stabilizes the breast tissue motion during breast MRI scans. This is beneficial when it comes to sequential dual-modality imaging because the patient might move slightly, but the breast will be stationary after two imaging scanning of PEM and MRI. Note that gentle compressive pressure will be applied to immobilize the breast and the effect of the paddle pressure on the breast MRI quality will be investigated in the future.

Last, unlike combining whole-body PET and MRI scanners into a single scanner, our approach requires minimal modification of existing MRI hardware allowing translation of this technique to clinical applications where the fast and accurate multimodal imaging data is needed. This innovative imaging system would be an economical alternative to stand-alone nuclear medicine imaging systems as it can be seamlessly used with any existing commercial MRI systems.

3.5. Conclusion

We demonstrate in this proof-of-concept study of MR/PEM cancer therapy monitoring for clinically aggressive molecular subtypes of breast cancer. For future work, the FOV of our PEM system will be expanded to cover the whole breast, which simplifies the imaging procedure by removing the PEM detector positioning and the breast MR image analysis before the PEM scan. Our dedicated breast coil will be updated to match the scanning speed of commercial parallel image acquiring breast coils. Ultimately, our system will be updated to operate in a simultaneous data acquisition mode for better temporal resolution, reduced imaging time, and dynamic dual-modality MR/PEM imaging.

Chapter 4: Development of dual-channel breast coil for MR/PEM multimodal imaging system

4.1. Introduction

Positron emission mammography (PEM) is an emerging molecular imaging technique for breast cancer detection and diagnosis using downsized gamma detection heads and compression paddles. (116, 118, 119) PEM has demonstrated high specificity and sensitivity up to 90 % with an improved spatial resolution which is hard to be achieved by conventional whole-body PET scanners. PEM shows a great potential in detecting early stage cancers and ductal carcinoma in situ (DCIS), which is hard to be achieved by conventional whole-body PET scanners. (119) However, standalone PEM has difficulty in imaging of the specific tissue uptake of the nuclear medicine in a large FOV due to the trade-offs made between the detection efficiency and the spatial resolution. Also, PEM suffers from high false-positive because of fibroadenomas, fibrocystic changes, and fat necrosis. Therefore PEM requires image-guided tissue biopsy capabilities. (140)

Meanwhile, magnetic resonance imaging (MRI) is a widely used non-invasive imaging modality that provides not only whole-body anatomical information with the high spatial resolution but also localized physiological metabolic activities with dynamic contrast-enhanced MRI (DCE-MRI), diffusion-weighted imaging (DWI) and MR spectroscopy (MRS) techniques. However, MRI suffers from substantially lower sensitivity (~10^5 fold) compared to radiotracer-based molecular imaging techniques such as PET, SPECT, and PEM. Thus, PEM in conjunction with MRI (henceforth MR/PEM) may offer a robust solution to breast cancer detection, diagnosis, and treatment monitoring with respective advantages. Additionally, MR/PEM can provide multi-dimensional co-registration of imaging data for in-vivo characterization of cancer biology and a

better understanding of in-vivo molecular pathways in cancer processes.

The key to a successful MR/PEM system design is to develop a dedicated MR radio-frequency coil (henceforth breast coil) for breast imaging. This breast coil is required to be assembled with PEM detector heads on the front-end of the imaging system, and it should provide high-sensitivity and large field-of-view without sacrificing essential imaging qualities. Several critical engineering concerns should be considered for designing the breast coil to maximize the synergetic effects of combining PEM and MRI. First, electromagnetic interference (EMI) should be carefully managed not to affect the imaging performance of each imaging modality. Next, the presence of extremely high magnetic field should not deteriorate the PEM information. Then last, data acquisition of each modality needs to be running fast enough and allows to capture information within a reasonable time.

In the previous chapter, we have successfully demonstrated our novel MR/PEM system for the therapy monitoring of breast cancer without deteriorating EMI effects. The optimal geometry, orientation, and design of the breast coil vary with the size, anatomy, and applications. Since a single RF coil loop of diameter *d* gives the highest possible SNR for a volume at depth *d* inside an imaging volume of the coil loop, (141) the rapid and wide acceptance of the solenoid coils for large volume imaging applications such as breast imaging is reasonable. However, the solenoid coil is a volume coil in nature that is susceptible to geometrical dimensions and has a moderate signal-to-noise ratio (SNR). Also, the limitation of the previous solenoid coil design is the lower temporal resolution for DCE-MRI sequence and lower SNR than commercial multi-channel breast coils due to the single channel construction of the breast coil. The elongated MR scanning time limits patient access and increases cost. Furthermore, the longer the scanning time takes, the more the data acquisition is susceptible to motion artifacts.

Multiple channel RF coil has been introduced as a solution for improving the SNR and B1 field homogeneity as well as reducing the dielectric effects at high field (>3T) MRI application. Modern 3T MRI system uses parallel imaging methods with multiple RF coil channels to accelerate the acquisition of image data. (142-144) The MR parallel imaging is characterized by acquiring a reduced amount of frequency bandwidth in k-space with an array of RF receiver coils. The challenge of designing multiple channel arrayed coil is minimizing or eliminating the mutual inductance between coil loops. If the RF coil loops tuned to the same resonance frequency are placed close each other, the mutual inductance causes the resonance peak to split, which results in reduced sensitivity and SNR in MR images. In this chapter, we improve the design of the dual-channel breast coil, achieve high temporal resolution, and enhance the signal-to-noise ratio for MR/PEM system.

4.2. Methods

4.2.1. Single Channel solenoid breast coil vs. Philips SENSE 4-channel breast coil

As described in the previous chapter, we have developed the single-channel solenoid coil consisted of two antenna loops for our MR/PEM multimodal molecular imaging system. In this section, we evaluate the performance of our new single channel solenoid coil with its coil housing interface. A commercial-grade clinical breast coil for 3T MRI coil, Philips SENSE 4-channel breast coil, is used for the comparison study. It is important to note that we only used one side of the breast for a fair comparison. In other words, Philips SENSE 4-channel breast coil uses two channels for each side of the breast, while our breast coil uses one channel for the one side of the breast.

4.2.2. Dual-channel breast coil

The saddle coil loop is oriented on the x-axis, while the solenoid loop channel is aligned on the y-axis ss shown in Figure 4.1(a). A circular opening made of the solenoid breast coil loops has a diameter of 15 cm and height of 10 cm, which also allows for insertion of the breast and PEM detector heads. The saddle coil is inserted between the two opposing loops of the solenoid coils, and the resonance frequency is tuned to the Larmor frequency of proton in 3T. The mutual inductances between the two coils are suppressed by using low input impedance low-noise preamplifiers. (141) Our dual-channel breast coils are the receiver only coils employing combined passive/active detuning circuits to decouple the coils from the RF transmitter. Each coil loop was etched on FR4 laminate board using copper strips of 0.0341 mm thickness and mounted on an acrylic plate with the material within the loops removed to allow for insertion of the breast. The separation space between the plates of the vertical coil loops allows for insertion of the saddle coil loops (height, 9 cm) and PEM detector heads through the side of the vertical circular coil loops. The newly developed transverse saddle coil loops are based on the same materials and electric components with the vertical circular coil loops. A circular opening made of two facing saddle coil loops has a diameter of 15 cm, which also allows for insertion of the breast, and the materials within the saddle coil loops are removed to secure the space for insertion of breast compression paddles. The saddle coil is designed to be removed without the patient repositioning to facilitate the workflow of our MR/PEM cancer therapy monitoring application. As shown in Figure 4.1(b), (c), and (d), the saddle coil is designed to be detachable not only to perform high sensitivity MR imaging but to also secure space between the quadrature solenoid loops to accommodate PEM detector heads for MR/PEM imaging.

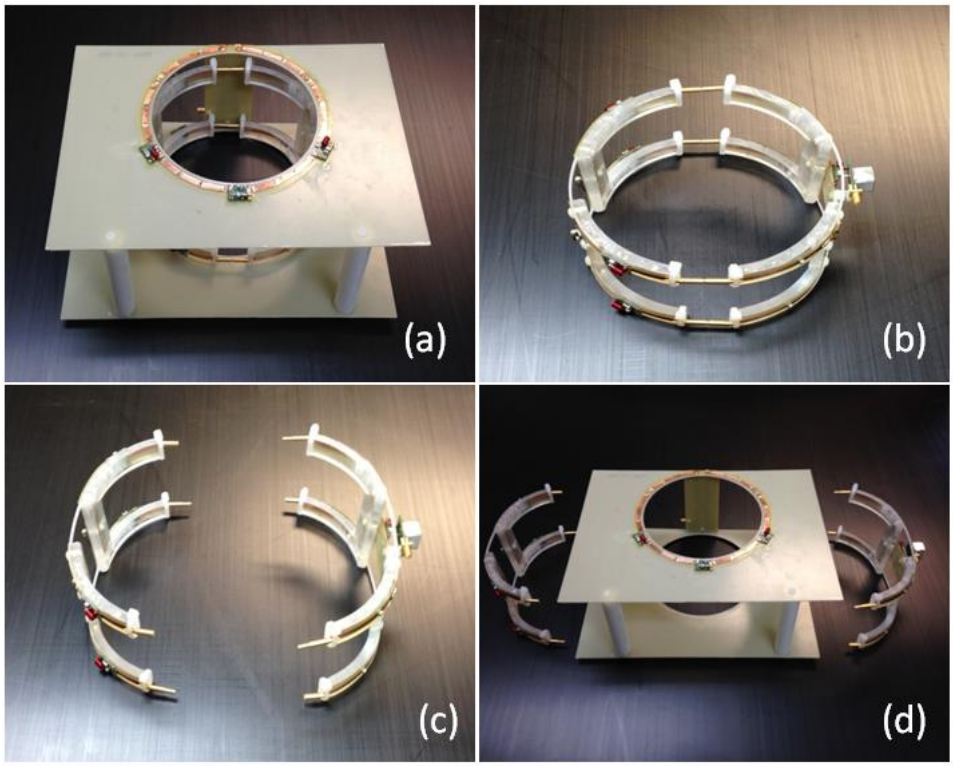

Figure 4.1 Pictures show new dual-channel breast coil design for our MR/PEM therapy monitoring application. (a) Dual-channel breast coils consist of a one-channel solenoid coil and a one-channel saddle coil. (b) Our new saddles coil consists of two coil loops connected with MR-compatible circular connectors. (c) The saddle coil is separate into two semi-cylinder to make it detachable without patient repositioning. (d) There are space for PEM detector head positioning and breast compression paddles between the top and bottom plates of the solenoid coil after removing the saddle coil from the solenoid coil.

4.2.3. MR/PEM hardware configuration

As shown in Figure 4.2(a), we have developed a prototype MR/PEM interface for our new dual-channel MR breast coil. MR/PEM imaging with dual-channel breast coil is split into three steps. The high sensitivity MR imaging is performed with the dual-channel breast coil including the solenoid and saddle coils [STEP 1] as shown in Figure 4.2(b), and healthcare provider removes the detachable saddle coil from the MR/PEM system without repositioning the patient [STEP 2]. MR/PEM imaging is performed sequentially with the solenoid coil only and the PEM detector heads [STEP 3]. Based on the location of the tumor identified from MRI, the PEM detector heads can be positioned to collect the imaging data at the hot spot.

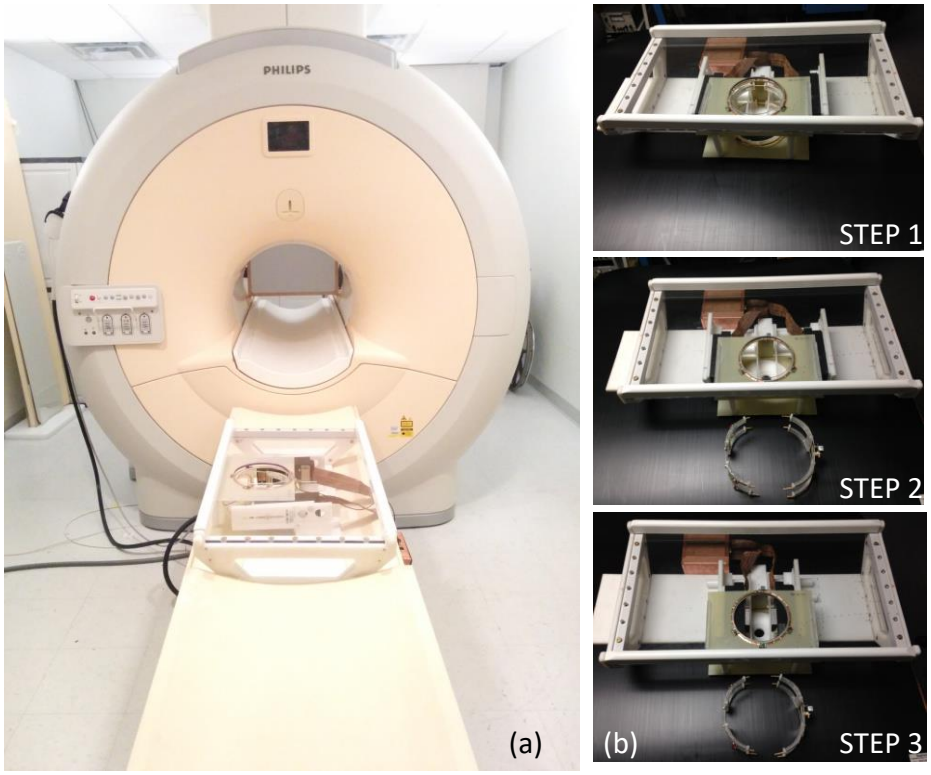

Figure 4.2 (a) A newly developed prototype for our MR/PEM cancer therapy monitoring application. (b) Imaging procedure splits into three steps. High SNR MR breast imaging with dual-channel breast coils [STEP 1]. Healthcare provider removes the detachable saddle coil from the MR/PEM system without patient repositioning [STEP 2]. Moderate SNR MR breast imaging with single-channel solenoid coil and simultaneous PEM data acquisition [STEP 3].

4.2.4. MRI experiments

Three sets of MR images are acquired using our dual-channel breast coil, our single-channel solenoid coil, and Philips SENSE 4-channel breast coil with a 3T Philips Achieve MR scanner (Philips Medical Systems). The transverse images of a breast phantom (diameter 12 cm) are used for the SNR comparison. The SNR of the local FOV is calculated using Equation (4.1).

$$SNR = \frac{S_{avg} - N_{avg}}{N_{std}} \qquad (4.1)$$

where, SNR is the signal-to-noise ratio, S_{avg} is the average intensity of signal defined by the mean intensity of pixels from the signal ROI. N_{avg} is the average intensity of noise measured from the background noise pixels. N_{std} is the standard deviation of the background noise.

The integral uniformity (IU) is computed by using Equation (4.2) where the maximum and minimum values of signals are measured from the pixels within the phantom signal.

$$IU = \left(\frac{S_{\max} - S_{\min}}{S_{\max} + S_{\min}} \right) \qquad (4.2)$$

where, S_{max} and S_{min} are the maximum and the minimum signal intensities of the breast phantom, respectively. It is important to note that for a given coil, the lower the IU, the better its MR image uniformity. We used a T1-weighted gradient echo sequence with the parameters: FOV = 120 × 120 mm, matrix size 512 × 512, echo time (TE) = 5 ms, repetition time = 100 ms, flip angle = 30º and 90º, slice thickness = 2 mm, and number of signal averages (NSA) = 1. MRI data were acquired without PEM detector heads to allow a fair comparison study.

4.3. Results

An MR image of the breast phantom is shown in Figure 4.3. A region-of-interest (ROI) is defined to calculate the SNR. Almost 80 % of the pixels from the breast phantom MR images are used for the SNR calculation. The background noise and standard deviation are measured outside the breast phantom MR signal and avoided any ghosting signal caused by MR scanner artifacts. The SNRs of our single-channel solenoid coil, our dual-channel breast coil, and Philips Achieva SENSE 4-channel coils are presented in Table 4.1. For the flip angle 30°, the measured SNRs for our single-channel solenoid coil, our dual-channel breast coil, and Philips SENSE 4-channel coils are 90, 134, and 112, respectively. For the flip angle 90°, the SNRs for our single-channel solenoid coil, our dual-channel breast coil, and Philips SENSE 4-channel coils are 112, 156, and 140, respectively for the flip angle 90°. The relative SNR of our single-channel solenoid coil and dual-channel breast coil to Philips SENSE 4-channel coil was 0.8 and 1.2, respectively. Coronal and transverse MR image sliced from the breast phantom with different MR breast coils are presented in Figure 4.4. Centerlines are drawn at given MR image slices to measure the maximum and minimum signal intensities of the MR images. For the coronal plane, the calculated IU for our single-channel solenoid coil, our dual-channel breast coil, and Philips SENSE 4-channel breast coil are 0.16, 0.27, and 0.28. For the transverse plane, the calculated IU for our single-channel solenoid coil, our dual-channel breast coil, and Philips SENSE 4-channel breast coil are 0.03, 0.21, and 0.15, respectively. MR imaging of the breast phantom yields interesting findings. Our novel dual-channel breast coil shows the best performance regarding the SNR, while our single-channel solenoid coil has the best IU from the breast phantom MR experiments.

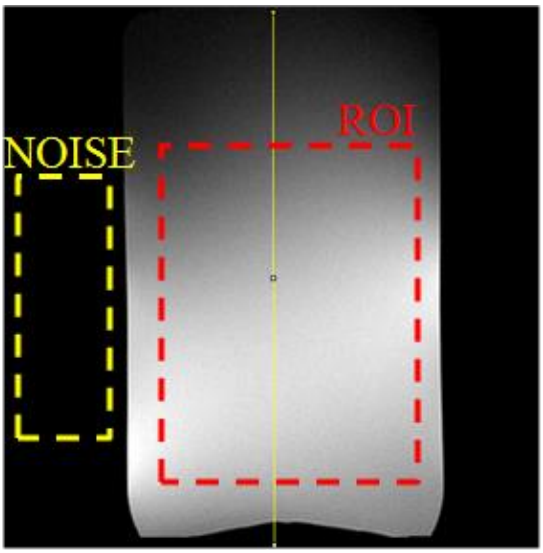

Figure 4.3 A rectangular region-of-interest (ROI) is drawn over the middle 80 % of the phantom breast images (red-dashed box) to compute the SNR of the MR images, while the average noise intensity and the standard noise deviation are measured from the background in the yellow dashed box.

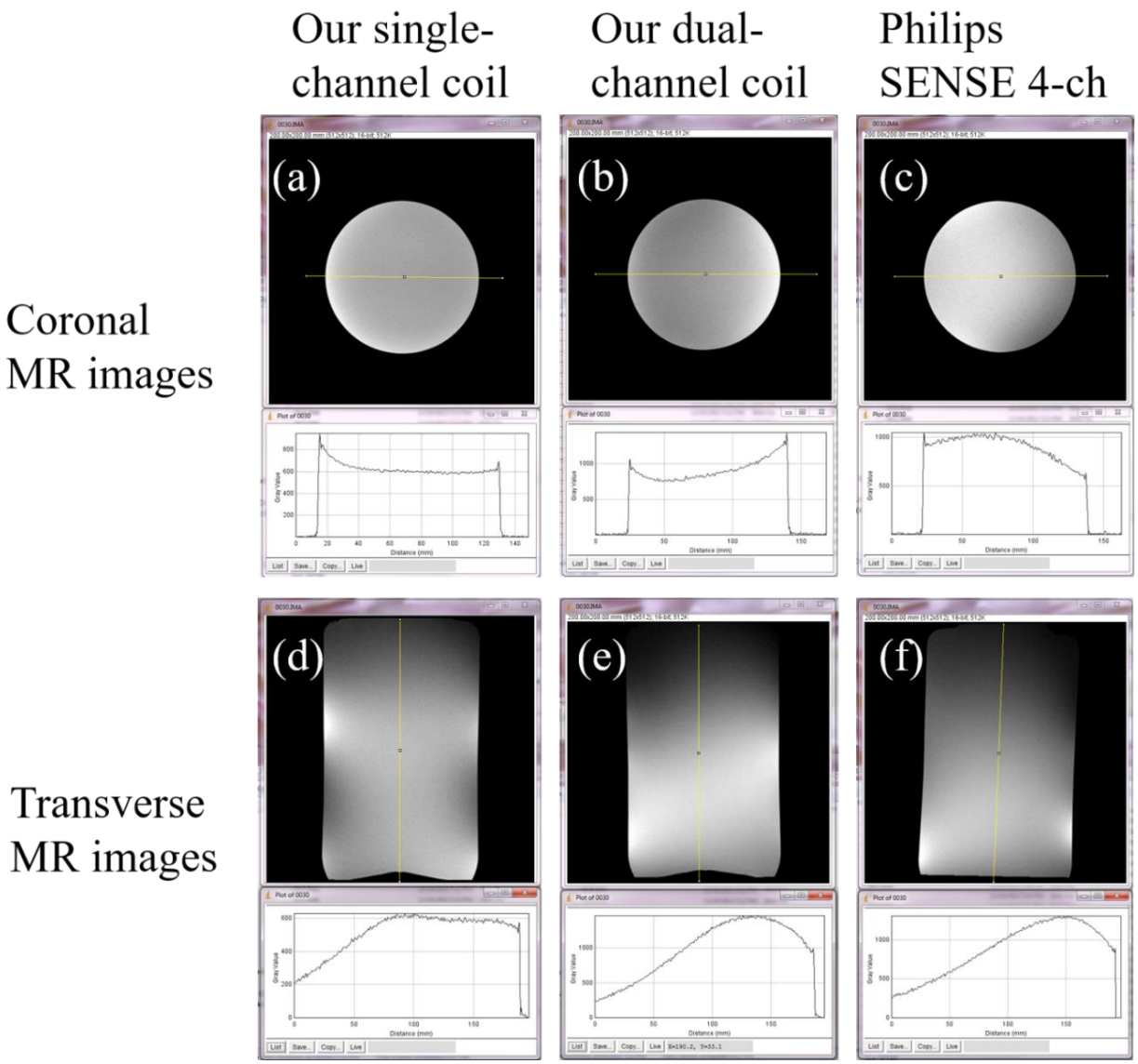

Figure 4.4 Coronal 2D MR images with the intensity plots along the solid yellow lines from (a) our single-channel solenoid coil, (b) our dual-channel breast coil, and (c) Philips SENSE 4-channel breast coil. Transverse 2D MR images with the intensity plots along the solid yellow lines from (d) our single-channel solenoid coil, (e) our dual-channel breast coil, and (f) Philips SENSE 4-channel breast coil.

Table 4.1 Comparison of the SNR and the IU with our single-channel solenoid coil, dual-channel breast coil, and Philips SENSE 4-channel breast coil. *The relative SNR is calculated from the ratio between a given breast coil over Philips SENSE 4-channel breast coil.

	Our single-channel breast coil / (relative SNR)*	Our dual-channel breast coil/ (relative SNR)*	Philips SENSE 4-channel breast coil/(relative SNR)*
Signal-to-noise ratio (SNR)			
at flip angle 30°	90/(0.80)	134/(1.20)	112/(1.00)
at flip angle 90°	112/(0.80)	156/(1.11)	140/(1.00)
Integral Uniformity (IU)			
Coronal plane	0.16	0.27	0.28
Transvers plane	0.03	0.21	0.15

4.4. Discussion

We have demonstrated a new unilateral dual-channel breast coil for our multimodal MR/PEM cancer therapy monitoring application. The highest SNR among three different coils is achieved with our novel dual-channel breast coil. The primary reason for the high SNR of our dual-channel breast coil is attributed to the filling factor. Our dual-channel breast coil has the highest filling factor compared to our single-channel solenoid coil and Philips SENSE 4-channel coil. However, our single-channel solenoid coil shows the best IU from the MR images of the breast phantom. The main reason for worse IU of our dual-channel breast coil and Philips SENSE 4-channel coil is the dielectric effect of the breast phantom (diameter 12 cm). The phantom is too close to the conductive loop (diameter 15 cm) of coils such that the phantom dielectric effect contributed as a loss medium to the RF resonance loop. This image non-uniformity of our dual-channel breast coil and Philips SENSE 4-channel breast coil disappears with the smaller size breast phantom, which is more practical in clinical MR imaging setup. Regarding MR imaging speed, our dual-channel coil finishes the scanning of T1-weighted gradient-echo sequence at the same scanning time of Philips SENSE 4-channel breast coil.

Our dual-channel breast coil design and prototype MR/PEM interface are designed with the concept of the prone positioning of a patient. The shape of our dual-channel breast coil and the interface design of MR/PEM are formed with this configuration in mind. However, our design is only tested using the breast phantom. An in-vivo study is crucial for further validation of our approach that will be the subject of a future communication. Greater attention is required to the ergonomics of the coil design and the MR/PEM hardware interface design to proceed with in-vivo clinical pilot experiments. The coil should be designed to fit as comfortable as possible while maintaining its MR image quality with PEM detector heads and breast compression paddles.

Specifically, sharp edges must be removed to form smooth contours, particularly on physical contacts to breast tissue. All electric components must be covered and electrically insulated from the contact with the patient. Our dual-channel coil is designed for unilateral MR breast scanning, while Philips SENSE 4-channel breast coil is designed for bilateral MR breast imaging. Our dual-channel coil should be extended to bilateral MR breast scanning by simply replicate the coil configuration on the other side.

4.5. Conclusion

In this chapter, a new dual-channel breast coil design for our MR/PEM cancer therapy monitoring application is proposed. The MRI experiments have demonstrated that our dual-channel breast coil can provide comparable MR image SNR and IU to Philips SENSE 4-channel breast coil with similar scanning speed. This validation experiment justifies further investigation and modification of our design concept. We plan to perform imaging on human subjects after receiving appropriate institutional approvals.

Chapter 5: Development of excitation-resolved NIRF system

5.1. Introduction

Optical fluorescence imaging has attracted significant attention due to non-ionizing radiation, cost-efficiency, and high-sensitivity. Fluorescence imaging utilizes a wide-field illumination source and image detectors such as a charge-coupled (CCD) camera to measure fluorescence signal, which has proven to be suitable source-detector geometry for intraoperative optical imaging. (62) Fluorescence imaging can be even more powerful when utilizing near-infrared excitation source to minimize intrinsic tissue fluorescence and to enhance tissue penetration depth of light because the absorption of the main tissue chromophores, such as hemoglobin, lipid, and water is minimal around 800 nm. Most of the viable NIR fluorescence imaging agents have an absorption or excitation maximum around 750 – 800 nm. For instance, ICG has seven times higher absorption at 800 nm than the absorption at 690 nm, which is a frequently used far-red wavelength. In other words, one must use seven times brighter light source to achieve the same fluence rate of ICG fluorescence with a far-red light source, which also results in increased background tissue fluorescence. It is no wonder that near-infrared fluorescence imaging (NIRF) can be a promising molecular-guided surgery tool for better identification of deeply seated fluorophores.

NIRF is a rapidly growing noninvasive and nonionizing molecular two-dimensional projection imaging technique that can generate high-resolution, high-sensitivity, and high-contrast images for preclinical (145) and clinical applications (146). Even though a large pool of near-infrared NIR fluorescence agents is under development, the only one approved by the U.S Food and Drug Administration (FDA) for human intravenous injection in the last 50-years is ICG.

Owing to its excellent biocompatibility, ICG has been used for a variety of biomedical applications such as intraoperative sentinel lymph node mapping in breast cancer (147), ovarian cancer detection (148), hepatic function (149) and cardiac output (98) estimations, choroidal angiography (150), photodynamic therapy (151), treatment of leg veins (152), and inflamed atherosclerotic plaques (38). The maximum excitation wavelength of ICG (780 nm in aqueous media, 800 nm when bound to plasma proteins) lies in the near-infrared 'imaging window' in which the low tissue absorption and scattering allow a deeper probing depth. Furthermore, the background autofluorescence is minimized at excitation wavelengths longer than 780 nm (153). The principle of NIRF with ICG is based on tissue illumination with excitation light sources, such as light-emitting diodes (LED) and laser diodes (LD), and the detection of the fluorescence emission intensity at the surface with a charge-coupled device (CCD) camera incorporated with optical interference filters.

ICG is an amphiphilic cyanine dye whose excitation spectrum depends on the nature of the solvent and the concentration of ICG (35). The main peak of the excitation spectrum of ICG shifts from 780 nm to 800 nm when free ICG binds to plasma proteins. Following intravenous injection, the competition between the binding to protein and the aggregation determines the *in-vivo* spectral properties of ICG (154). Some researchers have reported that a gradual spectral peak blue shift of 9 nm after intravenous injection due to specific phospholipid binding (155). Furthermore, ICG can be incorporated into the design of an activatable tumor imaging agent, whose spectral properties are different before and after activation (156). Therefore, spectral investigation, in addition to the fluorescence intensity-based imaging, can help better understand the Pharmacokinetics of ICG and its associated biological processes *in-vivo*. Most importantly, the spectral investigation can improve the image contrast of NIRF.

The measurement of the excitation-shift of ICG in turbid media with a wide-field imaging geometry, unfortunately, has been challenging for the many reasons. Firstly, the Stokes shift of ICG is too small to separate the heavily overlapping excitation and emission spectra. Secondly, the solvatochromic response of ICG is too weak to be detected by a conventional NIRF system. Finally, the tissue optical properties aggravate both excitation and fluorescence spectra via multiple scattering. For these reasons, a suitable excitation-resolved source is necessary. Several techniques can be used for spectrally-resolved NIRF systems using a liquid crystal tunable filter (78) and a spectrograph (157) to acquire accurate spectral information of ICG with a wide-field imaging setup. However, these techniques are all employed at the detection side and have an intrinsic trade- off between the spectral resolution and the photon flux.

Instead of scanning the emission spectrum, excitation spectrum-resolved NIRF could be a more suitable spectroscopic approach for fluorescence-guide surgery. Since the excitation fluorescence spectroscopy reports wavelength-dependent excitation spectra of fluorescent molecules, it is not necessary to discard any fluorescence emission light for the spectroscopic purpose. Therefore, the excitation spectrum-resolved NIRF could use most of the fluorescence emission photons without sacrificing the spectral resolution. There are several reported spectrally-resolved light sources such as filtered broadband source, LEDs, and LDs. (7) Filtered broadband sources are a widely used technique to obtain excitation-resolved spectroscopic information of ICG with various source-detector geometries. (8) However, this wavelength-selection method with post-filtering suffers a tradeoff between the spectral confinement and the illumination brightness. LEDs can be a high brightness source but have a broad emission spectrum that is unsuitable for resolving the minute solvatochromic response of ICG. LDs can be a promising candidate because they meet the spectral confinement requirements, as well as having high brightness. However, LDs

are not suitable for in-vivo imaging applications that require sufficient video frame-rates, such as a fluorescence-guided surgery.

Wavelength-swept lasers are rapidly growing light source technology in the medical optics field, for use in optical coherence tomography, and its extent of biomedical imaging applications are gradually increasing. (81, 158-162) Due to its unique performance of emitting almost monochromatic light with broadband wavelength-swept bandwidth, wavelength-swept lasers in the near-infrared spectral window can make a versatile light source for the excitation-resolved NIRF.

In this chapter, we propose a novel method that can obtain spectrally resolved images in NIRF by employing a near-infrared wavelength-swept laser, as opposed to the previous techniques which employ spectral resolving on the detection side of the instrumentation. To the best of our knowledge, we demonstrate for the first time the spectrally-resolved NIRF imaging with a wavelength-swept laser and a CCD camera. Since the quantum yield of the fluorescence is independent of the excitation wavelength (163), the fluorescence intensity is proportional to the quantum yield, the concentration of fluorophore, and absorbed energy during the excitation. Accordingly, the measurement of the fluorescence intensity differences while sweeping the laser wavelength can provide information on the wavelength-dependent excitation of the fluorophores.

Several research groups have reported on various types of near-infrared wavelength-swept lasers for biomedical imaging (82, 84, 161). Meanwhile, we recently developed a wavelength-swept laser centered at 800 nm to image microstructural and functional information of blood *in-vitro* (85) and high-resolution depth-resolved retina layers (164) for optical coherence tomography. The wavelength-swept laser that we have developed can tune the wavelength from 780 nm to 820 nm, which covers the maximum excitation wavelength of ICG.

5.2. Methods

5.2.1. Near-infrared wavelength-swept laser

Since a piezoelectric transducer based wavelength-selector poses thermal instability, we employed a holographic transmission grating and a Galvo-scanner as a wavelength selector to avoid the heat instability [Figure 5.1]. A traveling-wave semiconductor optical amplifier (SOA) was employed to provide the optical gain fro the spectral range of 780 nm to 820 nm. A 10-dB fiber-optic directional coupler is connected to the output port of the SOA. A 90 % arm of the optical directional coupler is used to drain the laser output while the other arm coupled to the external fiber-optic laser cavity to feedback stimulated light towards the traveling-wave SOA. The wavelength-selector consists of a holographic transmission grating, a reflection mirror, and a Galvo-scanner mirror. The wavelength selection is made by rotation of the Galvo-scanner mirror such that a narrow- bandwidth of the light within the numerical aperture of a fiber-optic collimator can act as a feedback to the external laser cavity. The measured maximum output power and the steady-state -3 dB laser linewidth are 14 mW and 0.2 nm, respectively at 801 nm. To reduce the spectral tails of the spontaneous emission overlapping the passband of the interference filter, we place an interference bandpass filter at the output port of the wavelength-swept laser, which is centered at 800 nm and the bandwidth of the passband was 40 nm. To maximize the out-band rejection performance of the interference filter, we collimate the laser light with a fiber-optic collimator and let the collimated light pass through the filter with an incident angle of 4 degrees.

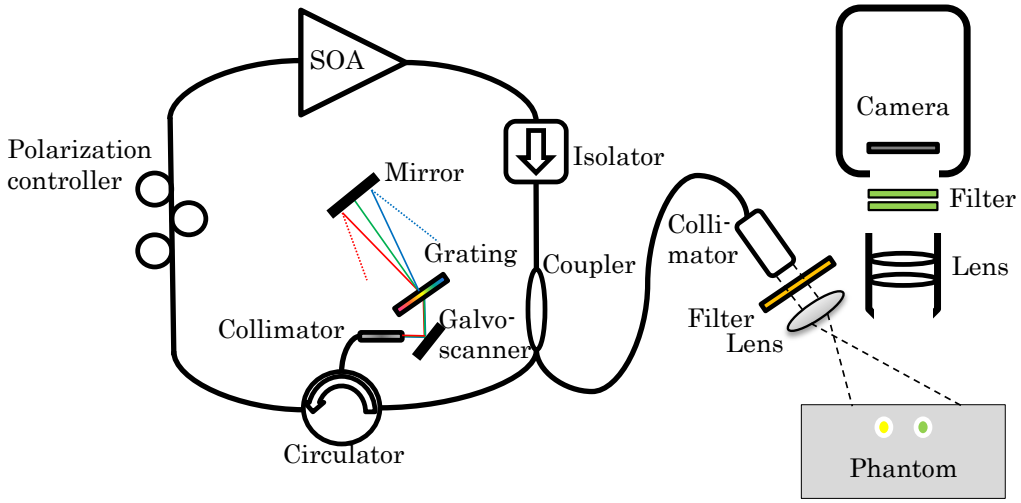

Figure 5.1 Schematic of the wavelength-swept laser (left) and epi-illumination setup for NIRF imaging (right). SOA stands for semiconductor optical amplifier.

A lens expanded the filtered laser beam before illuminating the phantom. The measured intensity of the wavelength-swept laser around 800 nm was 10 mW after the spectral filtering.

5.2.2. Wide-field imaging system

A schematic of the system implementing a wide-field epi-illumination geometry is shown in Figure 5.1. The diameter of the illumination spot on the target was 40 mm. A cooled CCD camera with a Sigma MACRO 50 mm F2.8 lens was used to collect photons emitted from the surface. We employed two-cascaded bandpass interference filters with a passband of 10 nm, centered at 830 nm to selectively collect the fluorescence emission of ICG [Figure 5.2]. The filters are located between the lens and the cooled CCD camera. The steady-state spectra of the laser at different wavelengths before the optical filtering are shown in Figure 5.2(a). We collected the light intensity of the laser power with and without the optical interference filters on the CCD camera and calibrated the measurements by referring to the used integration time and the gain of CCD camera. One can notice that the spectral tails at the longer wavelengths decreased the out-band rejection

performance of the cascaded bandpass filters. Images of different laser wavelengths are collected with the fluorescence filters. This process improves the accuracy of the fluorescence imaging to calibrate the NIRF system for the wavelength dependent excitation leakage. (165)

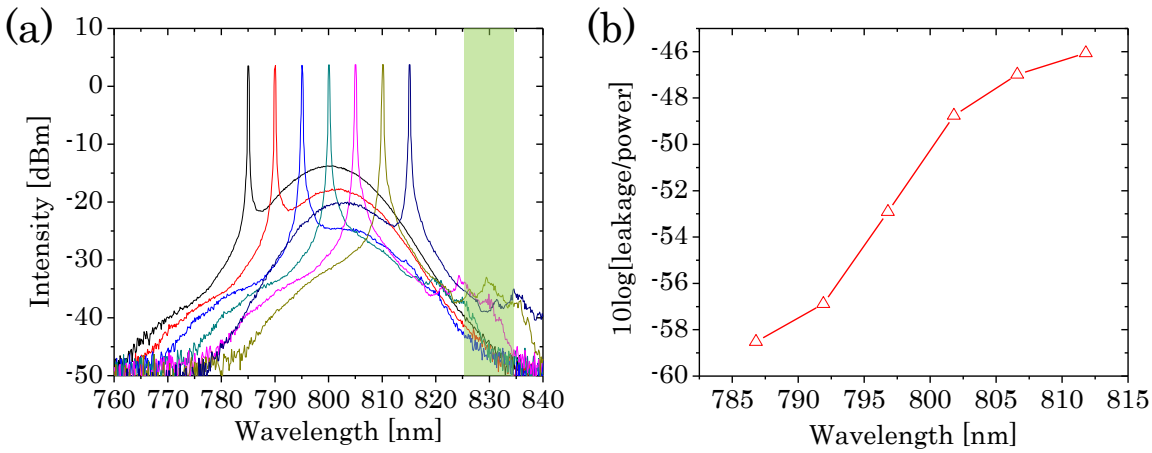

Figure 5.2 (a) Graph of laser output spectra of the wavelength-swept laser. The passband of the interference filters for fluorescence collection is indicated by a shaded box in green. (b) A graph of the excitation light leakage intensity versus wavelength.

5.2.3. Image processing

The excitation leakage intensity consists of the excitation leakage depending on the spectral tails of the excitation laser, the interference filter performance of rejection, and design of the optical lens system. (165) The measured fluorescence intensity, FL, at the surface can be described as in Equation (5.1)

$$FL(\lambda_n) = \frac{1}{S(\lambda_n)}\{I(\lambda_n) - L(\lambda_n)\} + \varepsilon \qquad (5.1)$$

where, S is the power spectrum density of the wavelength-swept laser, λ_n is the nth wavelength of a selected set of wavelengths. I is the raw intensity, L is the excitation leakage. ε is the system noise including the shot noise and the readout noise. To quantify the spectral information, we calculated the spectrum centroid as described in Equation (5.2)

$$SC = \sum_{n=0}^{N-1} \lambda_n FL(\lambda_n) \Big/ \sum_{n=0}^{N-1} FL(\lambda_n) \qquad (5.2)$$

where, SC is the spectrum centroid, λ_n is the wavelength of the index n. N is the number of used wavelengths.

5.2.4. Turbid phantom

Two sets of agarose phantoms are used to examine the performance of the excitation-resolved NIRF system. The first phantom consists of an agarose gel with Intralipid and Indian ink mimicking general optical tissue properties of tissue with the absorption and scattering coefficient of 0.008 mm^{-1} and 0.8 mm^{-1}, respectively. A plastic box is used to form the shape of the agarose phantom. A glass tube (diameter: 5 mm, wall thickness: 0.3 mm, length: 120 mm) is embedded 10 mm below the surface. The glass tube contains ICG dissolved in dimethyl sulfoxide (DMSO) at a concentration of 5 μM. Dimethyl sulfoxide (DMSO) is a widely used amphipathic solvent for

experimental hydrophobic drug delivery studies and is an effective medicine for various diseases such as inflammation and arthritis. (166, 167) Particularly, imaging DMSO is of interest in studying water-insoluble drug delivery of biological barriers such as the skin, the membrane, the blood-brain barrier. (168) Therefore, development of an in-vivo organ-level molecular imaging technique to visualize DMSO is essential for better understanding of the physicochemical interaction of the molecule in tissue. The maximum absorption of the ICG in DMSO is found to be 796 nm with a commercial spectrometer (USB 2000+, Oceanoptics Inc., USA). The NIRF images were collected using a set of six wavelengths (N = 6) of the wavelength-swept laser from 789 nm to 814 nm, at 5 nm interval. A set of six images at different wavelengths is collected, with each image consisting of 2280 × 1528 CCD elements with a 16-bit resolution. The images are collected as 570 × 382 pixels, with 4 × 4 CCD elements binning. The integration time of the CCD camera is nine second per each wavelength. The sum of the fluorescence intensity images of the six images is shown in Figure 5.3(a). The field of view of the images is 70 mm × 47 mm. We calculated the spectrum centroid; then we plotted the calculated values at a selected yellow dashed line as shown in Figure 5.3(b). The deviation of the calculated spectrum centroid values increases while the sum of fluorescence intensity decreases. The spectrum centroid and full-width-half-maximum are 796.67 nm and 0.49 nm, respectively.

The second phantom consisted of the same agarose gel, but with two different ICG tubes. One is a tube containing ICG dissolved in distilled water, and the other is a similar sized tube with bovine serum albumin (400 mg/ml, Sigma-Aldrich). The two ICG tubes were separated 10 mm away from the center line of the agarose phantom. The concentration of ICG in both tubes was 5 μM. The absorption maximum of ICG in water was found at 780 nm, while the absorption maximum of ICG bonded to bovine serum albumin is obtained at 800 nm.

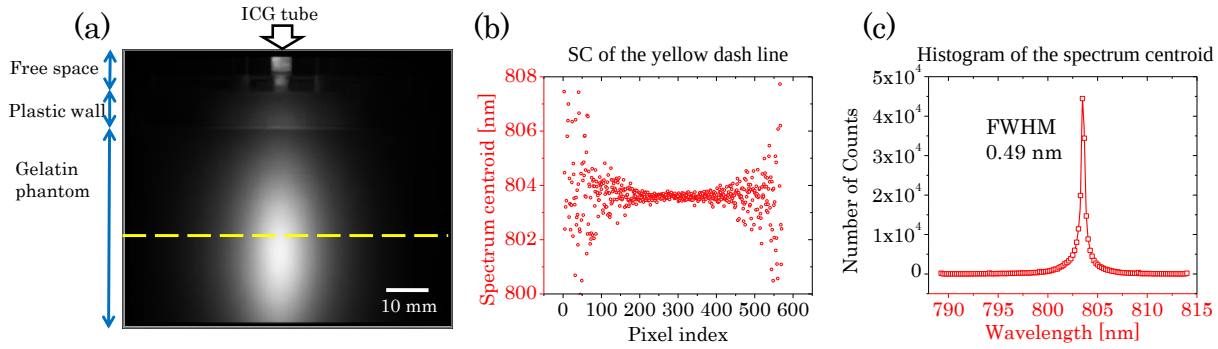

Figure 5.3 (a) Fluorescence intensity image of an agarose phantom with a 5-mm diameter tube containing ICG dissolved in dimethyl sulfoxide (DMSO). (b) Graph of the spectrum centroid along the yellow dash line on the image (a). Graph of the histogram of the spectrum centroid in the full field-of-view.

5.3. Results

The two different ICG tubes are visualized using the sum of fluorescence intensity measurements [Figure 5.4(a)]. The intensity difference is originated from the center wavelength of the interference filter passband (830 nm). As expected, the spectrum centroid of the ICG bonded to bovine serum albumin shows a higher value than the value of the ICG in water. The histogram of the spectrum centroid is shown in Figure 5.4(c). The maximum pixel count frequency of the spectrum centroid histogram is found at 801.92 nm for the free ICG in water, and 803.29 nm for the ICG bonded to bovine serum albumin. One can notice that there is negative skewness of the histograms on Figure 5.3(c). The wavelength-dependent absorption of the phantom is responsible for the negative skewness on the spectrum centroid explains the red-shift by the phantom absorption. This result shows good agreement with a previous publication. (150, 169, 170) As the fluorescence emission on the surface is going away from the ICG tubes, the spectrum centroid is gradually shifting [Figure 5.4(b)].

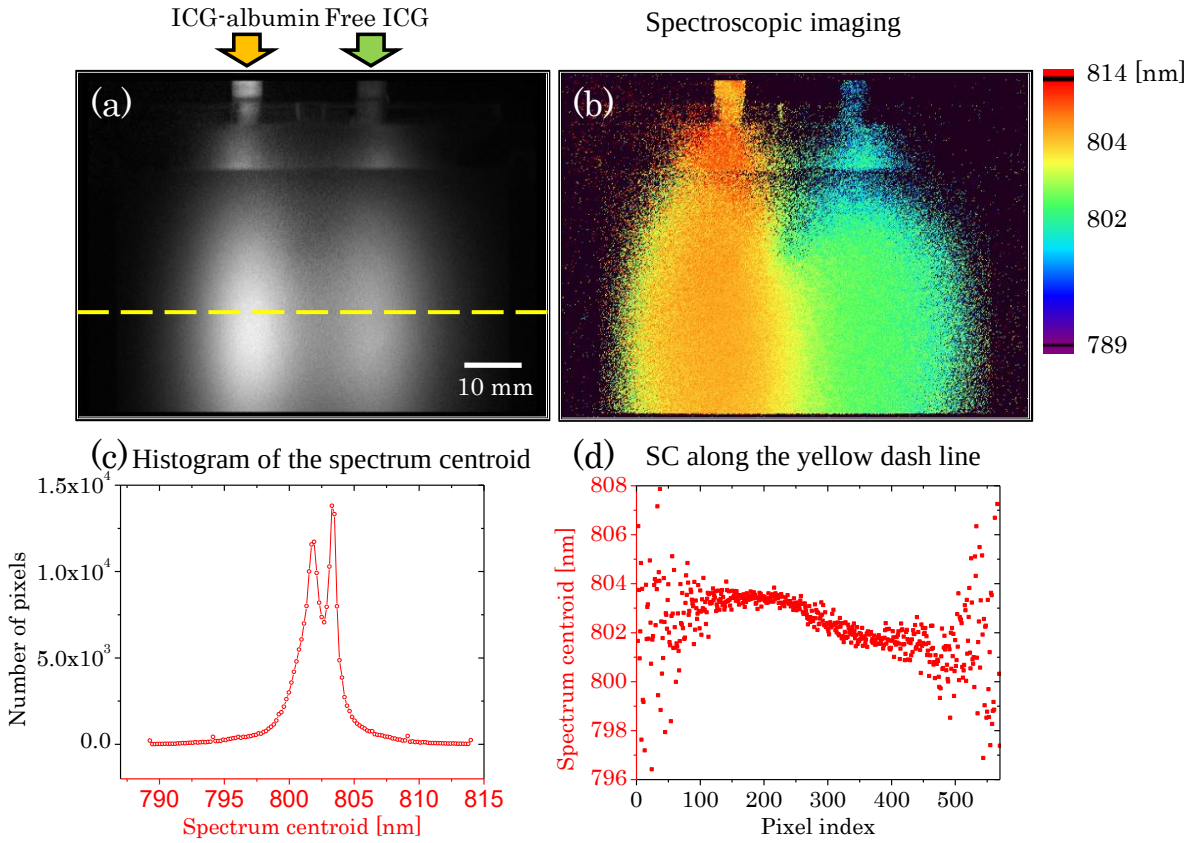

Figure 5.4 (a) Fluorescence intensity image of an agarose phantom with two different tubes. One tube was filled with ICG-albumin in distilled water (left side of the image), while the other tube is filled with free ICG in distilled water (right side of the image). (b) Spectrally decomposed fluorescence image with the spectrum centroid. Pixels dominated by noise are eliminated by setting a threshold value that is larger than zero. (c) Histogram of the calculated spectrum centroid of the whole image. (d) Graph of the spectrum centroid along the yellow dash line on the image.

5.4. Conclusion

We demonstrated that the excitation-resolved NIRF imaging with ICG using wavelength-swept laser. The performance of the excitation leakage rejection versus the wavelength of the swept laser is evaluated. The spectral resolution of the excitation-resolved NIRF system is characterized by the FWHM of the spectrum centroid histogram. The spectral components of two different ICG tubes located 10 mm deep from the phantom surface are successfully decomposed by using the spectrum centroid. This technique is not limited to differentiation of ICG states. The wavelength-swept laser-based excitation-resolved NIRF can also be a promising method for multiple near-infrared agents imaging and activatable agents for specific biomolecule targeting. This technique still poses practical limitations. A trade-off between the imaging speed and the improved statistics for the estimation of the spectrum parameters, however, can be resolved by employing high-gain and high-speed CCD cameras, such as intensified CCD and electron-multiplying CCD for the real-time excitation-resolved fluorescence imaging. The excitation leakage of the wavelength-swept laser at longer wavelengths can be reduced by proper design of optical gain medium, lens, and interference filters.

Chapter 6: Ratiometric Excitation-resolved NIRF towards quantitative measurement of microenvironmental solvent polarity

6.1. Introduction

Predicting solubility and permeability of drug *in vivo* is essential for drug discovery and development. (171-173) Dimethyl sulfoxide (DMSO) is a water miscible solvent that is frequently used to enhance solubility and permeability of water-insoluble pharmaceutical compounds by diluting them into a well-stirred aqueous medium for the drug administration. (168) However, the solubility of the DMSO-mixed water-insoluble drugs depends on in a different local residual level of DMSO, and permeability of the drugs decreases by precipitation of the drugs in biological media. Imaging DMSO distribution *in vivo* can provide localized levels of residual DMSO, and thus help better understanding the pharmacokinetics of the water-insoluble drugs. Saar *et al*. have demonstrated molecular imaging visualizing DMSO with a stimulated Raman scattering technique. (174) However, this nonlinear microscopy is inadequate for wide-field imaging with an organ-level field of view. Meanwhile, measuring the environment polarity in biological media has been studied extensively with optical fluorescent dyes using solvatochromism. (149, 175) Indeed, optical dyes are utilized for this purpose since their molecular spectral profiles are significantly affected by the local polarity of biological media. These compounds whose absorption and emission spectra depend on the environment polarity are known as solvatochromic dyes, which can perform in a wide range of the optical spectrum including ultraviolet, visible, and near-infrared (NIR, ~650-950 nm). However, it is challenging to perform solvatochromic dye-mediated polarity measurements *in vivo*. The solvatochromic dyes in NIR, unfortunately, have heavily overlapping excitation and emission spectra and exhibit weak

solvatochromic shifts in their spectral profiles. Moreover, tissue optical properties affect the measured fluorescence spectra. (150, 170)

Among the various solvatochromic dyes, Indocyanine green (ICG) is the most widely used NIR dye for fluorescence imaging. (176) Its absorption peak lies around 800 nm where biological tissue attenuates the fluorescence less and generates low autofluorescence. (153) Furthermore, hemoglobin absorption stays low and has an isosbestic point at 800 nm. Despite these spectroscopic merits of ICG in the 800-nm spectral window, the use of ICG has been limited to visualize blood perfusion volume and tissue permeability rate-based physiological assessment due to the lack of molecular specificity. The solvatochromic response of ICG can also be leveraged to measure the polarity of the local environment. Typically, ICG is dissolved into an aqueous solution before the ICG administration, which has its absorption peak at 780 nm. After the administration, ICG quickly and mostly binds to hydrophobic pockets of albumin and its absorption peak shifts to 805 nm. (177) Figure 6.1(a) shows the normalized absorption spectra of ICG in water, DMSO, and bonded to bovine serum albumin (BSA-ICG). Figure 6.1(b) demonstrates a complex behavior of ICG in mixtures of water, DMSO, and BSA, which mimics ICG in biological media such as lymph or blood in the presence of DMSO. First, ICG is mixed with bovine serum albumin (BSA, Sigma-Aldrich, USA) at a concentration of 50 mg/ml to mimic the concentration of albumin in human plasma dissolved in distilled water. (178)

This mixture is called BSA-ICG. After adding DMSO into the BSA-ICG in distilled water, one can observe that the varying amount of DMSO results in the absorption peak shift of ICG. At the volume fraction zero, the solution contains BSA, ICG, and water. The absorption peak of this solution is demonstrating that most of the ICG are bound to BSA. The BSA-ICG bond gradually breaks until the volume fraction of 0.4, the solutions in this volume fraction range contain BSA-ICG, free-ICG, BSA, water, and DMSO. One can observe that the absorption peak shifts to the shorter wavelength since free-ICG starts

attributing to this absorption blue-shift. Between the volume fraction of 0.4 and 1, all ICG becomes free from the BSA-ICG bond and its absorption spectrum solely depends on the polarity of the mixtures of solvents.

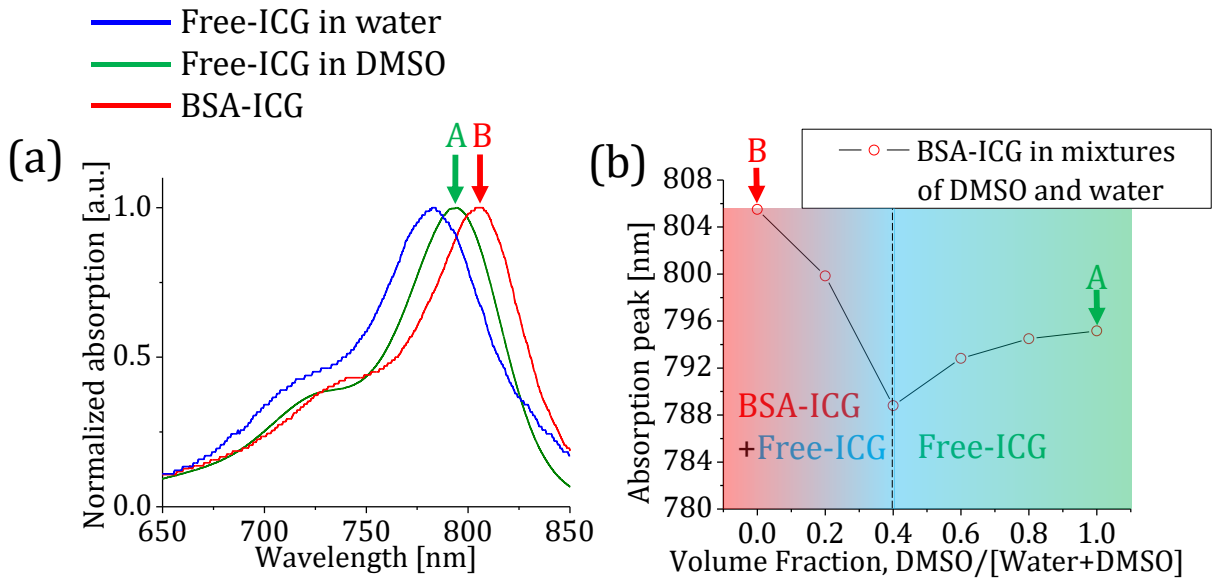

Figure 6.1 (a) Absorption spectra graph of ICG in different environments. The absorption peaks of BSA-ICG, ICG in DMSO and ICG in water are 805 nm, 795 nm, and 780 nm, respectively. (b) The graph shows the absorption peak shift of a 6 μM BSA-ICG solutions adding DMSO.

To be able to measure this complex solvatochromic response of ICG, a fluorescence lifetime imaging technique has been introduced. (175) However, this fluorescence lifetime technique requires either pulsed laser or radio-frequency amplitude modulated source. Also, expensive high-speed electronics are necessary to measure the time-domain or the frequency-domain signals. In this Letter, we demonstrate a steady-state spectroscopic wide-field imaging technique that can resolve the solvatochromic response of ICG. The pivotal part of our imaging technique is a continuous-wave near-infrared novel wavelength-swept laser, which can tune its output wavelength with high speed and superior spectral resolution. (85)

6.2. Methods

6.2.1. Experimental setup

The wavelength swept window of the laser is optimized around 800 nm to excite ICG around its maximum absorption wavelength as shown in Figure 6.2(a). An optical spectrum analyzer measures the different laser output spectrum. The selected spectra of the laser output are displayed in dBm, Figure 6.2(b). An exciter bandpass filter with a central wavelength of 794 nm, a bandwidth of 32 nm, and an out of band optical density (OD) of 7 is employed to clean up non-lasing components. An optical diffuser homogenizes the Gaussian laser beam with a power of less than 0.5 mW/cm2. A CCD camera (ColdBlue, PerkinElmer Optoelectronics, USA) with an imaging lens (Marco F/2.8, Sigma Inc., USA) is used to capture snapshots of fluorescence signals. The working distance of the imaging lens is 60 cm. An emitter bandpass filter that has a central wavelength of 840 nm, a bandwidth of 10 nm, and an average OD of 5 is used to collect the fluorescence emission. Figure 6.2(c) shows the measured OD of the filters employed in this HER-NIRF system in the absence of ICG. As the wavelength of our swept laser approaches the fluorescence collection band, the excitation light leakage degrades the performance of our system reducing the signal-to-noise ratio and yields to incorrect fluorescence measurements. (165) Therefore, HER-NIRF images need to be corrected by subtracting the excitation-leakage images collected in the absence of ICG.

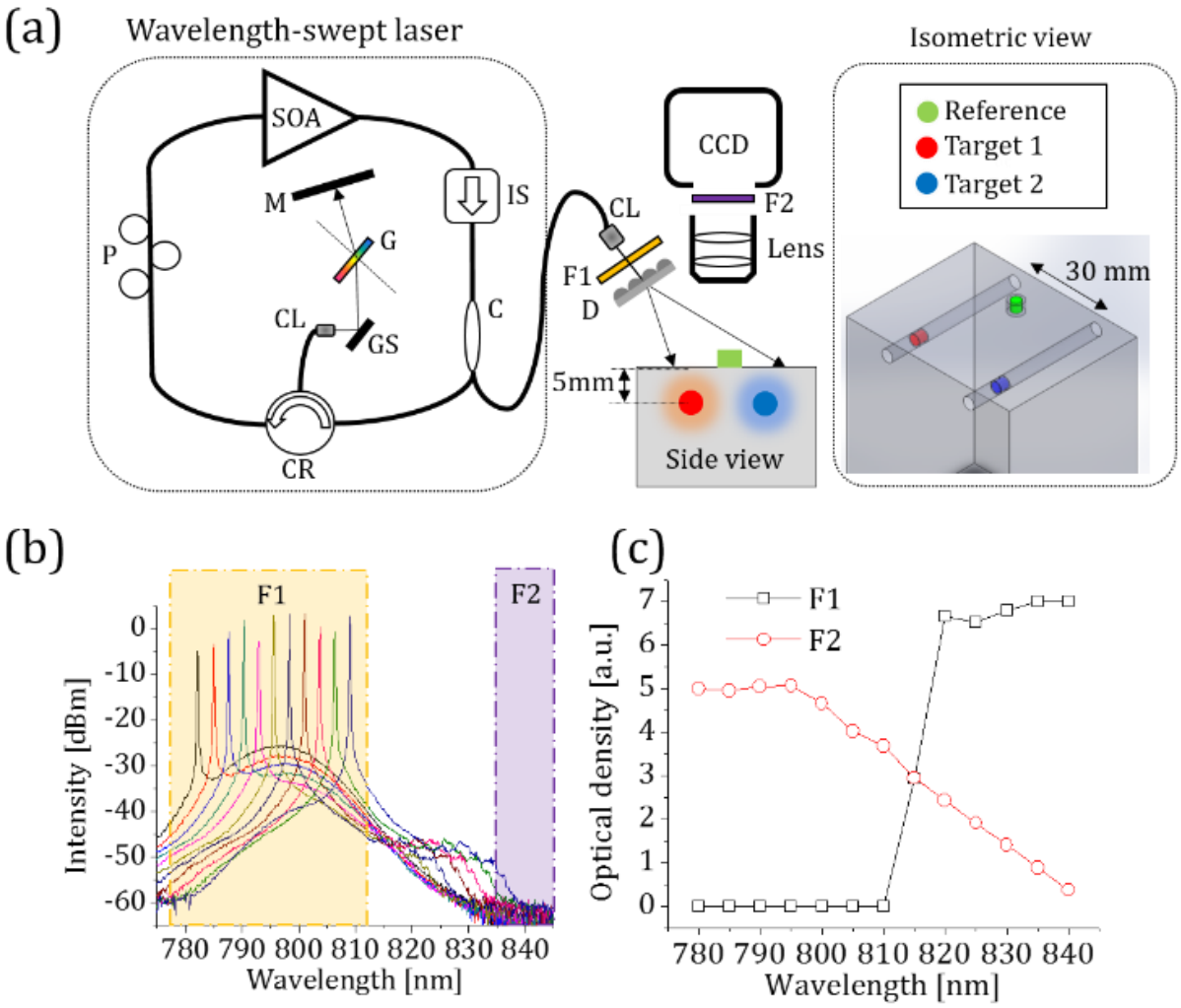

Figure 6.2 (a) Schematic diagram of the wavelength-swept laser and our HER-NIRF system. SOA: semiconductor optical amplifier, P: polarization controller, CR: circulator, CL: collimator, GS: Galvo-scanner, G: grating, M: mirror, C: coupler, IS: isolator, F1: exciter bandpass filter, D: diffuser, F2: emitter bandpass filter, CCD: charge coupled camera. (b) Measured output spectra of our wavelength-swept laser at different wavelengths. (c) Graph of the optical density of F1 and F2 over the wavelength range of interest.

6.2.2. Ratiometric excitation spectrum measurement

A ratiometric approach is employed to estimate a relative excitation shift on a reference standard that can be either a well-known fluorescent dye or a priori fluoresce image data to measure the solvatochromic response of ICG. By using the first-order approximation to the basic equation of fluorescence can be written as

$$F(\lambda) \approx I\eta \frac{\Omega}{4\pi} 2.303\varepsilon(\lambda)lc. \qquad (6.1)$$

where, F is the steady-state fluorescence intensity, I is the incident light excitation intensity on the target, Ω is the solid angle, ε is the molar extinction coefficient as a function of the excitation wavelength λ, η is the quantum yield, l is the path length of excitation light through the fluorescence sample, and c is the concentration of the fluorescent dye.

The change of the molecular environment affects the wavelength-dependent molecular extinction coefficient, and thus the spectral scan driven by our system reveals the solvatochromic shift. One can assume a simplified case where the change of ICG concentration is trivial between the time sets of before and after the administration of DMSO. The ratiometric fluorescence of ICG in DMSO on BSA-ICG in a dilute solution can be written as

$$\ln\left[F_D(\lambda)/F_B(\lambda)\right] = \ln\left[\varepsilon_D(\lambda)/\varepsilon_B(\lambda)\right] + \ln\left[\eta_D/\eta_B\right]. \qquad (6.2)$$

where, the subscripts B and D describe BSA-ICG and ICG in DMSO, respectively. The right-hand side of Equation (6.2) consists of a wavelength-dependent ratio of the extinction coefficients and a ratio of the quantum yields.

To confirm Equation (6.2), control measurements of absorption spectra of different ICG solutions are performed on a variety of ICG solutions (Arkon, Inc., USA) with a molar concentration of 6 μM. The first kind is mixed with bovine serum albumin with a concentration of 50 mg/ml to mimic the concentration

of albumin in human plasma dissolved in distilled water, BSA-ICG. In the second kind named "DMSO-ICG," ICG is dissolved in 99.9 % DMSO (DMSO, Fisher, USA) to engage the solvatochromic response of the ICG. Also, different mixtures of BSA-ICG in various DMSO and water volume fractions are prepared. The absorption spectra of the ICG solutions are measured by a commercial spectrometer (USB2000, Ocean Optics Inc., USA). The ratio of extinction coefficients of DMSO- and BSA-ICG in water solutions is shown in Figure 6.3(a). Between 785 nm and 810 nm, the natural logarithmic ratio of extinction coefficients shows the maximum contrast and almost a linear decrease as a function of wavelength. In addition, the isosbestic point of DMSO- and BSA-ICG is found in the spectral range. Hence, we can model the ratio of extinction coefficients as a linear function of the excitation wavelength,

$$\ln\left[\varepsilon_D(\lambda)/\varepsilon_B(\lambda)\right] \approx m_{solvato}(\lambda - \lambda_{iso}). \qquad (6.3)$$

where, $m_{solvato}$ is the slope of our linear approximation and λ_{iso} is the isosbestic wavelength of DMSO- and BSA-ICG in water solutions. In the maximum contrast window, the ratio of extinction coefficients in the different volume fractions are presented in Figure 6.3(b). Calculated values of $m_{solvato}$ the various volume fractions are plotted as a function of the volume fraction of Figure 6.3(c). One can compare Figure 6.1(b) with Figure 6.1(c) to find a good correlation between our commercial spectrometer absorption measurements and the slope values of our linear model in Equation (6.3) as shown in Figure 6.3(d). Note that a 1 nm increase in the absorption peak of ICG corresponds to 1.45×10^{-3} nm^{-1} of the slope change in our ratiometric model.

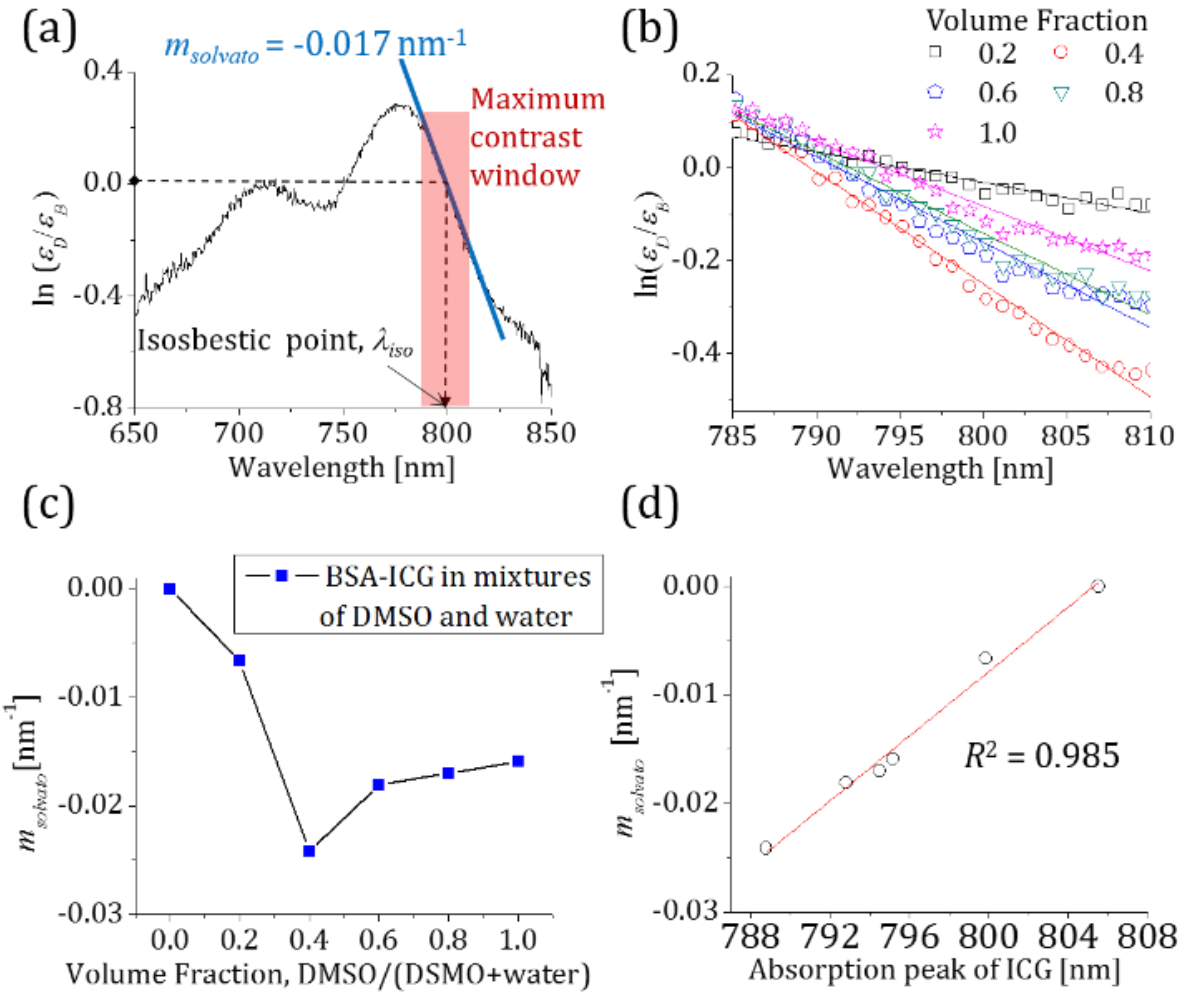

Figure 6.3 (a) Natural logarithmic ratio of the extinction coefficients of DMSO-ICG and BSA-ICG. The solid blue line shows a linear fit to the natural logarithmic ratio between 785 nm and 810 nm [red-boxed area]. (b) The graph shows the slope change of a 6 μM BSA-ICG solutions adding DMSO.

6.2.3. Tissue-like phantom

To conduct tissue-like turbid medium (μ_a= 0.0132 mm^{-1}, μ_s' = 1 mm^{-1} at 800 nm) experiments, an Intralipid gelatin phantom, L 70 mm × W 50 mm × D 100 mm, is prepared. Two 3.2 mm long tubes, with a 3.2 mm inner diameter, are placed 5 mm deep under the top surface of the phantom and positioned 30 mm apart, Figure 6.1(a). The tubes are filled with 26 μl of BSA-ICG and DMSO-ICG solutions.

The first step of our fluorescence experiments is measuring the ratiometric fluorescence in free space for the verification of Equation (6.2). Fluorescence images at 50 different excitation wavelengths are acquired with a wavelength step of 0.5 nm, Figure.6.4(a). The mean fluorescence signals are extracted from regions of interest and used for computation of the ratiometri**c** fluorescence. By incorporating Equation. (6.3) into Equation (6.2), we obtain

$$\ln\left[\varepsilon_D(\lambda)/\varepsilon_B(\lambda)\right] + \ln\left[\eta_D/\eta_B\right] = m_{solvato}\left(\lambda - \lambda_{iso}\right) + b_{quantum}. \qquad (6.4)$$

where, $b_{quantum}$ is the wavelength independent value of the relative quantum yield ratio. As seen from the black dots and line in Figure 6.4 (c), $b_{quantum}$ can be read at the isosbestic point and is 0.80, which means η_D is 2.23 times higher than η_B. The calculated $m_{solvato}$ obtained from the relative fluorescence measurement in Figure 6.4 (c) is -0.017 nm^{-1}, which shows good agreement with the calculated $m_{solvato}$ from our absorption measurements in Figure 6.3 (a). As expected, the slope value between two identical fluorescence signals of the BSA-ICG yields approximately zero as shown by the black dots and line in Figure 6.4 (b).

The second turbid phantom experiment is designed to demonstrate the DMSO-ICG identification performance of our HER-NIRF technique with the spectral distortion by multiple scattering. A BSA-ICG tube is used as a reference and placed on top of the phantom, Figure 6.1(a). As an experimental control, the

same BSA-ICG tube is positioned in the turbid phantom at a 5-mm depth. The other tube filled with DMSO-ICG is also put in the phantom at the same depth of the embedded BSA-ICG tube.

6.3. Results

Fluorescence images at different excitation wavelengths are acquired for this turbid phantom experiment. The CCD camera integration time is one second per image. The mean fluorescence signals are measured at the selected regions of interest indicated by the dashed-line circles in Figure 6.4(a). The ratiometric fluorescence for BSA- and DMSO-ICG tubes on the BSA-ICG reference is plotted as a function of the excitation wavelength as red and blue dots and lines in Figure 6.4(b) and Figure 6.4(c), respectively. The ratiometric fluorescence between the reference BSA-ICG on the surface and the BSA-ICG embedded in the phantom demonstrates a red-shift due to the multiple scattering which yields to a positive slope value in our ratiometric model, as shown in Figure 6.4(b). Likewise, the multiple scattering shifts measured the relative excitation spectrum of DMSO-ICG by increasing the slope value from -0.017 nm^{-1} (in free space) to -0.009 nm^{-1} (in phantom).

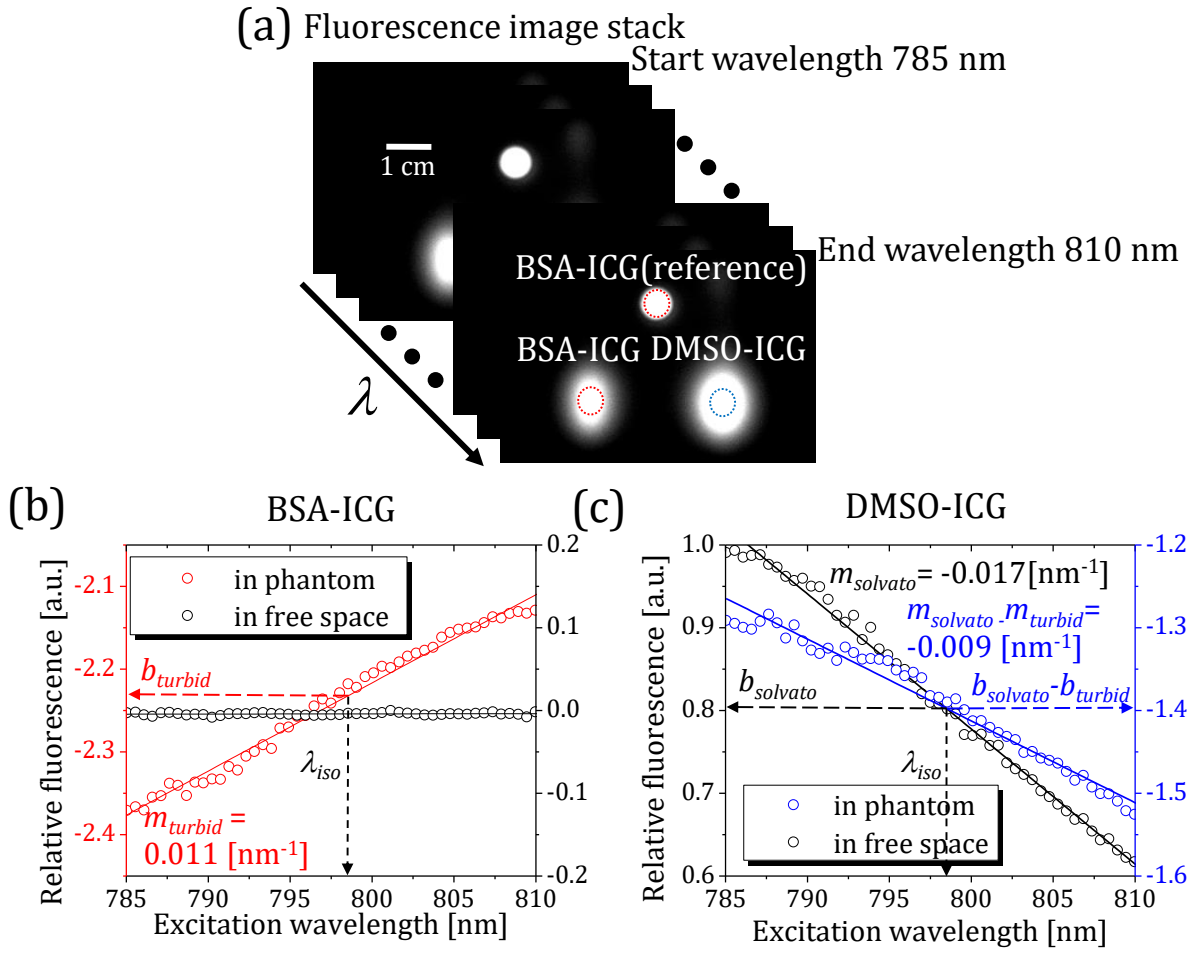

Figure 6.4 (a) Fluorescence image stack consists of 50 images obtained at different excitation wavelengths. Red-dashed circles indicate the reference BSA-ICG on the surface and the BSA-ICG embedded, in the phantom. A blue dashed circle shows the DMSO-ICG region of interest. (b) Ratiometric measurements of BSA-ICG in free space and phantom on the reference BSA-ICG. (c) Ratiometric measurements of DMSO-ICG in open space and phantom on the reference BSA-ICG.

A fluorescence signal from an embedded ICG tube in a turbid medium can be written as

$$A(F) = F\exp\left[-\mu_{eff}(\lambda)2d\right]. \qquad (6.5)$$

where, A is the attenuation operator describing the Beer's law, μ_{eff} is the wavelength-dependent effective attenuation coefficient, and d is the depth of the tube. Factor 2 describes the photon round-trip. If both the reference and the embedded targets contain the same BSA-ICG, we obtain

$$\ln\left[\frac{A(F_B)}{F_B}\right] = -\mu_{eff}(\lambda)2d = m_{turbid}(\lambda - \lambda_{iso}) + b_{turbid}. \qquad (6.6)$$

where, m_{turbid} is the slope of the linear fit in Figure 6.4(b) that is equal to 0.011 nm^{-1}. The parameter b_{turbid} is -2.23 which describes the wavelength-independent attenuation in the region of interest. If the embedded tube contains a different solution (DMSO-ICG) than the reference (BSA-ICG), we can use Equation. (6.2)-(6.6) to obtain

$$\ln\left[\frac{A(F_D)}{F_B}\right] = (m_{solvato} - m_{turbid})(\lambda - \lambda_{iso}) + (b_{quantum} - b_{turbid}). \qquad (6.7)$$

In Figure 6.4(c), $m_{solvato}$ corresponds to the slope of the black dots and line, while $(m_{solvato} - m_{turbid})$ corresponds to the slope the blue dots and line. The spectral distortion by multiple scattering affects the spectral content of DMSO-ICG measurements similarly to the result shown in Figure 6.4(b). Based on this theory and our experimental results, we further applied our ratiometric technique to

produce a pixel-by-pixel spectroscopic map. First, the fluorescence signal at each pixel is used as a numerator in the left-hand side of Equation (6.7), while the fluorescence signal of the reference BSA-ICG on the surface is used as the denominator. Afterward, the slope of the linear fit per pixel is attributed to the pixel under study to produce a spectroscopic image as shown in Figure 6.5(a). When the pixels show approximately a zero slope, they identify fluorescence signals from the reference BSA-ICG on the surface. However, when the pixels show a positive slope, they belong to the multiply scattered fluorescence signals from the embedded BSA-ICG tubes. Note that a positive slope is observed even around the container wall of the reference BSA-ICG due to scattering within the container wall. A gradient threshold of our linear fitting (-2.95×10^{-5} nm^{-1}) is applied on the spectral map to generate a binary identification map of DMSO-ICG. Despite this spectral content degradation induced by multiple scattering, one can still identify the pixels of DMSO-ICG tubes in Figure 6.5(b).

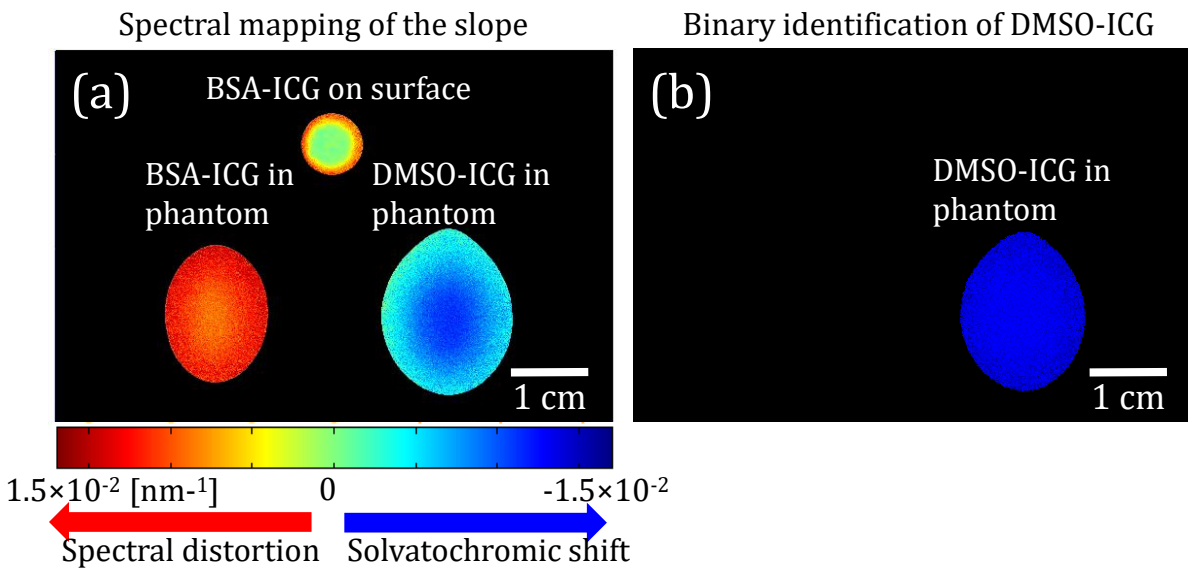

Figure 6.5 (a) Color-coded slope map shows the excitation blue-shift of the DMSO-ICG tube while the embedded BSA-ICG sample demonstrated a red-shift of excitation spectrum by multiple scattering. Low signal pixels from the intercept map are excluded from the image processing. (b) Binary identification map exclusively displays DMSO-ICG. All the pixels of the slope values that are lower than a gradient threshold is removed from the original spectral map.

6.4. Discussion and conclusion

We demonstrate the performance of our HER-NIRF technique as a proof-of-concept to measure the solvatochromic response of ICG in turbid phantoms. The spectroscopic measurement of the local polarity expands the information contents of conventional wide-field fluorescence imaging techniques. Although the sign of the slope is used to identify the presence of DMSO in each pixel qualitatively, our measurements show that quantitative imaging can be possible if one can choose appropriate reference signals to minimize the spectral distortion. As an alternative, if the HER-NIRF imaging is performed before and after the application of DMSO, the reference may not even be required considering the change in the slope of the ratiometric fluorescence. For example, if ICG is accumulated in lymph nodes and imaging is performed before and after the application of DMSO, the technique presented here can be applied since the depth of the reference and target will be the same in the Equation. (6.2). The ability to measure the distribution of DMSO *in vivo* can lead to a better understanding of the pharmacokinetic properties of ICG in tissue. For instance, K. Licha *et al*. have demonstrated that increasing hydrophilicity of cyanine dyes enhances the fluorescence image contrast of tumor by inhibiting the plasma protein binding of these dyes. Thus, the properties of DMSO inhibiting the albumin binding of ICG can lead to better understanding of the pharmacokinetics of ICG for tumor imaging. Furthermore, imaging of DMSO by measuring the excitation shift of ICG can be invaluable information for studying the pharmaceutical effect of DMSO on inflammation *in vivo*.

The wavelength-swept laser is the key to our HER-NIRF technique due to its superior performance compared to other available light sources. Being low-cost, fast in the spectral scan, and able to perform coherent light amplification, this wavelength-swept laser can be a very powerful light source for real-time measurement in various ICG imaging applications. While its superior spectral resolution is a significant advantage for this application, the HER-NIRF technique also provides a much higher signal to noise ratio

by measuring the whole fluorescence emission spectrum as opposed to conventional systems utilizing band-pass filters at the detection site. By providing additional spectral information, HER-NIRF technique can be applied for measuring the solvatochromic response of other fluorescence dyes and even be adapted for endoscopic applications due to the efficient light guiding by fiber optics. Our future aim is to apply this HER-NIRF technique for the imaging of ICG to map DMSO distribution *in vivo*.

Chapter 7: Conclusion and future work

7.1. Conclusion

In Part I, we have demonstrated a proof-of-concept of our MR/PEM cancer therapy monitoring strategy for clinically aggressive molecular subtypes of breast cancer. A serial dual-modal MR/PEM system is developed and validated with a tissue-like phantom study and a volunteer pilot study. A tissue-like phantom study shows that our PEM system has a 2-mm spatial resolution that is about 2.5 times better than a whole-body PET scanner. Our single-channel breast coil design with the breast compression paddle shows a comparable MR image quality to a commercial multi-channel breast coil from the pilot study with a volunteer.

Our novel design of the dual-modal imaging interface and fiducial markers allows a straightforward image registration of image data from breast MRI and PEM. Our new dual-channel breast coil design for our MR/PEM cancer therapy monitoring application is proposed. MRI experiments using a breast phantom have demonstrated that our dual-channel breast coil can provide comparable MR image SNR and IU to a commercial multi-channel breast coil as well as the MR scanning speed. This validation justifies further investigation and modification of our design concept to perform imaging on human subjects after receiving appropriate institutional approvals.

In Part II, we demonstrate that the excitation-resolved NIRF imaging with ICG using wavelength-swept laser. The performance of the excitation leakage rejection versus the wavelength of the swept laser is evaluated. The spectral resolution of the excitation-resolved NIRF system is characterized by the FWHM of the spectrum centroid histogram. The spectral components of two different ICG tubes located 10 mm deep from the phantom surface are successfully decomposed by using the spectrum centroid. Our excitation-resolving technique is

not only useful for differentiation of ICG states but also used for multiple NIR agent fluorescence images. This technique still poses practical limitations. The imaging speed can be improved by employing high-gain and high-speed CCD cameras, such as intensified CCD and electron-multiplying CCD for the real-time excitation-resolved fluorescence imaging. The excitation leakage of the wavelength-swept laser at longer wavelengths can be reduced by proper design of optical gain medium, lens, and interference filters.

Also, we demonstrate the performance of our HER-NIRF technique as a proof-of-concept to measure the solvatochromic response of ICG in turbid phantoms. The spectroscopic measurement of the local polarity expands the information contents of conventional wide-field fluorescence imaging techniques. Although the sign of the slope is used to identify the presence of DMSO in each pixel qualitatively, our measurements show that quantitative imaging can be possible if one can choose appropriate reference signals to minimize the spectral distortion. As an alternative, if the HER-NIRF imaging is performed before and after the application of DMSO, the reference may not even be required considering the change in the slope of the ratiometric fluorescence. The ability to measure the distribution of DMSO *in vivo* can lead to a better understanding of the pharmacokinetic properties of ICG in tissue. Furthermore, imaging of DMSO by measuring the excitation shift of ICG can be invaluable information for studying the pharmaceutical effect of DMSO on inflammation *in vivo*.

The wavelength-swept laser is the key to our HER-NIRF technique due to its superior performance compared to other available light sources, and it can be a very powerful light source for real-time measurement in various ICG imaging applications. Our HER-NIRF technique provides a much higher image SNR by measuring the whole fluorescence emission spectrum as opposed to conventional systems utilizing band-pass filters at the detection site. By providing additional spectral information, HER-NIRF technique can be applied for measuring the solvatochromic response of other fluorescence dyes and even

be adapted for endoscopic applications due to the efficient light guiding by fiber optics. Our future aim is to apply this HER-NIRF technique for the imaging of ICG to map DMSO distribution *in vivo*.

7.2. Future work

In Part I, the field-of-view of our PEM system will be expanded to cover the whole breast, which simplifies the imaging procedure by removing the PEM detector positioning and the breast MR image analysis before the PEM scan. Our dedicated breast coil will be updated to match the scanning speed of commercial parallel image acquiring breast coils. Ultimately, our system will be updated to operate in a simultaneous data acquisition mode for better temporal resolution, reduced imaging time, and dynamic dual-modality MR/PEM imaging studies.

In Part II, a prototype excitation-resolved NIRF system for intraoperative imaging is developed. However, the current prototype can be further improved by employing an optical amplifier with high gain (20 – 30 dB) at NIR window to increase the fluence rate of our wavelength-swept laser-based excitation-resolved NIRF system. We also plan to develop real-time intraoperative imaging system by employing embedded real-time image processing units. After successful development of the real-time excitation-resolved NIRF system, we plan to validate the system with small animal studies with multiple NIR dyes to solve complex biomedical problems.

References

1. Siegel RL, Miller KD, Jemal A. Cancer statistics, 2016. CA: a cancer journal for clinicians. 2016;66(1):7-30.

2. Society AC. About and key statistics https://www.cancer.org/content/dam/CRC/PDF/Public/8577.00.pdf2017

3. Miller KD, Siegel RL, Lin CC, Mariotto AB, Kramer JL, Rowland JH, et al. Cancer treatment and survivorship statistics, 2016. CA: a cancer journal for clinicians. 2016;66(4):271-89.

4. Siu AL. Screening for breast cancer: US Preventive Services Task Force recommendation statement. Annals of internal medicine. 2016;164(4):279-96.

5. Tabar L, Gad A, Holmberg L, Ljungquist U, Group KCP, Fagerberg C, et al. Reduction in mortality from breast cancer after mass screening with mammography: randomised trial from the Breast Cancer Screening Working Group of the Swedish National Board of Health and Welfare. The Lancet. 1985;325(8433):829-32.

6. Foulkes WD, Smith IE, Reis-Filho JS. Triple-negative breast cancer. New England journal of medicine. 2010;363(20):1938-48.

7. Carney PA, Miglioretti DL, Yankaskas BC, Kerlikowske K, Rosenberg R, Rutter CM, et al. Individual and combined effects of age, breast density, and hormone replacement therapy use on the accuracy of screening mammography. Annals of internal medicine. 2003;138(3):168-75.

8. Bird RE, Wallace TW, Yankaskas BC. Analysis of cancers missed at screening mammography. Radiology. 1992;184(3):613-7.

9. Oude Munnink TH, Nagengast WB, Brouwers AH, Schroder CP, Hospers GA, Lub-de Hooge MN, et al. Molecular imaging of breast cancer. Breast. 2009;18 Suppl 3:S66-73.

10. Rouzier R, Perou CM, Symmans WF, Ibrahim N, Cristofanilli M, Anderson K, et al. Breast cancer molecular subtypes respond differently to preoperative chemotherapy. Clinical Cancer Research. 2005;11(16):5678-85.

11. Gioux S, Choi HS, Frangioni JV. Image-guided surgery using invisible near-infrared light: fundamentals of clinical translation. Molecular imaging. 2010;9(5):237.

12. Weissleder R, Mahmood U. Molecular imaging 1. Radiology. 2001;219(2):316-33.

13. Mankoff DA. A definition of molecular imaging. Journal of Nuclear Medicine. 2007;48(6):18N-21N.

14. Weissleder R. Molecular imaging in cancer. Science. 2006;312(5777):1168-71.

15. Gambhir SS. Molecular imaging of cancer with positron emission tomography. Nature Reviews Cancer. 2002;2(9):683-93.

16. Rosenthal M, Cullom J, Hawkins W, Moore S, Tsui B, Yester M. Quantitative SPECT imaging: a review and recommendations by the Focus Committee of the Society of Nuclear Medicine Computer and Instrumentation Council. Journal of Nuclear Medicine. 1995;36(8):1489-513.

17. Mann RM, Kuhl CK, Kinkel K, Boetes C. Breast MRI: guidelines from the European society of breast imaging. European radiology. 2008;18(7):1307-18.

18. Berg WA, Gutierrez L, NessAiver MS, Carter WB, Bhargavan M, Lewis RS, et al. Diagnostic accuracy of mammography, clinical examination, US, and MR imaging in preoperative assessment of breast cancer 1. Radiology. 2004;233(3):830-49.

19. Bluemke DA, Gatsonis CA, Chen MH, DeAngelis GA, DeBruhl N, Harms S, et al. Magnetic resonance imaging of the breast prior to biopsy. Jama. 2004;292(22):2735-42.

20. Heywang SH, Fenzl G, Hahn D, Krischke I, Edmaier M, Eiermann W, et al. MR imaging of the breast: comparison with mammography and ultrasound. Journal of computer assisted tomography. 1986;10(4):615-20.

21. Sourbron SP, Buckley DL. Classic models for dynamic contrast-enhanced MRI. NMR in biomedicine. 2013;26(8):1004-27.

22. Kelcz F. Quantitative Assessment of T2 Imaging information in differential diagnosis of enhancing breast lesions. Eur radiol. 2006;16(Suppl 5):E51-E3.

23. Kuhl CK, Klaschik S, Mielcarek P, Gieseke J, Wardelmann E, Schild HH. Do T2-weighted pulse sequences help with the differential diagnosis of enhancing lesions in dynamic breast MRI? Journal of Magnetic Resonance Imaging. 1999;9(2):187-96.

24. Dip FD, Ishizawa T, Kokudo N, Rosenthal RJ. Fluorescence Imaging for Surgeons. 2015.

25. De Grand AM, Frangioni JV. An operational near-infrared fluorescence imaging system prototype for large animal surgery. Technol Cancer Res Treat. 2003;2(6):553-62.

26. Mansell J, Monypenny IJ, Skene AI, Abram P, Carpenter R, Gattuso JM, et al. Patterns and predictors of early recurrence in postmenopausal women with estrogen receptor-positive early breast cancer. Breast cancer research and treatment. 2009;117(1):91-8.

27. McCahill LE, Single RM, Bowles EJA, Feigelson HS, James TA, Barney T, et al. Variability in reexcision following breast conservation surgery. Jama. 2012;307(5):467-75.

28. Moran MS, Schnitt SJ, Giuliano AE, Harris JR, Khan SA, Horton J, et al. Society of Surgical Oncology–American Society for Radiation Oncology consensus guideline on margins for breast-conserving surgery with whole-breast irradiation in stages I and II

invasive breast cancer. International Journal of Radiation Oncology* Biology* Physics. 2014;88(3):553-64.

29. Zhang RR, Schroeder AB, Grudzinski JJ, Rosenthal EL, Warram JM, Pinchuk AN, et al. Beyond the margins: real-time detection of cancer using targeted fluorophores. Nature Reviews Clinical Oncology. 2017.

30. Nguyen QT, Tsien RY. Fluorescence-guided surgery with live molecular navigation [mdash] a new cutting edge. Nature reviews cancer. 2013;13(9):653-62.

31. Harlaar NJ, van Dam GM, Ntziachristos V. Intraoperative Optical Imaging. Intraoperative Imaging and Image-Guided Therapy: Springer; 2014. p. 233-45.

32. Hong G, Antaris AL, Dai H. Near-infrared fluorophores for biomedical imaging. Nature Biomedical Engineering. 2017;1:0010.

33. Alander JT, Kaartinen I, Laakso A, Pätilä T, Spillmann T, Tuchin VV, et al. A review of indocyanine green fluorescent imaging in surgery. Journal of Biomedical Imaging. 2012;2012:7.

34. Vahrmeijer AL, Hutteman M, van der Vorst JR, van de Velde CJH, Frangioni JV. Image-guided cancer surgery using near-infrared fluorescence. Nat Rev Clin Oncol. 2013;10(9):507-18.

35. Landsman M, Kwant G, Mook G, Zijlstra W. Light-absorbing properties, stability, and spectral stabilization of indocyanine green. Journal of applied physiology. 1976;40(4):575-83.

36. Rodriguez VB, Henry SM, Hoffman AS, Stayton PS, Li X, Pun SH. Encapsulation and stabilization of indocyanine green within poly(styrene-alt-maleic anhydride) block-poly(styrene) micelles for near-infrared imaging. J Biomed Opt. 2008;13(1):014025.

37. Cherrick GR, Stein SW, Leevy CM, Davidson CS. Indocyanine green: observations on its physical properties, plasma decay, and hepatic extraction. Journal of Clinical Investigation. 1960;39(4):592.

38. Vinegoni C, Botnaru I, Aikawa E, Calfon MA, Iwamoto Y, Folco EJ, et al. Indocyanine green enables near-infrared fluorescence imaging of lipid-rich, inflamed atherosclerotic plaques. Science translational medicine. 2011;3(84):84ra45-84ra45.

39. Heath CH, Deep NL, Sweeny L, Zinn KR, Rosenthal EL. Use of panitumumab-IRDye800 to image microscopic head and neck cancer in an orthotopic surgical model. Annals of surgical oncology. 2012;19(12):3879-87.

40. Rosenthal EL, Warram JM, de Boer E, Chung TK, Korb ML, Brandwein-Gensler M, et al. Safety and tumor specificity of cetuximab-IRDye800 for surgical navigation in head and neck cancer. Clinical Cancer Research. 2015;21(16):3658-66.

41. Choi HS, Gibbs SL, Lee JH, Kim SH, Ashitate Y, Liu F, et al. Targeted zwitterionic near-infrared fluorophores for improved optical imaging. Nature biotechnology. 2013;31(2):148-53.

42. Tanaka E, Chen FY, Flaumenhaft R, Graham GJ, Laurence RG, Frangioni JV. Real-time assessment of cardiac perfusion, coronary angiography, and acute intravascular thrombi using dual-channel near-infrared fluorescence imaging. The Journal of thoracic and cardiovascular surgery. 2009;138(1):133-40.

43. Taggart DP, Choudhary B, Anastasiadis K, Abu-Omar Y, Balacumaraswami L, Pigott DW. Preliminary experience with a novel intraoperative fluorescence imaging technique to evaluate the patency of bypass grafts in total arterial revascularization. The Annals of thoracic surgery. 2003;75(3):870-3.

44. Yamamoto M, Sasaguri S, Sato T. Assessing intraoperative blood flow in cardiovascular surgery. Surgery today. 2011;41(11):1467-74.

45. Verbeek FP, Schaafsma BE, Tummers QR, van der Vorst JR, van der Made WJ, Baeten CI, et al. Optimization of near-infrared fluorescence cholangiography for open and laparoscopic surgery. Surgical endoscopy. 2014;28(4):1076-82.

46. Schols RM, Bouvy ND, Masclee AA, van Dam RM, Dejong CH, Stassen LP. Fluorescence cholangiography during laparoscopic cholecystectomy: a feasibility study on early biliary tract delineation. Surgical endoscopy. 2013;27(5):1530-6.

47. Zarrinpar A, Dutson EP, Mobley C, Busuttil RW, Lewis CE, Tillou A, et al. Intraoperative Laparoscopic Near-Infrared Fluorescence Cholangiography to Facilitate Anatomical Identification: When to Give Indocyanine Green and How Much. Surgical innovation. 2016;23(4):360-5.

48. van der Vorst JR, Schaafsma BE, Hutteman M, Verbeek FP, Liefers GJ, Hartgrink HH, et al. Near-infrared fluorescence-guided resection of colorectal liver metastases. Cancer. 2013;119(18):3411-8.

49. Ishizawa T, Fukushima N, Shibahara J, Masuda K, Tamura S, Aoki T, et al. Real-time identification of liver cancers by using indocyanine green fluorescent imaging. Cancer. 2009;115(11):2491-504.

50. Ferroli P, Acerbi F, Albanese E, Tringali G, Broggi M, Franzini A, et al. Application of intraoperative indocyanine green angiography for CNS tumors: results on the first 100 cases. Intraoperative Imaging: Springer; 2011. p. 251-7.

51. Perry D, Bharara M, Armstrong DG, Mills J. Intraoperative fluorescence vascular angiography: during tibial bypass. Journal of diabetes science and technology. 2012;6(1):204-8.

52. Forsythe RO, Hinchliffe RJ. Assessment of foot perfusion in patients with a diabetic foot ulcer. Diabetes/metabolism research and reviews. 2016;32(S1):232-8.

53. Troyan SL, Kianzad V, Gibbs-Strauss SL, Gioux S, Matsui A, Oketokoun R, et al. The FLARE intraoperative near-infrared fluorescence imaging system: a first-in-human clinical trial in breast cancer sentinel lymph node mapping. Ann Surg Oncol. 2009;16(10):2943-52.

54. Tagaya N, Yamazaki R, Nakagawa A, Abe A, Hamada K, Kubota K, et al. Intraoperative identification of sentinel lymph nodes by near-infrared fluorescence imaging in patients with breast cancer. The American Journal of Surgery. 2008;195(6):850-3.

55. Parungo CP, Ohnishi S, Kim S-W, Kim S, Laurence RG, Soltesz EG, et al. Intraoperative identification of esophageal sentinel lymph nodes with near-infrared fluorescence imaging. The Journal of thoracic and cardiovascular surgery. 2005;129(4):844-50.

56. van Driel P, van de Giessen M, Boonstra M, Snoeks T, Keereweer S, Oliveira S, et al. Characterization and evaluation of the artemis camera for fluorescence-guided cancer surgery. Molecular Imaging and Biology. 2015;17(3):413-23.

57. Spinoglio G, Priora F, Bianchi PP, Lucido FS, Licciardello A, Maglione V, et al. Real-time near-infrared (NIR) fluorescent cholangiography in single-site robotic cholecystectomy (SSRC): a single-institutional prospective study. Surgical endoscopy. 2013;27(6):2156-62.

58. Tobis S, Knopf J, Silvers C, Yao J, Rashid H, Wu G, et al. Near infrared fluorescence imaging with robotic assisted laparoscopic partial nephrectomy: initial clinical experience for renal cortical tumors. The Journal of urology. 2011;186(1):47-52.

59. Zhu B, Sevick-Muraca E. A review of performance of near-infrared fluorescence imaging devices used in clinical studies. The British journal of radiology. 2014;88(1045):20140547.

60. Sevick-Muraca EM, Sharma R, Rasmussen JC, Marshall MV, Wendt JA, Pham HQ, et al. Imaging of lymph flow in breast cancer patients after microdose administration of a near-infrared fluorophore: feasibility study. Radiology. 2008;246(3):734-41.

61. Stoffels I, Dissemond J, Pöppel T, Schadendorf D, Klode J. Intraoperative fluorescence imaging for sentinel lymph node detection: prospective clinical trial to compare the usefulness of indocyanine green vs technetium Tc 99m for identification of sentinel lymph nodes. JAMA surgery. 2015;150(7):617-23.

62. DSouza AV, Lin H, Henderson ER, Samkoe KS, Pogue BW. Review of fluorescence guided surgery systems: identification of key performance capabilities beyond indocyanine green imaging. Journal of Biomedical Optics. 2016;21(8):080901-.

63. Hoffmann C, Compton F, Schäfer J, Steiner U, Fuller T, Schostak M, et al., editors. Intraoperative assessment of kidney allograft perfusion by laser-assisted indocyanine green fluorescence videography. Transplantation Proceedings; 2010: Elsevier.

64. Barkhoudarian G, Romero ADCB, Laws ER. Evaluation of the 3-dimensional endoscope in transsphenoidal surgery. Operative Neurosurgery. 2013;73:ons74-ons9.

65. Jones GE, Garcia CA, Murray J, Elwood ET, Whitty LA. Fluorescent intraoperative tissue angiography for the evaluation of the viability of pedicled TRAM flaps. Plastic and Reconstructive Surgery. 2009;124(4S):53.

66. Takahashi M, Ishikawa T, Higashidani K, Katoh H. SPY™: an innovative intra-operative imaging system to evaluate graft patency during off-pump coronary artery bypass grafting. Interactive cardiovascular and thoracic surgery. 2004;3(3):479-83.

67. Fengler J. Near-infrared fluorescence laparoscopy-technical description of PINPOINT® a novel and commercially available system. Colorectal Disease. 2015;17(S3):3-6.

68. Van Dam GM, Themelis G, Crane LM, Harlaar NJ, Pleijhuis RG, Kelder W, et al. Intraoperative tumor-specific fluorescence imaging in ovarian cancer by folate receptor-[alpha] targeting: first in-human results. Nature medicine. 2011;17(10):1315-9.

69. Troyan SL, Kianzad V, Gibbs-Strauss SL, Gioux S, Matsui A, Oketokoun R, et al. The FLARE™ intraoperative near-infrared fluorescence imaging system: a first-in-human clinical trial in breast cancer sentinel lymph node mapping. Annals of surgical oncology. 2009;16(10):2943-52.

70. Mieog JSD, Troyan SL, Hutteman M, Donohoe KJ, van der Vorst JR, Stockdale A, et al. Toward optimization of imaging system and lymphatic tracer for near-infrared fluorescent sentinel lymph node mapping in breast cancer. Annals of surgical oncology. 2011;18(9):2483-91.

71. Liu Y, Bauer AQ, Akers WJ, Sudlow G, Liang K, Shen D, et al. Hands-free, wireless goggles for near-infrared fluorescence and real-time image-guided surgery. Surgery. 2011;149(5):689-98.

72. Gotoh K, Yamada T, Ishikawa O, Takahashi H, Eguchi H, Yano M, et al. A novel image-guided surgery of hepatocellular carcinoma by indocyanine green fluorescence imaging navigation. Journal of surgical oncology. 2009;100(1):75-9.

73. Tajima Y, Murakami M, Yamazaki K, Masuda Y, Kato M, Sato A, et al. Sentinel node mapping guided by indocyanine green fluorescence imaging during laparoscopic surgery in gastric cancer. Annals of surgical oncology. 2010;17(7):1787-93.

74. Handa T, Katare RG, Nishimori H, Wariishi S, Fukutomi T, Yamamoto M, et al. New device for intraoperative graft assessment: HyperEye charge-coupled device camera system. General thoracic and cardiovascular surgery. 2010;58(2):68-77.

75. Koch M, Glatz J, Ermolayev V, de Vries EG, van Dam GM, Englmeier K-H, et al. Video-rate optical flow corrected intraoperative functional fluorescence imaging. Journal of biomedical optics. 2014;19(4):046012-.

76. Tichauer KM, Samkoe KS, Gunn JR, Kanick SC, Hoopes PJ, Barth RJ, et al. Microscopic lymph node tumor burden quantified by macroscopic dual-tracer molecular imaging. Nature medicine. 2014;20(11):1348-53.

77. Elliott JT, Marra K, Evans LT, Davis SC, Samkoe KS, Feldwisch J, et al. Simultaneous in vivo fluorescent markers for perfusion, protoporphyrin metabolism and EGFR expression for optically guided identification of orthotopic glioma. Clinical Cancer Research. 2016:clincanres. 1400.2016.

78. Valdés PA, Leblond F, Jacobs VL, Wilson BC, Paulsen KD, Roberts DW. Quantitative, spectrally-resolved intraoperative fluorescence imaging. Scientific reports. 2012;2.

79. Ashitate Y, Vooght CS, Hutteman M, Oketokoun R, Choi HS, Frangioni JV. Simultaneous assessment of luminal integrity and vascular perfusion of the gastrointestinal tract using dual-channel near-infrared fluorescence. Molecular imaging. 2012;11(4):7290.2011. 00048.

80. Hyun H, Henary M, Gao T, Narayana L, Owens EA, Lee JH, et al. 700-nm zwitterionic near-infrared fluorophores for dual-channel image-guided surgery. Molecular Imaging and Biology. 2016;18(1):52-61.

81. Yun SH, Bouma BE. Wavelength swept lasers. Optical coherence tomography: technology and applications. 2015:619-37.

82. Rapidly wavelength-swept laser at 780 nm. IEEE Photon Technol Lett. 2011;23:197.

83. External line-cavity wavelength-swept source at 850 nm for optical coherence tomography. IEEE Photon Technol Lett. 2007;19:176.

84. Optical frequency domain imaging with a rapidly swept laser in the 815–870 nm range. Opt Express. 2006;14:5937.

85. Cho J, Gulsen G, Kim C-S. 800-nm-centered swept laser for spectroscopic optical coherence tomography. Laser Physics. 2014;24(4):045605.

86. Fourier domain optical coherence tomography for retinal imaging with 800-nm swept source: Real-time resampling in k-domain. J Opt Soc. 2011;15:293.

87. Evans R. The Atomic Nucleus. Malabar, Fla. Robert E. Krieger; 1955.

88. Humm JL, Rosenfeld A, Del Guerra A. From PET detectors to PET scanners. European journal of nuclear medicine and molecular imaging. 2003;30(11):1574-97.

89. Cho Z, Chan J, Ericksson L, Singh M, Graham S, MacDonald N, et al. Positron ranges obtained from biomedically important positron-emitting radionuclides. J Nucl Med. 1975;16(12):1174-6.

90. Eisberg R, Resnick R, Brown J. Quantum physics of atoms, molecules, solids, nuclei, and particles. Physics Today. 1986;39:110.

91. Hoffman EJ, Huang S-C, Phelps ME. Quantitation in positron emission computed tomography: 1. Effect of object size. Journal of computer assisted tomography. 1979;3(3):299-308.

92. Kessler RM, Ellis Jr JR, Eden M. Analysis of emission tomographic scan data: limitations imposed by resolution and background. LWW; 1984.

93. Meltzer CC, Leal JP, Mayberg HS, Wagner Jr HN, Frost JJ. Correction of PET data for partial volume effects in human cerebral cortex by MR imaging. Journal of computer assisted tomography. 1990;14(4):561-70.

94. Müller-Gärtner HW, Links JM, Prince JL, Bryan RN, McVeigh E, Leal JP, et al. Measurement of radiotracer concentration in brain gray matter using positron emission tomography: MRI-based correction for partial volume effects. Journal of Cerebral Blood Flow & Metabolism. 1992;12(4):571-83.

95. Rousset OG, Ma Y, Evans AC. Correction for partial volume effects in PET: principle and validation. The journal of nuclear medicine. 1998;39(5):904.

96. Meltzer CC, Kinahan PE, Greer PJ, Nichols TE. Comparative evaluation of MR-based partial-volume correction schemes for PET. The Journal of Nuclear Medicine. 1999;40(12):2053.

97. O'Sullivan TD, Cerussi AE, Cuccia DJ, Tromberg BJ. Diffuse optical imaging using spatially and temporally modulated light. Journal of biomedical optics. 2012;17(7):0713111-07131114.

98. Guilbault GG. Practical fluorescence: CRC Press; 1990.

99. Olopade OI, Grushko TA, Nanda R, Huo D. Advances in breast cancer: pathways to personalized medicine. Clinical Cancer Research. 2008;14(24):7988-99.

100. Liedtke C, Mazouni C, Hess KR, André F, Tordai A, Mejia JA, et al. Response to neoadjuvant therapy and long-term survival in patients with triple-negative breast cancer. Journal of clinical oncology. 2008;26(8):1275-81.

101. Lund MJ, Butler EN, Hair BY, Ward KC, Andrews JH, Oprea-Ilies G, et al. Age/race differences in HER2 testing and in incidence rates for breast cancer triple subtypes. Cancer. 2010;116(11):2549-59.

102. Kohler BA, Sherman RL, Howlader N, Jemal A, Ryerson AB, Henry KA, et al. Annual report to the nation on the status of cancer, 1975-2011, featuring incidence of breast cancer subtypes by race/ethnicity, poverty, and state. Journal of the National Cancer Institute. 2015;107(6):djv048.

103. Sineshaw HM, Gaudet M, Ward EM, Flanders WD, Desantis C, Lin CC, et al. Association of race/ethnicity, socioeconomic status, and breast cancer subtypes in the National Cancer Data Base (2010–2011). Breast cancer research and treatment. 2014;145(3):753-63.

104. Yankeelov TE, Lepage M, Chakravarthy A, Broome EE, Niermann KJ, Kelley MC, et al. Integration of quantitative DCE-MRI and ADC mapping to monitor treatment response in human breast cancer: initial results. Magnetic resonance imaging. 2007;25(1):1-13.

105. Martincich L, Montemurro F, De Rosa G, Marra V, Ponzone R, Cirillo S, et al. Monitoring response to primary chemotherapy in breast cancer using dynamic contrast-enhanced magnetic resonance imaging. Breast cancer research and treatment. 2004;83(1):67-76.

106. Li X, Arlinghaus LR, Ayers GD, Chakravarthy AB, Abramson RG, Abramson VG, et al. DCE-MRI analysis methods for predicting the response of breast cancer to neoadjuvant chemotherapy: Pilot study findings. Magnetic resonance in medicine. 2014;71(4):1592-602.

107. Hrung JM, Sonnad SS, Schwartz JS, Langlotz CP. Accuracy of MR imaging in the work-up of suspicious breast lesions: a diagnostic meta-analysis. Academic radiology. 1999;6(7):387-97.

108. Judenhofer MS, Wehrl HF, Newport DF, Catana C, Siegel SB, Becker M, et al. Simultaneous PET-MRI: a new approach for functional and morphological imaging. Nat Med. 2008;14(4):459-65.

109. Pichler BJ, Kolb A, Nägele T, Schlemmer H-P. PET/MRI: paving the way for the next generation of clinical multimodality imaging applications. Journal of Nuclear Medicine. 2010;51(3):333-6.

110. Romeo V, D'Aiuto M, Frasci G, Imbriaco M, Nicolai E. Simultaneous PET/MRI assessment of response to cytotoxic and hormone neo-adjuvant chemotherapy in breast cancer: a preliminary report. Medical Oncology. 2017;34(2):18.

111. Henry T, Chungani H, Abou-Khalil W, Theodore W, Swartz B. Positron emission tomography. Medical Imaging: Principles and Practices. 2012.

112. Wahl RL, Zasadny K, Helvie M, Hutchins GD, Weber B, Cody R. Metabolic monitoring of breast cancer chemohormonotherapy using positron emission tomography: initial evaluation. Journal of Clinical Oncology. 1993;11(11):2101-11.

113. Muehllehner G, Karp JS. Positron emission tomography. Physics in medicine and biology. 2006;51(13):R117.

114. Levin CS, Hoffman EJ. Calculation of positron range and its effect on the fundamental limit of positron emission tomography system spatial resolution. Physics in medicine and biology. 1999;44(3):781.

115. Thompson C, Murthy K, Weinberg I, Mako F. Feasibility study for positron emission mammography. Medical physics. 1994;21(4):529-38.

116. Thompson C, Murthy K, Picard Y, Weinberg I, Mako R. Positron emission mammography (PEM): a promising technique for detecting breast cancer. IEEE transactions on nuclear science. 1995;42(4):1012-7.

117. Tafra L. Positron emission tomography (PET) and mammography (PEM) for breast cancer: importance to surgeons. Annals of surgical oncology. 2007;14(1):3-13.

118. Kelly L, Khatiwada S, Moorby E, Noble R, Purches J, Tong J, et al. Positron Emission Mammography (pem) For The Diagnosis Of Breast Cancer In Young Women: A Literature Review. Internal Medicine Journal. 2014;44:26-7.

119. Berg WA, Weinberg IN, Narayanan D, Lobrano ME, Ross E, Amodei L, et al. High-Resolution Fluorodeoxyglucose Positron Emission Tomography with Compression ("Positron Emission Mammography") is Highly Accurate in Depicting Primary Breast Cancer. The breast journal. 2006;12(4):309-23.

120. Muehllehner G. Effect of resolution improvement on required count density in ECT imaging: a computer simulation. Physics in medicine and biology. 1985;30(2):163.

121. Ha S, Hamamura MJ, Roeck WW, Hugg J, Wagenaar DJ, Meier D, et al. Feasibility study of a unilateral RF array coil for MR-scintimammography. Physics in medicine and biology. 2011;56(21):6809.

122. Ha S, Hamamura MJ, Nalcioglu O, Muftuler LT. A PIN diode controlled dual-tuned MRI RF coil and phased array for multi nuclear imaging. Physics in medicine and biology. 2010;55(9):2589.

123. Barnes G. Mammography equipment: compression, scatter control, and automatic exposure control. Syllabus: a categorical course in physics. 1993:73-82.

124. Mani V. Survey of medical image registration. Journal of Biomedical Engineering and Technology. 2013;1(2):8-25.

125. Dmitriev I, Loo C, Vogel W, Pengel K, Gilhuijs K. Fully automated deformable registration of breast DCE-MRI and PET/CT. Physics in medicine and biology. 2013;58(4):1221.

126. Leibfarth S, Mönnich D, Welz S, Siegel C, Schwenzer N, Schmidt H, et al. A strategy for multimodal deformable image registration to integrate PET/MR into radiotherapy treatment planning. Acta oncologica. 2013;52(7):1353-9.

127. MacDonald L, Edwards J, Lewellen T, Haseley D, Rogers J, Kinahan P. Clinical imaging characteristics of the positron emission mammography camera: PEM Flex Solo II. Journal of Nuclear Medicine. 2009;50(10):1666-75.

128. Rakow-Penner R, Daniel B, Yu H, Sawyer-Glover A, Glover GH. Relaxation times of breast tissue at 1.5 T and 3T measured using IDEAL. Journal of Magnetic Resonance Imaging. 2006;23(1):87-91.

129. Farrer AI, Odéen H, de Bever J, Coats B, Parker DL, Payne A, et al. Characterization and evaluation of tissue-mimicking gelatin phantoms for use with MRgFUS. Journal of therapeutic ultrasound. 2015;3(1):1.

130. Rao P, Gregg E. Attenuation of monoenergetic gamma rays in tissues. American Journal of Roentgenology. 1975;123(3):631-7.

131. Schneider CA, Rasband WS, Eliceiri KW. NIH Image to ImageJ: 25 years of image analysis. Nature methods. 2012;9(7):671.

132. Wieczorek H. The image quality of FBP and MLEM reconstruction. Physics in medicine and biology. 2010;55(11):3161.

133. Smith MF, Majewski S, Weisenberger AG, Kieper DA, Raylman RR, Turkington TG. Analysis of factors affecting positron emission mammography (PEM) image formation. IEEE Transactions on Nuclear Science. 2003;50(1):53-9.

134. Karp JS, Surti S, Daube-Witherspoon ME, Muehllehner G. Benefit of time-of-flight in PET: experimental and clinical results. Journal of Nuclear Medicine. 2008;49(3):462-70.

135. Schug D, Lerche C, Weissler B, Gebhardt P, Goldschmidt B, Wehner J, et al. Initial PET performance evaluation of a preclinical insert for PET/MRI with digital SiPM technology. Physics in medicine and biology. 2016;61(7):2851.

136. Schug D, Wehner J, Dueppenbecker PM, Weissler B, Gebhardt P, Goldschmidt B, et al. PET performance and MRI compatibility evaluation of a digital, ToF-capable PET/MRI insert equipped with clinical scintillators. Physics in medicine and biology. 2015;60(18):7045.

137. Kim CL, Wang G-C, Dolinsky S. Multi-pixel photon counters for TOF PET detector and its challenges. IEEE Transactions on Nuclear Science. 2009;56(5):2580-5.

138. Schug D, Weissler B, Gebhardt P, Schulz V. Crystal Delay and Time Walk Correction Methods for Coincidence Resolving Time Improvements of a Digital-Silicon-Photomultiplier-based PET/MRI Insert. IEEE Transactions on Nuclear Science. 2017.

139. Vandenberghe S, Marsden PK. PET-MRI: a review of challenges and solutions in the development of integrated multimodality imaging. Physics in medicine and biology. 2015;60(4):R115.

140. Birdwell RL, Mountford CE, Iglehart JD. Molecular imaging of the breast. American Journal of Roentgenology. 2009;193(2):367-76.

141. Roemer PB, Edelstein WA, Hayes CE, Souza SP, Mueller O. The NMR phased array. Magnetic resonance in medicine. 1990;16(2):192-225.

142. Deshmane A, Gulani V, Griswold MA, Seiberlich N. Parallel MR imaging. Journal of Magnetic Resonance Imaging. 2012;36(1):55-72.

143. Pruessmann KP, Weiger M, Scheidegger MB, Boesiger P. SENSE: sensitivity encoding for fast MRI. Magnetic resonance in medicine. 1999;42(5):952-62.

144. Griswold MA, Jakob PM, Heidemann RM, Nittka M, Jellus V, Wang J, et al. Generalized autocalibrating partially parallel acquisitions (GRAPPA). Magnetic resonance in medicine. 2002;47(6):1202-10.

145. Darne C, Lu Y, Sevick-Muraca EM. Small animal fluorescence and bioluminescence tomography: a review of approaches, algorithms and technology update. Physics in medicine and biology. 2014;59(1):R1.

146. Yang B, Tunnell JW. Real-time absorption reduced surface fluorescence imaging. Journal of biomedical optics. 2014;19(9):090505-.

147. Kitai T, Inomoto T, Miwa M, Shikayama T. Fluorescence navigation with indocyanine green for detecting sentinel lymph nodes in breast cancer. Breast cancer. 2005;12(3):211-5.

148. Zhao W, Carreira EM. Conformationally Restricted Aza-Bodipy: A Highly Fluorescent, Stable, Near-Infrared-Absorbing Dye. Angewandte Chemie International Edition. 2005;44(11):1677-9.

149. Reichardt C. Solvatochromic dyes as solvent polarity indicators. Chemical Reviews. 1994;94(8):2319-58.

150. Pera V, Brooks DH, Niedre M. Multiplexed fluorescence tomography with spectral and temporal data: demixing with intrinsic regularization. Biomedical Optics Express. 2016;7(1):111-31.

151. Würth C, Grabolle M, Pauli J, Spieles M, Resch-Genger U. Relative and absolute determination of fluorescence quantum yields of transparent samples. Nature protocols. 2013;8(8):1535-50.

152. Shafirstein G, Moreno M, Klein A, Siegel E, Babilas P, Landthaler M, et al. Treatment of leg veins with indocyanine green and lasers investigated with mathematical modelling. International Journal of Hyperthermia. 2011;27(8):771-81.

153. Adams KE, Ke S, Hirschi K, Mawad ME, Barry MA, Sevick-Muraca EM, et al. Comparison of visible and near-infrared wavelength-excitable fluorescent dyes for molecular imaging of cancer. Journal of biomedical optics. 2007;12(2):024017--9.

154. Desmettre T, Devoisselle J, Mordon S. Fluorescence properties and metabolic features of indocyanine green (ICG) as related to angiography. Survey of ophthalmology. 2000;45(1):15-27.

155. Mordon S, Devoisselle JM, Soulie-Begu S, Desmettre T. Indocyanine Green: Physicochemical Factors Affecting Its Fluorescence< i> in Vivo</i>. Microvascular research. 1998;55(2):146-52.

156. Kim T, Chen Y, Mount C, Gombotz W, Li X, Pun S. Evaluation of Temperature-Sensitive, Indocyanine Green-Encapsulating Micelles for Noninvasive Near-Infrared Tumor Imaging. Pharmaceutical Research. 2010;27(9):1900-13.

157. Kim M, Chen Y, Mehl P. Hyperspectral reflectance and fluorescence imaging system for food quality and safety. TRANSACTIONS-AMERICAN SOCIETY OF AGRICULTURAL ENGINEERS. 2001;44(3):721-30.

158. Rapid wavelength-swept spectrally encoded confocal microscopy. Opt Express. 2005;13:8214.

159. Cho J, Jeon SW, Zheng J, Kim C-S, Nalcioglu O, Gulsen G, editors. Development of a spectrally-resolved fluorescence tomography system using a NIR swept laser and a digital micromirror array based detection system. SPIE BiOS; 2014: International Society for Optics and Photonics.

160. Cho J, Lim G, Jeong MY, Nalcioglu O, Kim C-S, Gulsen G, editors. Diffuse optical tomography using wavelength-swept laser. SPIE BiOS; 2013: International Society for Optics and Photonics.

161. Kim HJ, Cho J, Noh Y-O, Oh M-C, Chen Z, Kim C-S. Three-dimensional surface phase imaging based on integrated thermo-optic swept laser. Measurement Science and Technology. 2014;25(3):035201.

162. Lim H, De Boer J, Park B, Lee E, Yelin R, Yun S. Optical frequency domain imaging with a rapidly swept laser in the 815-870 nm range. Optics express. 2006;14(13):5937-44.

163. Weber G, Teale F. Fluorescence excitation spectrum of organic compounds in solution. Part 1.—Systems with quantum yield independent of the exciting wavelength. Transactions of the Faraday Society. 1958;54:640-8.

164. Fourier domain mode locking (FDML): a new laser operating regime and applications for optical coherence tomography. Opt Express. 2006;14:3225.

165. Zhu B, Rasmussen JC, Lu Y, Sevick-Muraca EM. Reduction of excitation light leakage to improve near-infrared fluorescence imaging for tissue surface and deep tissue imaging. Med Phys. 2010;37(11):5961-70.

166. Ahn H, Kim J, Jeung E-B, Lee G-S. Dimethyl sulfoxide inhibits NLRP3 inflammasome activation. Immunobiology. 2014;219(4):315-22.

167. Pal R, Mamidi MK, Das AK, Bhonde R. Diverse effects of dimethyl sulfoxide (DMSO) on the differentiation potential of human embryonic stem cells. Archives of toxicology. 2012;86(4):651-61.

168. Santos NC, Figueira-Coelho J, Martins-Silva J, Saldanha C. Multidisciplinary utilization of dimethyl sulfoxide: pharmacological, cellular, and molecular aspects. Biochemical pharmacology. 2003;65(7):1035-41.

169. Swartling J SJBDTK, Andersson-Engels S. Fluorescence spectra provide information on the depth of fluorescent lesions in tissue. Appl Opt. 2005;44(10):1934.

170. Kolste KK, Kanick SC, Valdés PA, Jermyn M, Wilson BC, Roberts DW, et al. Macroscopic optical imaging technique for wide-field estimation of fluorescence depth in optically turbid media for application in brain tumor surgical guidance. Journal of biomedical optics. 2015;20(2):026002-.

171. Lipinski CA. Drug-like properties and the causes of poor solubility and poor permeability. Journal of pharmacological and toxicological methods. 2000;44(1):235-49.

172. Lipinski CA, Lombardo F, Dominy BW, Feeney PJ. Experimental and computational approaches to estimate solubility and permeability in drug discovery and development settings. Advanced drug delivery reviews. 1997;23(1-3):3-25.

173. Avdeef A. Absorption and drug development: solubility, permeability, and charge state: John Wiley & Sons; 2012.

174. Saar BG, Freudiger CW, Reichman J, Stanley CM, Holtom GR, Xie XS. Video-rate molecular imaging in vivo with stimulated Raman scattering. Science. 2010;330(6009):1368-70.

175. Berezin MY, Lee H, Akers W, Achilefu S. Near Infrared Dyes as Lifetime Solvatochromic Probes for Micropolarity Measurements of Biological Systems. Biophysical Journal. 2007;93(8):2892-9.

176. Jung B, Vullev VI, Anvari B. Revisiting indocyanine green: Effects of serum and physiological temperature on absorption and fluorescence characteristics. Selected Topics in Quantum Electronics, IEEE Journal of. 2014;20(2):149-57.

177. Nairat M, Konar A, Kaniecki M, Lozovoy VV, Dantus M. Investigating the role of human serum albumin protein pocket on the excited state dynamics of indocyanine green using shaped femtosecond laser pulses. Physical Chemistry Chemical Physics. 2015;17(8):5872-7.

178. Akers WJ, Berezin MY, Lee H, Achilefu S. Predicting in vivo fluorescence lifetime behavior of near-infrared fluorescent contrast agents using in vitro measurements. Journal of biomedical optics. 2008;13(5):054042--9.